

**Dipl.-Ing. Martin Luckabauer**

# **Extension of the temperature range in kinetics studies on metallic glasses by novel dilatometric techniques**

## **DOCTORAL THESIS**

For obtaining the academic degree of  
Doktor der technischen Wissenschaften

Doctoral Programme of Technical Sciences  
Technical Physics



Graz University of Technology

Supervisor:  
Assoc.Prof. Dr. Wolfgang Sprengel  
Institute of Materials Physics

Graz, May 2014



**EIDESSTATTLICHE ERKLÄRUNG**  
**AFFIDAVIT**

Ich erkläre an Eides statt, dass ich die vorliegende Arbeit selbstständig verfasst, andere als die angegebenen Quellen/Hilfsmittel nicht benutzt, und die den benutzten Quellen wörtlich und inhaltlich entnommenen Stellen als solche kenntlich gemacht habe. Das in TUGRAZonline hochgeladene Textdokument ist mit der vorliegenden Dissertation identisch.

*I declare that I have authored this thesis independently, that I have not used other than the declared sources/resources, and that I have explicitly indicated all material which has been quoted either literally or by content from the sources used. The text document uploaded to TUGRAZonline is identical to the present doctoral dissertation.*

---

Datum / Date

---

Unterschrift / Signature



# Abstract

The study of volume kinetics in metallic glasses is one fundamental aspect on the way to a comprehensive understanding of this class of materials. The characterizing phenomenon of all glasses, the glass transition is inherently linked to the amount of atomic free volume available for atomic or molecular motion in the material. However, with the established measurement techniques it is only possible to investigate specific volume changes on relatively short time-scales and at temperatures near the calorimetric glass transition. In this work a dilatometric measurement device based on laser-interferometry for contactless length measurements in the nm range was adapted and further developed to assess the specific volume kinetics in metallic glasses on time-scales of up to  $10^6$  s with a measurement resolution of 10 nm. For this purpose an entirely new specimen support and heating system was implemented into the dilatometer and the control hardware and software was redesigned. The reversible equilibrium volume formation was studied in two different bulk glassy alloys using the new measurement setup. The results were analysed in terms of their underlying atomic processes. Effective activation energies could be derived and were compared with results from other measurement techniques especially to values obtained from tracer diffusion experiments. As a complementing measurement technique dynamic mechanical analysis (DMA) was performed and differences to the dilatometric studies were emphasized. To directly probe the glass transition with the new measurement capabilities a method for the realization of effective heating rates in the order of  $10^{-2}$  K/min was developed and applied to the low-temperature specific volume evolution of an equilibrated bulk metallic glass. Positron annihilation experiments using a high-intensity positron beam were conducted to get deeper insights into the free volume on an atomistic scale. Additionally, possible changes in the chemical environment of the positron annihilation site during thermal treatments below the glass transition temperature were addressed by coincident Doppler broadening experiments. As an extension to the measurement capabilities of the laser-dilatometer a new measurement technique based on temperature modulation was developed. This method allows for the simultaneous measurement of isothermal volume equilibration and phase transformations. As a first measurement the low-temperature crystallization kinetics of a Zr-based glassy alloy was studied. The results were analysed in the framework of established models for describing crystallization kinetics.



---

# Contents

---

<b>Abstract</b>	i
<b>1 Introduction</b>	1
<b>2 Terminology and Applied Models</b>	5
2.1 The glass transition . . . . .	5
2.2 Relaxation in glasses . . . . .	6
2.3 Models for the sub- $T_g$ volume-equilibration in bulk metallic glasses . . . . .	8
<b>3 Materials and Methods</b>	15
3.1 Materials and sample preparation . . . . .	15
3.2 Characterization methods . . . . .	17
3.3 Experimental methods . . . . .	18
<b>4 The Laser-Dilatometer</b>	23
4.1 General idea and basic principle of operation . . . . .	24
4.2 Developments and functional details . . . . .	27
4.3 Dilatometric measurement techniques . . . . .	40
4.4 Measurements on B2-Fe <sub>61</sub> Al <sub>39</sub> . . . . .	43
<b>5 Results and Discussion</b>	57
5.1 Kinetics in the glassy state . . . . .	57
5.1.1 Zr <sub>56</sub> Al <sub>7</sub> Cu <sub>24</sub> Ni <sub>10</sub> Co <sub>3</sub> : Volume equilibration . . . . .	57
5.1.2 Zr <sub>56</sub> Al <sub>7</sub> Cu <sub>24</sub> Ni <sub>10</sub> Co <sub>3</sub> : Dynamic mechanical analysis . . . . .	71
5.1.3 Zr <sub>52.5</sub> Ti <sub>5</sub> Cu <sub>17.9</sub> Ni <sub>14.6</sub> Al <sub>10</sub> : Volume equilibration . . . . .	80

5.1.4	Discussion . . . . .	87
5.2	The glass transition . . . . .	93
5.3	The specific volume on a local atomic scale . . . . .	102
5.4	Low-temperature crystallization kinetics . . . . .	110
<b>6</b>	<b>Summary and Conclusion</b>	<b>123</b>
<b>Bibliography</b>		<b>127</b>
<b>A</b>	<b>Dilatometer control software</b>	<b>135</b>
<b>Acknowledgement / Danksagung</b>		<b>143</b>

---

# 1 Introduction

---

Since the discovery of bulk metallic glasses in the early nineteen-nineties [1, 2] a lot of effort was devoted to the development of advanced alloy systems with high glass forming ability and favourable mechanical properties. The combination of unique processing possibilities and outstanding material properties makes bulk metallic glasses to one of the most studied materials throughout science. Considering these facts it is interesting that the physical foundations of the unusual high glass forming ability of some of these alloys are only poorly understood. This is probably based on the fact that the glass transition itself, which is the characterizing phenomenon of all glasses, is not understood in terms of its underlying physics. Currently, the question whether the glass transition is a purely kinetic phenomenon or a real phase transition in the limit of infinitesimal small heating or cooling rate is a highly debated topic in theoretical and solid state physics [3, 4]. Up to now a consistent answer to the problem is missing and it seems that the phenomenon of glass formation needs new theoretical as well as experimental approaches [5].

Experimentally a variety of characterization methods for glasses is available. The most established methods are differential scanning calorimetry (DSC) [6–8], conventional dilatometry (DIL) [9–11] and dynamic mechanical analysis (DMA) measurements [12–14]. In all those experimental techniques the transformation behaviour of the supercooled liquid into a glass upon cooling is studied on relatively short time-scales. Therefore, the assessment of the equilibrium behaviour is only possible by using time or temperature extrapolations of mostly empirical formulas [15]. A main objective of the present work was the extension of measurements on metallic glasses to the long-time and low-temperature regime. To achieve this objective the development

---

of a highly stable dilatometer based on laser-interferometry was the foundation of all measurements in this work. The new device allows for the first time to study sub- $T_g$  volume kinetics in bulk metallic glasses with minimal disturbing influences on the specimen. Furthermore, with the very high length change resolution in the sub-100 nm regime it is possible to measure volume changes upon very small temperature steps. This capability enables new approaches for the determination of the glass transition temperature.

The present work tries to asses different kinetic and equilibrium aspects of the metallic glasses under investigation to provide a comprehensive picture of the important phenomena. At first the volume kinetics in the glassy state is examined by isothermal long time measurements. The obtained results are compared with DMA measurements to assess differences in the probed kinetics. To get deeper insights into the volume evolution on an atomic scale positron annihilation measurements using a high-intensity positron beam are presented and discussed in relation to the dilatometric results. Additionally to the kinetic measurements the equilibrium volume of a metallic glass is studied on very long timescales to assess the glass transition in equilibrium. To complete the range of investigated phenomena a low-temperature crystallization study, using a specially developed dilatometric measurement technique of temperature modulated dilatometry is also presented.

This work was realised in cooperation with the following institutes:

- Leibniz Institute for Solid State and Materials Research, Dresden, Germany (specimen production)
- Institute of Micro and Nanomaterials, Ulm University, Germany (specimen production)
- Workgroup on Physics of Functional Materials, Univeristy Vienna, Austria (DMA measurements)
- NEPOMUC positron beam line at FRM II, TU München, Garching, Germany (positron measurements)

Parts of this work can be found in the following publications:

- M. Luckabauer, U. Kühn, J. Eckert, and W. Sprengel, Specific volume study of a bulk metallic glass far below its calorimetrically determined glass transition temperature, Physical Review B **89**, 174113 (2014). (Sec. 5.2)

- H. Mehrer, M. Luckabauer, and W. Sprengel, Self- and Solute Diffusion, Interdiffusion and Thermal Vacancies in the System Iron-Aluminium, Defect and Diffusion Forum **333**, 1 (2013). (Sec. 4.4)

The following talks at conferences were given in the course of this work:

- Luckabauer, M.; Wunderlich, R.; Fecht, H.-J.; Sprengel, W., Direct measurements of reversible free-volume formation in bulk Zr<sub>56</sub>Al<sub>7</sub>Cu<sub>24</sub>Ni<sub>10</sub>Co<sub>3</sub> glass below the glass transition temperature, 62nd Annual Meeting of the Austrian Physical Society in Graz, Austria. (Sept. 18<sup>th</sup>, 2012).
- Luckabauer, M.; Kühn, U.; Eckert, J.; Sprengel, W., High-resolution laser dilatometry applied to reversible relaxation phenomena in a Zr-based bulk metallic glass, 20th International Symposium on Metastable, Amorphous and Nanostructured Materials (ISMANAM) in Torino, Italy (July 2<sup>nd</sup>, 2013).
- Luckabauer, M.; Kühn, U.; Eckert, J.; Sprengel, W., High-resolution laser dilatometry: Volume equilibration in a bulk metallic glass, DPG Spring Meeting in Dresden, Germany (April 3<sup>rd</sup>, 2014).



---

## 2 Terminology and Applied Models

---

In the first part of this chapter the terminology, necessary for a consistent understanding of the presented measurements and the results in this work is briefly defined. The most important term in this context is probably the term "relaxation" because it is sometimes misused to describe different phenomena. In this work only the standard physical definition is used and therefore, the difference to equilibration phenomena is emphasized. In the second part the mathematical and physical details of the models used to describe low-temperature volume equilibration are presented.

### 2.1 The glass transition

Glass formation can be observed in a variety of systems ranging from naturally found or engineered silicate glasses over polymeric plastics to metallic systems. In contrast to their chemical diversity all glass forming systems show the physical phenomenon of a glass transition. This process is characterized by a nearly complete kinetic arrest in the structure when the liquid material is deeply undercooled. The macroscopic behaviour changes from a liquid to a solid without an obvious sharp change in the thermodynamic variables like volume or energy. This is puzzling because such a dramatic change in the mechanical properties without an underlying phase transition is hard to imagine. On the other hand, the structure of the glass is really indistinguishable from the liquid. Therefore, the solution to the glass transition problem must be rooted in the kinetics of the glass. Naturally, the investigation of glasses started from the liquid phase because

of the well described and theoretically predictable behaviour of liquids. Actually there are theories as well as a variety of measurement techniques available for the liquid and the supercooled liquid state above the glass transition range. The reader here is referred to Refs. 4, 16, 17 for further information on this temperature regime.

At the point in the cooling process of the glass where the structural rearrangements in the liquid become slower than the cooling rate the systems falls out of thermodynamic equilibrium and all measurements become time-dependent. This behaviour is called ageing and is a characteristic feature of glassy materials. As temperature decreases the equilibrium behaviour becomes more and more difficult to assess and therefore, most available data are restricted to non-equilibrium measurements [18]. In view of these difficulties experimental evidence for the existence of a thermodynamic phase transition underlying the glass phenomenon remained so far an open question [4, 119]. Thus, prospective research on the phenomenon of the glass transition must be aimed to extend the experimental measurements to long-time, low-temperature equilibrium studies as given in this work. Further perspectives on glassy materials and the glass transition can be found in the book of Wolynes [3].

## 2.2 Relaxation in glasses

In the following some information and basics about the relaxation behaviour of glasses, especially in comparison with low viscosity liquids is given.

### Definition of the term "relaxation"

Physically the term relaxation describes the return of a system to equilibrium after an external perturbation. In the simplest case the response function of the system is linear which is true in cases were the magnitude of the perturbation is small. A classic example for such a response is the stress-strain response function of a spring, known as Hooke's law. The reaction of the spring is a linear function of the input force. Relaxation in complex systems is very similar to this simple example. The model system used in this description should be a liquid (which possibly forms a glass if it is deeply undercooled). The relaxation behaviour of a liquid can be studied by various types of external stimulations like, e.g., electric or magnetic fields, mechanical forces, temperature changes or also in scattering experiments. Here, we will focus on thermal and mechanical stimulations.

To perform a relaxation experiment the liquid must be in thermal equilibrium except for its fluctuations  $\propto k_B T$ . The (thermal or mechanical) perturbation to measure the relaxation time at a given temperature must be small enough to ensure that the system relaxes back to the same equilibrium state as before. This is especially critical when temperature changes are used to study volume or enthalpy relaxation. Only in the limit of very small temperature jumps the equilibrium is conserved and the real structural relaxation time can be measured as the response of the system [3]. As soon as the system starts to equilibrate to another structural state the response is non-linear in  $\Delta T$  and the relaxation time itself becomes time-depended. In the framework of glass science this behaviour is called ageing.

For simple liquids the time domain response function to a perturbation is an exponential function. This kind of relaxation is also called Debye-relaxation and characterized by a symmetric peak in the frequency domain. Such relaxations can be found, e.g., in dielectric spectroscopy experiments. In glass forming liquids due to the increasing particle interaction with decreasing temperature, non-Debey-relaxations are found. The characteristic time domain function is usually a stretched exponential function. This special type of relaxation in glasses originates from the splitting of the liquid like relaxation process into different modes (usually denoted by  $\alpha$  and  $\beta$ ) at a certain temperature in the regime of the supercooled liquid.

The dilatometric measurements presented in this work are solely volume equilibration measurements and not volume relaxation measurements. As a reaction to a relatively large temperature change the system establishes a new equilibrium with measurement time, i.e., severe structural changes occur. In the author's opinion this is a very important difference which often leads to misinterpretations if neglected.

### Spectroscopic techniques

In contrast to direct time domain measurements of relaxation, spectroscopic techniques are better suited to address the microscopic dynamics in glasses and liquids. These methods use different physical principles like mechanical stimulation, thermal stimulation or stimulation due to electric fields but they all share the same measurement principle: the measurement of a linear response function or susceptibility  $\chi(t)$ . Usually the measurement consists of a periodic stimulation with a certain frequency  $\omega$ . The complex susceptibility in the frequency domain is given by

$$\chi(\omega) = \chi'(\omega) + i\chi''(\omega), \quad (2.1)$$

where  $i$  is the imaginary unit. The complex part  $\chi''(\omega)$  is only  $\neq 0$  when there are energy dissipative processes in the system under investigation. In the framework of the linear response formalism it is possible to show that the following equation holds for the dissipative part of  $\chi(\omega)$  [19]

$$S_x(\omega) = \frac{2k_B T}{\omega} \cdot \chi''(\omega), \quad (2.2)$$

where  $S_x(\omega)$  describes the fluctuations in the microscopic variable  $x$  of the system,  $k_B$  is Boltzmann's constant and  $T$  is the temperature. Equation 2.2 is called the fluctuation-dissipation-theorem and fundamentally links the macroscopic dissipations to the microscopic fluctuations of the system. In an experiment either the system temperature or stimulation frequency is varied and  $\chi''(\omega)$  is measured. To measure the structural relaxation time of a glass forming system mechanical spectroscopy, usually in the form of dynamic mechanical analysis (DMA) is commonly performed. A DMA measurement is presented in Sec. 5.1.2. In this section also an analysis in terms of activation energy for atomic motion is shown.

## 2.3 Models for the sub- $T_g$ volume-equilibration in bulk metallic glasses

As most of this work deals with sub  $T_g$  measurements on bulk metallic glasses, a more detailed description on possible mathematical models will be given. Nevertheless such a description can in no way be exhaustive, because of the large variety of different models in literature. In the course of the dilatometric measurements two mathematical descriptions of the isothermal volume equilibration curves proved to be best suitable to capture the behaviour. Therefore, these two models, the simple exponential and the stretched exponential equilibration are described in this section together with possible atomistic interpretations.

### Exponential equilibration

At a thermodynamic temperature  $T_1 > 0$  K a solid in thermal equilibrium exhibits a certain amount of constitutional defects like, e.g., crystal vacancies or interstitial atoms. Those defects are introduced to maximize the configurational entropy and thus minimizing Gibbs free energy  $G = H - TS$ . When the temperature of the solid is

changed to a temperature  $T_2$  a new equilibrium concentration of defects is established. If those defects are volume relevant like, e.g., vacancies their formation is accompanied by an isothermal volume change of the material with time. If one type of defect with a fixed energy barrier  $E_A$  is formed the mathematical description of this volume change  $\Delta V$  with time is an exponential function

$$\Delta V(\Delta T, t) = A(\Delta T) \cdot \left(1 - \exp\left(-\frac{t}{\tau(T_2)}\right)\right), \quad (2.3)$$

where  $\Delta T$  is the temperature difference,  $\tau$  a characteristic time constant at  $T_2$  and  $A$  the process amplitude which is directly linked to the amount of defects by

$$\Delta N = \frac{A}{\Omega} = \frac{\Delta V(\Delta T, t = \infty)}{\Omega}, \quad (2.4)$$

with  $\Omega$  the defect size and  $\Delta N$  the total number of defects formed. In the case of vacancy formation in a crystal this qualitative formulation of migration is well based on the assumption of a random walk process of vacancy diffusion in the solid [20]. It is found that for most processes the energy barrier  $E_A$  is not a function of temperature and therefore its value can be derived by plotting the variation of  $\tau$  with temperature in the form of an Arrhenius plot. Quantitatively this relation is given by

$$\frac{1}{\tau} = \frac{1}{\tau_0} \cdot \exp\left(-\frac{E_A}{k_B T}\right), \quad (2.5)$$

where  $k_B$  is Boltzmann's constant. By plotting  $\log\left(\frac{1}{\tau}\right)$  versus the inverse temperature  $\frac{1}{T}$  a linear function is derived with slope  $-\frac{E_A}{k_B}$  and ordinate intersect  $\log\left(\frac{1}{\tau_0}\right)$ . The information which is included in the constant  $\tau_0$  depends on the thermally activated process under investigation. In the case of vacancy migration it includes a migration entropy, an attempt frequency and geometric constants which account for the specific crystal lattice.

### Multiple processes

The previous assumptions also hold if a certain number of independent equilibration processes with fixed energy barriers during equilibration occur. Mathematically this corresponds to a simple linear superposition of the equilibration functions

$$\Delta V(\Delta T, t) = A_1 \cdot \left(1 - \exp\left(-\frac{t}{\tau_1(T_2)}\right)\right) + A_2 \cdot \left(1 - \exp\left(-\frac{t}{\tau_2(T_2)}\right)\right) + \dots, \quad (2.6)$$

or in the case of  $n$  independent processes

$$\Delta V(\Delta T, t) = \sum_{i=1}^n A_i \cdot \left( 1 - \exp \left( -\frac{t}{\tau_i(T_2)} \right) \right), \quad (2.7)$$

with  $\Delta V(t = \infty) = \sum A_i$ . A practical example and a detailed description of such a multi-process analysis of a dilatometric experiment is given in section 4.4 for the B2-FeAl intermetallic compound.

In the case of bulk metallic glasses it is not clear if the defect type or energy barrier for migration does not change during the experiment. Therefore, the analysis is first based on the visual appearance of the equilibration curve. A simple one-process exponential analysis for a metallic glass is presented in section 5.1.1 and can also be found in literature [21].

## Stretched exponential equilibration

In contrast to the exponential equilibration function the stretched exponential function is commonly found in literature dealing with bulk metallic glasses or amorphous materials in general. In the case of relaxation measurements in the supercooled liquid state by, e.g., dynamic mechanical analysis or dielectric spectroscopy, the stretched exponential function (usually termed *KWW*-function after Kohlrausch, Williams and Watts) is often found as the time domain response function (or more precisely as the functional description of the  $\alpha$ -relaxation process) of the supercooled liquid (see also Sec. 2.2). As long as the system response does not become time dependent there is also a profound theoretical background available in literature [16, 22, 23]. This situation changes completely when the glass forming system is cooled below its glass transition temperature  $T_g$ . Relaxation measurements in this temperature regime are usually strongly time-dependent, the system is "ageing" towards its configurational equilibrium during measurements and therefore a response at a time  $t_1$  will in general not be equal to a response at time  $t_2$ . Because of this challenging behaviour attempts for theoretical descriptions are rare and far from straight forward [24]. Despite these fact there is a large number of publications in which the term relaxation in the sub  $T_g$  region is used for the ageing process itself. Those measurements are usually termed "volume or enthalpy relaxation studies" in the glassy state depending on the measurement technique (DSC, dilatometry or density measurements). Numerous examples for such studies can be

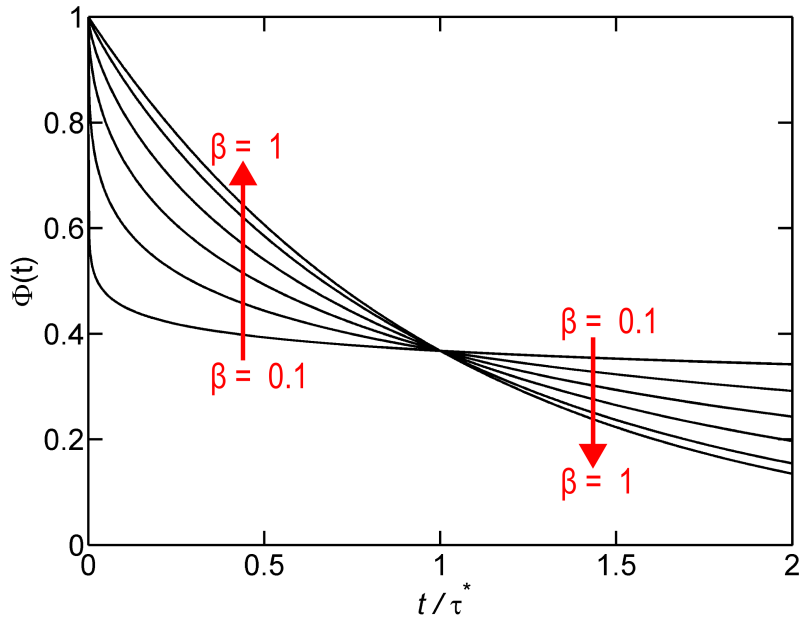


**Figure 2.1:** The stretched exponential function plotted for different  $\beta$  values. The characteristic decay is a faster than exponential decay for times  $< \tau^*$  and slower than exponential decay for longer times.

found in literature [6–9]. In all those experiments the transient response of the system, e.g., the volume change towards (quasi)equilibrium after fast cooling from the supercooled liquid can be described by a stretched exponential function. However, there is no physical evidence that there is a link between these findings and "true" relaxation measurements. Accordingly, the *KWW*-function is used purely empirically based on its ability to deliver good fitting results. It should be emphasized that in the present study reversible volume studies on a bulk metallic glass are analyzed using a stretched exponential analysis. To the knowledge of the author such an approach has so far not been reported.

The stretched exponential function was first introduced by R. Kohlrausch [25] to empirically describe the non-exponential discharge of a Leyden jar in the mid-19th century. It was reintroduced by Williams and Watts to describe non-symmetric dielectric relaxation results [26–28]. The basic form of the function reads as follows:

$$\Phi(t) = \exp\left(-\left(\frac{t}{\tau^*}\right)^\beta\right). \quad (2.8)$$

Herein,  $\beta$  is the so called stretching exponent and  $\tau^*$  is a characteristic time constant.

The amplitude in Eq. 2.8 is arbitrarily set to 1. In most experiments  $\beta$  is found to be between 0 and 1 but it is not limited to this range by any mathematical constraint. For  $\beta = 1$  the function is identical to the exponential function. For  $\beta < 1$  the function shows a faster than exponential decay before its amplitude reaches a value of  $e^{-1}$  and a slower than exponential decay for longer times. In Fig. 2.1 stretched exponential functions for different  $\beta$  values are shown using a time axis normalized to the characteristic time constant  $\tau^*$ .

### Reversible volume equilibration in glasses

As already mentioned, beside relaxation measurements where some theoretical basis is emerging, the *KWW*-function is often used on a purely empirical basis for the fitting of volume or enthalpy changes with time. In the following a closer look on possible mathematical and physical interpretations of the stretched exponential function is presented.

To start off we go back to Eq. 2.7 were the system evolution under the assumption of  $n$  independent volume affecting defect diffusion mechanisms is described. For this function the atomistic basis is quite clear: Every defect has its defined size, activation energy and therefore a well-defined time constant for a given temperature. The situation in glasses is different because a distinct, well-defined defect size is hard to imagine. A possible approach would be the consideration of a continuous range of defect sizes or generally speaking so-called free volume, which enables atomic motion. For a given temperature this range is well-defined, equivalent to the well-defined kind and amount of defects in the crystalline material. Because every defect has its own time constant of migration in the crystal the equivalent picture in the glassy state is a certain continuous distribution of time constants (or defect sizes) for a given temperature. In mathematical terms this means to take the limit in Eq. 2.7 as  $n$  approaches  $\infty$  while preserving the given total amplitude

$$\sum_{i=1}^n \exp\left(-\frac{t}{\tau_i}\right) \xrightarrow{n \rightarrow \infty} \int_0^\infty \rho(\tau) \exp\left(-\frac{t}{\tau}\right) d\tau. \quad (2.9)$$

Together with the normalization condition  $\int_0^\infty \rho(\tau) d\tau = 1$  this is the exact mathematical definition of the stretched exponential function

$$\int_0^\infty \rho(\tau) \exp\left(-\frac{t}{\tau}\right) d\tau = \exp\left(-\left(\frac{t}{\tau^*}\right)^\beta\right) = \Phi(t). \quad (2.10)$$

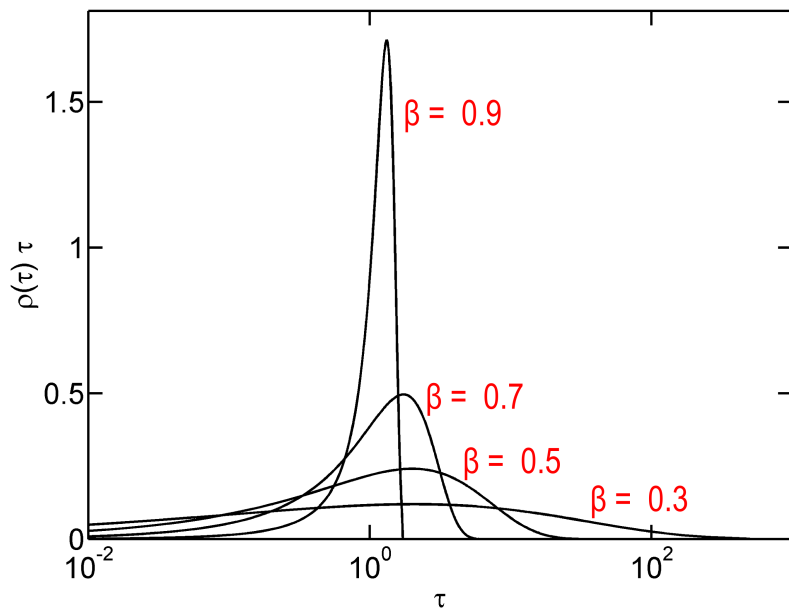


**Figure 2.2:** Four different time constant probability distributions for different values of  $\beta$  and a  $\tau^*$  of 1. The distributions become very broad for small beta values, while they are progressively sharper for larger  $\beta$  values. In the limit when  $\beta = 1$  a Dirac  $\delta$ -function is derived, as expected for the simple exponential function with one distinct time constant.

The function  $\rho(\tau)$  is the probability density function for the time constants  $\tau$ . All the physical information of the system is included in this function. To deduce  $\rho(\tau)$  from the integral in Eq. 2.9 one defines  $\chi = 1/\tau$  and gets the following Laplace transform:

$$\Phi(t) = \int_0^\infty \exp(-\chi t) \frac{\rho(1/\chi)}{\chi^2} d\chi = \mathcal{L}\left(\frac{\rho(1/\chi)}{\chi^2}\right), \quad (2.11)$$

and therefore,  $\rho(\tau)$  is given by

$$\rho(\tau) = \frac{1}{\tau^2} \mathcal{L}^{-1}[\Phi(t)]. \quad (2.12)$$

This calculation was explicitly conducted by Lindsey and Patterson [29]. For the probability density  $\rho(\tau)$  one gets the following expression

$$\rho(\tau) = -\frac{\tau^*}{\pi\tau^2} \sum_{k=0}^{\infty} \frac{(-1)^k}{k!} \sin(\pi\beta k) \Gamma(\beta k + 1) \left(\frac{\tau}{\tau^*}\right)^{\beta k + 1}, \quad (2.13)$$

where  $\Gamma$  denotes the gamma-function. In Fig. 2.2 examples of this functions in the commonly used form  $G(\tau) = \rho(\tau)\tau$  are shown for various values of  $\beta$  on a logarithmic

time scale. These distributions are very broad for small  $\beta$  values and become a Dirac  $\delta$ -function for  $\beta = 1$ .

The fact that all physical information of the system is included in the time constant distribution function defined by Eq. 2.13 shows that the parameter  $\tau^*$  from Eq. 2.8 is a meaningful physical time constant only in the limit of  $\beta = 1$ . In all other cases the time distribution of the system is only describable by knowing both quantities  $\tau^*$  and  $\beta$ .

In a macroscopic experiment only an effective time constant for atomic motion is measurable, so there is a need for a definition of a useful "mean" time constant for atomic motion. Because of the mathematical details of the distribution function Eq. 2.13 this is not a simple task. Johnston et al. [30, 31] showed in their theoretical paper [31] that the mathematical definition of the mean time constant from Eq. 2.9 has no direct physical meaning. They argued that for real physical systems the probability distributions in Fig. 2.2 should have a high  $\tau$  cutoff. This is very reasonable because infinitely long time constants cannot occur in real systems. With this and some other assumptions from [30] it is possible to define a useful effective time constant  $\tau_{\text{eff}}$  which is accessible in experiments as

$$\tau_{\text{eff}} = \frac{1}{\beta} \cdot \tau^*. \quad (2.14)$$

Although this relation looks rather straight forward, it would have no foundation without the aforementioned considerations and remarks. All glass measurements in this work were analysed according to this interpretation of the stretched exponential function. From the temperature variation of  $\tau_{\text{eff}}$  it is again possible to derive useful activation energies for comparison with other experimental techniques like, e.g., diffusion or DSC measurements. Detailed evaluations with measurement results are given in the corresponding sections in Chap. 5 of this work.

---

# 3 Materials and Methods

---

In this chapter the investigated materials and the experimental methods used are presented. The exact experimental parameters and configurations can be found in the relevant section in the measurement and results chapter (Chap. 5). Because the adaptation and configuration of the laser-dilatometer is a fundamental part of this work, it is not included in this Materials and Methods chapter but is given a chapter of its own (Chap. 4).

## 3.1 Materials and sample preparation

### Bulk metallic glasses

The bulk glass samples were produced via the copper-mould suction casting process [32]. At first a master alloy with the alloying elements is melted in a water-cooled copper crucible under Ti-gettered argon atmosphere. After re-melting the alloy a few times for homogenization it is casted into an evacuated water cooled copper mould. Due to the pressure difference the melt is pressed into the mould and rapidly cooled because of the good contact with the water cooled copper. The attainable cooling rates for a 5 mm zirconium bulk glass rod are 25 to 80 K/s at the bottom of the rod and 17 to 50 K/s at the top [33]. The form of the specimens produced is only limited by the available mould geometries. In this work prismatic specimens with dimensions 40 x 3 x 6 mm<sup>3</sup> (produced at the IFW Dresden) and 40 x 4 x 5 mm<sup>3</sup> (produced at the Institut für Mikro-und Nanomaterialien, Ulm University) were used.

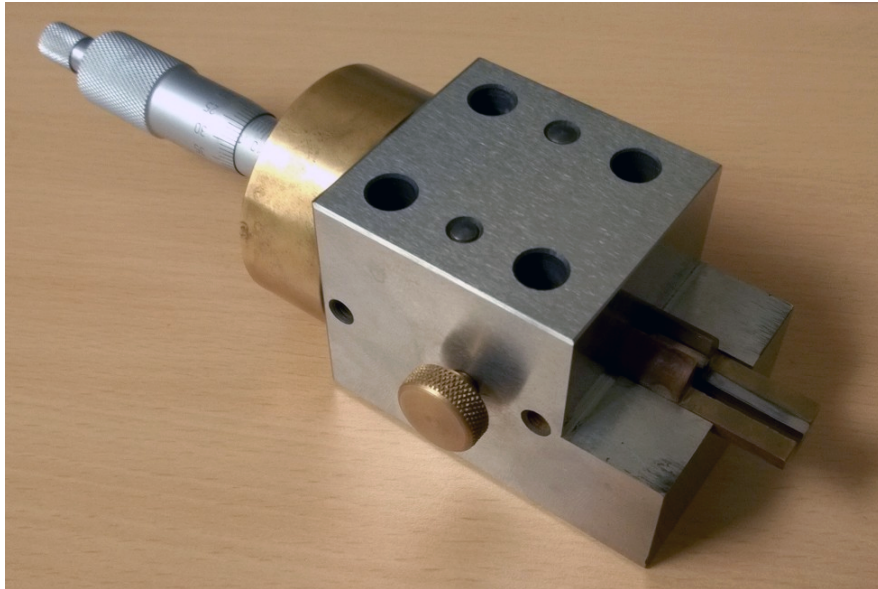


**Figure 3.1:** The device for sample preparation consists of a steel block with a central bore hole for a brass inset which holds the sample. A micrometer-screw is used to shift the inset back and forth to bring the sample surfaces and the reference surfaces into one plane

#### B2-iron aluminium ( $\text{Fe}_{61}\text{Al}_{39}$ )

The intermetallic B2 iron aluminium sample was produced at the former Max-Planck-Institut für Metallforschung in Stuttgart. The high-purity raw materials were melted and cast into a copper mould. After casting the specimen was annealed at elevated temperatures to attain thermal equilibrium. The sample was used for reference and calibration measurements (see. Chap. 4.4).

#### Sample preparation

For the purpose of sample preparation a BUEHLER Isomet low-speed saw with diamond grinding wheels is available at the institute. The necessary L-shaped sample geometry for the laser-dilatometric studies is described in Chap. 4 in detail. After cutting the sample the delicate task of grinding and polishing the two parallel laser reflecting surfaces is conducted with a self-developed grinding and polishing device shown in Fig. 3.1. The device consist of a steel block with two reference planes with a parallelity better than  $\pm 1'$  (minute of arc). The sample is fixed with cyanoacrylate glue inside a brass inset which can be moved precisely back and forth with a micrometer-screw at the back end of the device. The sample surfaces are grinded with abrasive papers which are glued to glass plates for flatness. Polishing is conducted with the

same glass plates but with a polishing cloth attached to it. The finest diamond paste used has a particle size of 1  $\mu\text{m}$ .

Although the reference surfaces are subjected to continuous grinding they have to stay parallel during the course of operation. This means that minimal material loss must be guaranteed by using a very hard material. Because such a material needs special manufacturing skills the device for sample preparation was manufactured at the Erich Schmid Institute of Materials Science in Leoben, Austria. The material used is Böhler S390 high-speed-steel hardened to 65 HRc.

## **3.2 Characterization methods**

### **X-ray diffraction**

Unless otherwise noted in the respective sections of his work, all X-ray diffraction measurements were conducted in-house. For this purpose a BRUKER D8 Advance powder diffractometer with  $\text{CuK}_\alpha$  radiation is available at the institute. Especially when measuring amorphous materials a very low intensity for the diffraction pattern could be expected because of the absence of defined sharp reflexes. Therefore, the cathode current and acceleration voltage for the X-ray tube were chosen to be 40 mA and 40 kV respectively. Together with relatively long measurement times of about 24h for  $2\Theta$  from 20 to 120° the necessary intensity was achieved. However, with this setup the reliable sensitivity for crystalline phases lies in the range of about one to five volume percent. Starting nucleation or small fractions of nano-crystals cannot be detected with this device.

### **Differential scanning calorimetry**

Differential scanning calorimetry (DSC) measurements for this work were conducted at the Institute for Experimental Physics at Graz University of Technology. The DSC used was a NETSCH DSC 404C equipped with high-purity dried and titanium gettered argon atmosphere. A heating rate of 5 to 20 K/min was used for all measurements.

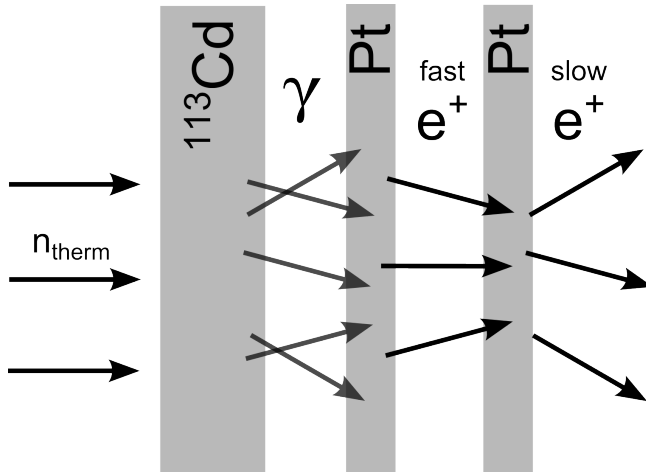


**Figure 3.2:** The slow positron generation process at the FRM II. High intensity, high energy gammas are produced by n-capture in a  $^{113}\text{Cd}$  target. These gammas are converted in a Pt target to electron-positron pairs. A second platinum foil is used for the moderation to 1 keV.

### 3.3 Experimental methods

#### Positron annihilation spectroscopy

Positron annihilation measurements were conducted at the high intensity positron source NEPOMUC at the Heinz-Maier-Leibnitz neutron source in Garching, Germany. The positron generation is based on the capture of thermalized neutrons from the reactor in  $^{113}\text{Cd}$  which gives rise to the generation of high intensity, high energy gamma-radiation (up to 9 MeV). This radiation is used for pair production in a platinum target. The generated high energy positrons (800 keV) are moderated in a second platinum foil. The principle is shown in Fig. 3.2. Platinum shows a positive work function for positrons, therefore with a transmission factor of about  $10^{-4}$  thermal positrons are emitted from the Pt-foil. These positrons are than accelerated to give a mono-energetic positron beam in the energy range from 1 to 30 keV. The intensity of the remoderated positron beam, used for annihilation experiments is  $5 \cdot 10^8$  positrons per second. The sample stage is located in an UHV chamber. Sample heating is realized by a halogen-bulb located underneath the sample. Temperature measurement and control is performed with a calibrated pyrometer. For the detection of the 511 keV annihilation gammas high-purity germanium detectors with an energy resolution of 1.35 keV (at 511 keV) are used. Further details on the experimental setup can be found in Refs. 34–37.

### - Doppler broadening spectroscopy

When a thermalized positron annihilates in a certain material with an electron, the emitted gamma quanta contain information about the electron impulse (or energy). An impulse of the annihilation electron leads to an energy shift of the annihilation  $\gamma$ -quanta of

$$\Delta E = \pm \frac{p_z c}{2}, \quad (3.1)$$

with  $p_z$  the impulse component of the electron parallel to the emitted photon direction and  $c$  the speed of light. The energy shift is positive for one of the 511 keV  $\gamma$ -quanta and negative for the other one depending on the impulse direction of the electron in the laboratory system. This is the reason why the measurement technique is called Doppler broadening in analogy to the variable frequency of a moving wave-source first described by Christian Doppler. Because the impulse of the thermalized positron can be neglected (energy in the range of some tens of meV) the energy shift of the radiation contains solely information about the annihilation electron. Low energy shifts are caused by weakly bonded valence electrons, while higher energy contributions are caused by annihilation events with core electrons. The binding energy of core electrons is element specific and therefore a change in the high energy shift region can correspond to a change of the chemistry of the environment of the annihilation site. To further improve the measurement accuracy, especially in terms of chemical sensitivity, an annihilation event only counts to the measured energy spectrum when both annihilation quanta according to Eq. 3.1 are detected in a certain time window. This method assures that no secondary  $\gamma$  radiation, not originating from annihilation events, counts to the spectrum and the method is therefore called coincident Doppler-broadening spectroscopy. It increases the signal to noise ratio up to  $10^5$  so that the rare high-electron momentum annihilation events are also accessible.

### - S and W - parameter

To quantitatively capture the aforementioned different energy shift regions the so called S (shape) and W (wing) parameter is defined. The S-parameter defines the energy peak shape around the 511 keV maximum and can be defined as:

$$S = \frac{\sum_{i=-\delta E}^{i=+\delta E} N_i}{\sum_{i=1}^{i=end} N_i} \quad (3.2)$$

Where  $-\delta E$  and  $+\delta E$  defines a small, usually symmetric energy window around 511 keV, which is schematically shown in Fig. 3.3. The window size is chosen according to

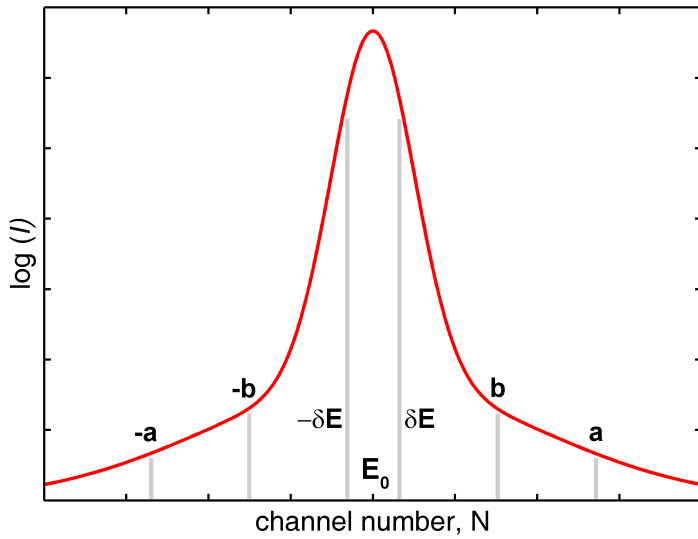


**Figure 3.3:** Schematic energy annihilation peak for positrons. The marked intervals correspond to the energy widows used for calculating the S-parameter ( $-\delta E$  and  $+\delta E$ , Eq. 3.2) and the W-parameter ( $a$  and  $b$ , Eq. 3.3).  $E_0$  is the 511 keV maximum.

the energy levels of the valence electrons in the investigated material. Usually about half the annihilation events count for that region, so that typically the S-parameter varies around 0.5. The discrete sum originates from the electronic recording of the energy spectrum in a multi-channel analyser. Each channel contains the counts  $N_i$  for a distinct energy window. The energy window should correspond to the energy resolution of the detector in use. In the Doppler broadening experiments energy shifts of at most 10 to 20 keV are expected. This directly entails the need for high resolution detectors such as high-purity germanium. The S-parameter is a measure of the annihilation events with valence electrons and therefore a change in this parameter is attributable to a change in local free volume in the material such as vacancy formation in crystalline solids.

The W-parameter is a measure of the chemical environment of the annihilation event and can be defined as:

$$W = \frac{\sum_{i=E_0-a}^{i=E_0-b} N_i + \sum_{i=E_0+b}^{i=end} N_i}{\sum_{i=1}^{i=end} N_i} \quad (3.3)$$

Where  $E_0 = 511$  keV and  $a$  and  $b$  defines symmetric energy windows at the lower and higher energy wing of the annihilation peak as shown in Fig. 3.3.

In a coincident Doppler broadening experiment the recorded spectrum is evaluated

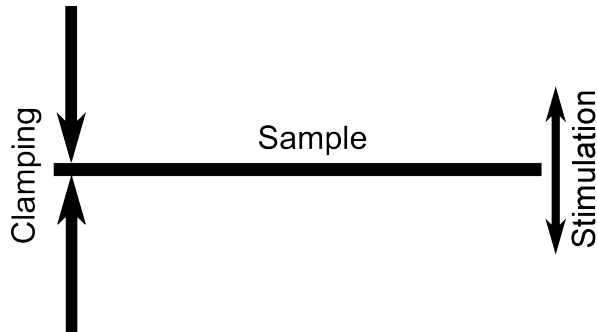


**Figure 3.4:** The single cantilever measurement principle in the DMA. The sample in the form of a flat plate is clamped on one side and attenuated at the other end.

relative to a reference material, usually a constituent of the investigated material:

$$F = \frac{N_{i,material}}{N_{i,reference}}. \quad (3.4)$$

This is necessary because the absolute changes, especially at higher energy shifts, are very small. Changes in  $F$  can therefore be interpreted as changes in the annihilation probability with core electrons from the atoms of the reference material.

## Dynamic mechanical analysis (DMA)

For all DMA measurements in this work a Perkin Elmer Diamond DMA was used. The measurement geometry used was the single cantilever setup. In this setup a sample of size  $5 \times 0.5 \times 20 \text{ mm}^3$  is clamped on one side to a fixed sample holder and the other side is connected to the actuator. This is schematically shown in Fig. 3.4. As a protective gas standard purity argon was used. As DMA measurements are very system specific details about the measurement procedure and mathematical evaluation are given in the DMA measurement section of this work (Sec. 5.1.2).



---

## 4 The Laser-Dilatometer

---

In this chapter the basic operation principle of the laser-dilatometer is presented. After a short description of the basic idea the details of the developments necessary to achieve the maximum possible measurement resolution are given and the hardware and software used for control is described. Finally, the performance of the laser-dilatometer is demonstrated by applying it to a vacancy study on the already well investigated B2-FeAl alloy. As these comprehensive test measurements on B2-FeAl are not directly related to the study of specific volume in metallic glasses the detailed study and results are included here within this chapter.

The original idea and setup for a dilatometer based on laser-interferometry was first realized in the work of Frenner et al. at the University of Stuttgart [38, 39]. This same original device with only minor changes was later used in the work of Baier [40], Ye et. al. [21], Lorenzoni [41] and Luckabauer [42]. The starting point for the development of a contactless dilatometer for long time, isothermal measurements were in-situ measurements of volume changes caused by vacancy migration in certain intermetallic compounds. In some of these materials the ratio  $\frac{H_V^M}{H_V^F}$  of vacancy migration enthalpy  $H_V^M$  to vacancy formation enthalpy  $H_V^F$  is larger than 1 [43]. Therefore, it is in principle possible to directly monitor the volume change caused by vacancy equilibration after a fast temperature change in an isothermal measurement. Unfortunately, the amount of vacancies and, as a consequence, the volume change of the sample is usually too small for being accessed by conventional dilatometers. The solution to this problem was the usage of a 2-beam Michelson laser-interferometer which measures the distance of two reference planes on the sample with an accuracy of 1 nm. With the original setup Fren-

ner [38, 39] was able to directly measure vacancy formation and migration enthalpies in a B2-FeAl intermetallic compound on a relatively short time scale confirming results obtained by positron annihilation spectroscopy obtained from long term measurements [43].

This dilatometer in its original configuration was the starting point of the present work. Whilst providing a technical resolution of 1 nm the full potential of the interferometer could not be used for the measurement of physical effects in the specimen because of certain influencing environmental factors. Therefore, the absolute resolution of the original device was limited to the  $\mu\text{m}$  regime. Most of this chapter deals with the overcoming of this drawbacks and the extension of the measurement accuracy to the sub 100 nm range.

## 4.1 General idea and basic principle of operation

The laser-dilatometer basically consists of a vacuum chamber wherein all the necessary parts to support and heat the specimen are installed. In Fig. 4.1 an image of the actual dilatometer setup is shown. The vacuum chamber is placed on a heavy stone table to isolate the measurement from vibrational influences. Through a window on the right hand side the laser beams of the SIOS SP120D interferometer can enter the vacuum chamber. A water-cooled aluminium block is mounted to the outside of the vacuum recipient at the position where the furnace and the sample are located. The water is kept at a constant temperature around room temperature using a HAAKE DC10 thermostat. This step is necessary to avoid significant shifting or tilting of the laser entrance window during operation. A tilting of the window would increase the effective optical way through the window and as a consequence would cause an apparent length change of the sample by changing the phase angle between the two interfering laser beams.

The picture in Fig. 4.1 shows the dilatometer out of operation with the insulating housing removed. During operation the interferometer is placed inside a water cooled polyacrylic-housing to minimize environmental temperature variations induced by the air conditioning of the laboratory. The dilatometer chamber works at a vacuum level of  $< 10^{-5}$  mbar to avoid unwanted chemical reactions of the sample material with air and to preserve the laser frequency. The terminals for the heating current, the

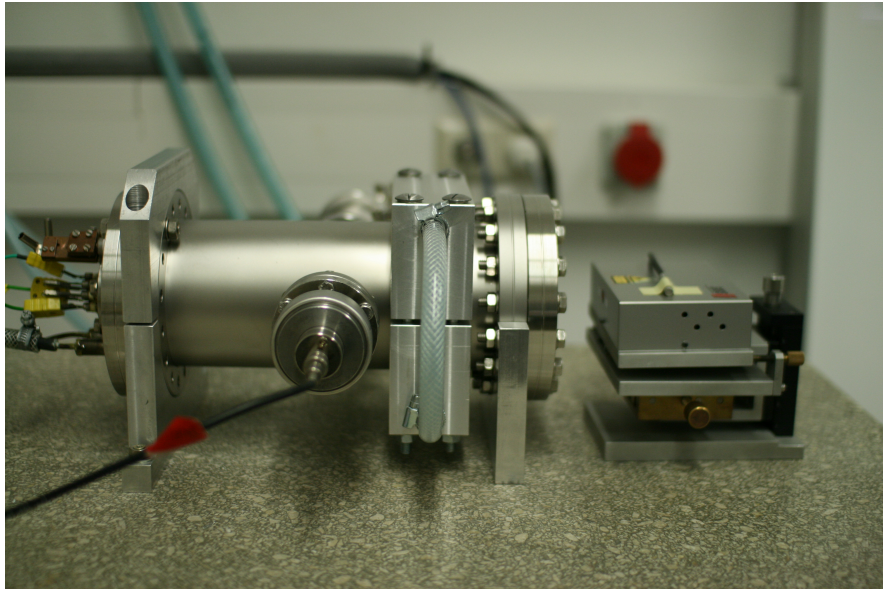


**Figure 4.1:** Laser-dilatometer with interferometer sensor head on the right and vacuum chamber on the left. The vacuum chamber has a diameter of 110 mm and a total length of 310 mm.

thermocouples and the water for cooling the specimen holder are located at the left side of the vacuum chamber in Fig. 4.1.

The SIOS SP 120D is a dual-beam interferometer, i.e., the laser light of a HeNe supply laser is used to realize in principle two independent interferometers which share almost the same optical components. The sensor head shown in Fig. 4.1 on the right is connected via a single-mode glass-fiber cable with the supply and evaluation unit. A drawing of the optical path is shown in Fig. 4.2 [42]. When the polarized laser light enters the interferometer it is first filtered by a polarization filter in such a way that its polarization direction is inclined 45° to the propagation plane. Therefore, in the first beam splitter two beams with opposite polarization but same intensity are created. One beam is the reference beam and the other one is the measurement beam. Both beams pass a quarter-wave plate two times so that their polarization is rotated by 90°. As a consequence the beam which was first reflected passes the beam splitter now and vice versa. The now unaffected reference beam interferes with the measurement beam to elliptically polarized light at the beam splitter 1 which is again converted to linear polarized light by passing through another quarter wave plate. After being split again the sine and cosine part of the intensities is measured by photodiodes. This procedure of detecting the phase shift has the advantage that it is also possible to detect the direction in which the measurement mirror is moving.

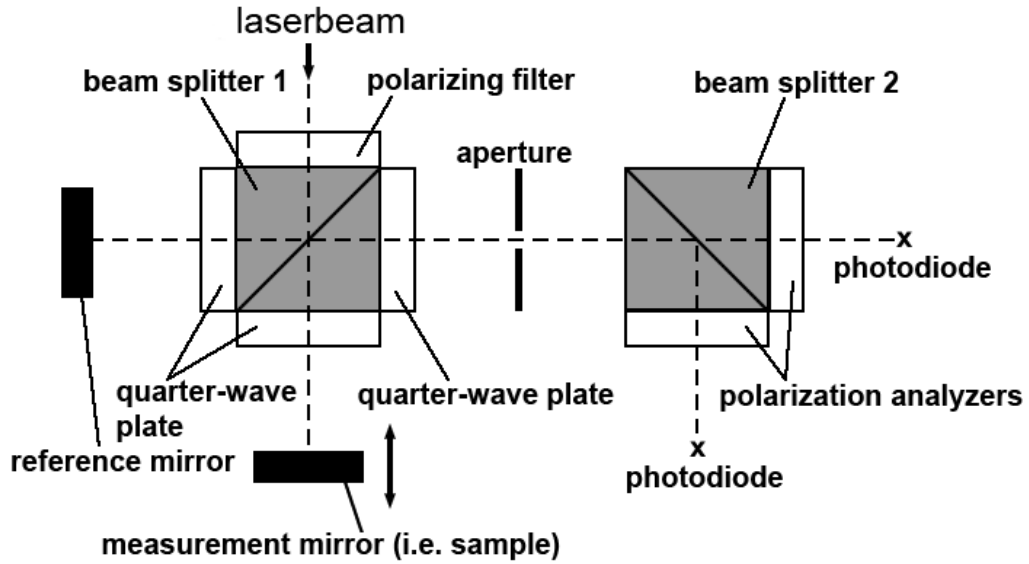


**Figure 4.2:** Drawing of the optical path for one laser beam in the interferometer sensor head. The second laser beam shares the same optical components except for another reference mirror. Picture taken from reference [42].

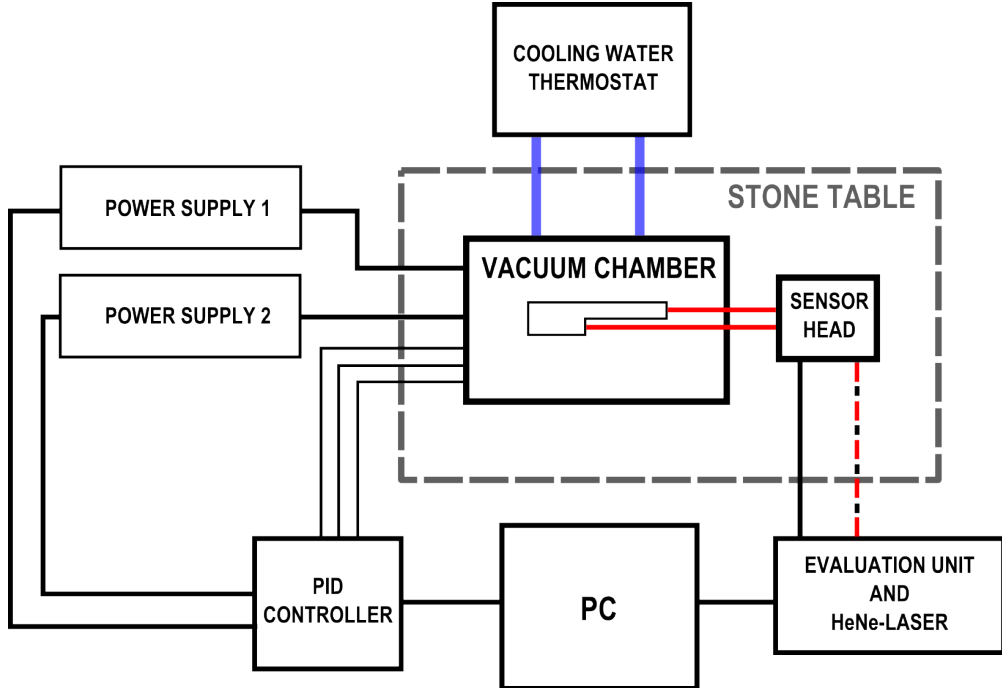


**Figure 4.3:** Block diagram of the dilatometer setup. Inside the vacuum chamber the L-shaped sample is depicted.

## Supply and control units

The laser-light generation, signal evaluation and the data acquisition is conducted outside the interferometer sensor head. This has the advantage that the optical components do not heat up due to power dissipation of the electronic circuitry. On the other hand the connection between the sensor head and the evaluation and control unit is a critical part in the setup because the glass-fibre cable is very sensitive to mechanical and thermal fluctuations. Therefore, it is necessary to prevent the cable from being influenced during operation by a special thermal insulation. In Fig. 4.3 a block diagram of the whole setup is shown. The glass-fibre cable is represented by the black and red dashed line. As mentioned above the vacuum chamber with furnace assembly and sample holder is located on a heavy stone table (grey dashed confined area) together with the interferometer sensor head. A PID controller with two independent control loops is used to control the sample temperatures via two power supply units. Details about the controller and furnace assembly are given in the next subsection. For data storage and monitoring of the measurements a standard Windows based PC is used.

## 4.2 Developments and functional details

To make use of the high specific resolution of the interferometer for real measurements a few crucial points have to be considered:

- The stability and accuracy of sample temperature control
- The stability of environment variables, i.e., air temperature, air pressure and humidity
- The influences of environment variables and their corrections

In this section details about the necessary adaptations and modifications made in the course of this work to improve the original dilatometer setup are given.

### Specimen holder

The specimen holder was redesigned to minimize the influences acting on the sample. As the measurement and the reference plane are both prepared on the sample itself

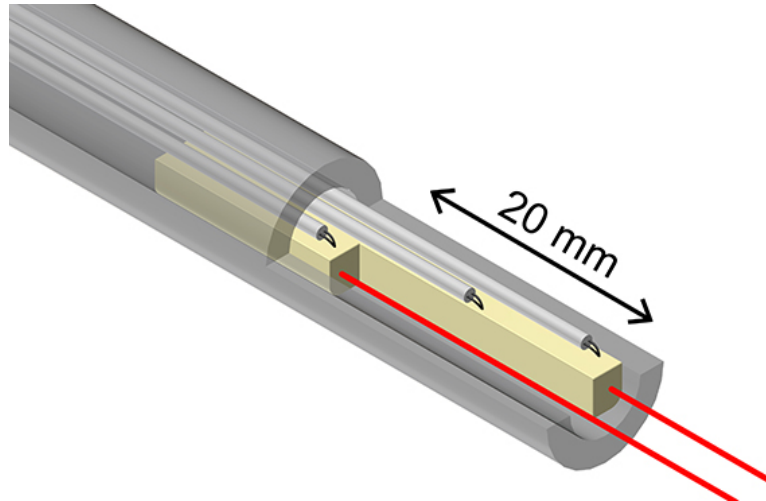


**Figure 4.4:** The foremost part of the specimen holder (grey part). Also shown is the sample with three spot-welded thermocouples and the two laser beams from the interferometer.

the only task of the holder is to support the sample in such a way that no tilting of the reflection planes can occur during a measurement. All other influences like, e.g., thermal expansion of the specimen holder itself or minor vibrations are cancelled out by the fundamental design principle of the dilatometer: Both laser-beams are affected equally by any perturbation so the only net measurement signal is the shifting of the measurement plane relative to the reference plane. This is the reason why no fixing of the specimen is necessary.

Additional criteria which have to be fulfilled by the specimen holder are chemical inertness against the material under investigation and absolute thermal stability in the intended temperature range. In Fig. 4.4 a 3D-CAD representation of the model is shown. It consists of a high density alumina tube (DEGUSIT AL23) with an outer diameter of 10 mm and an inner diameter of 6 mm. It is cut in half in axial direction as shown in the figure. This allows higher heating rates than with a closed tube. The fixing of the holder inside the vacuum assembly is shown in Fig. 4.5. Further details are discussed in the next subsection.

### Temperature control of the specimen

From a physical point of view isothermal measurements have certain useful advantages over conventional, constant-ramp heating experiments. The most important advantage is the possibility of studying processes with very large time constants which are not

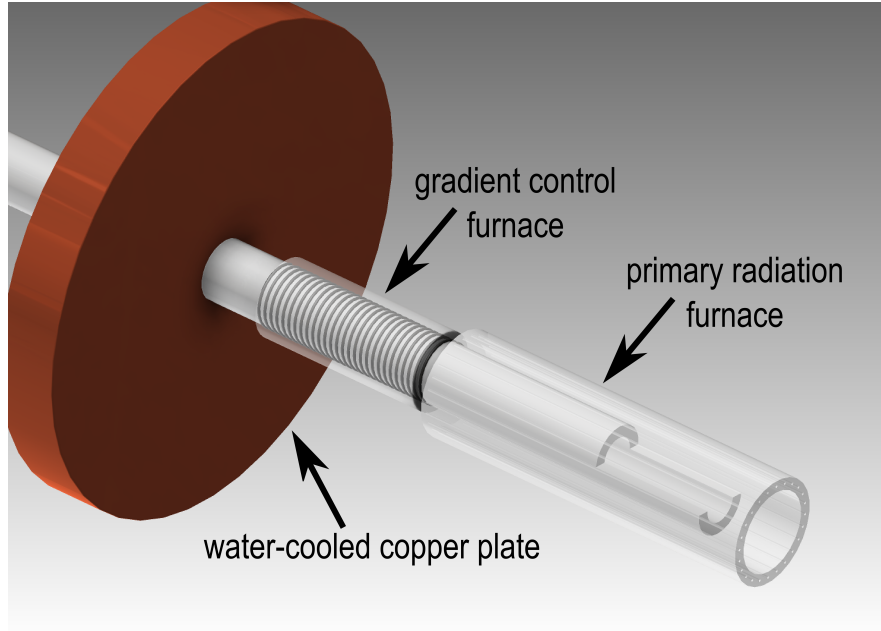


**Figure 4.5:** The specimen support and heating system of the dilatometer. The primary heating furnace is shown without the heating wire for clarity. The connections of the gradient control furnace are also not shown.

accessible in ramp rate experiments simply because the heating rate is usually limited to a minimum of a few K per minute. On the other hand isothermal measurements are a more demanding task for the control equipment in use, especially if a very high measurement resolution in the sub  $\mu\text{m}$  regime is required. For a 20 mm aluminium sample with a thermal expansion coefficient of  $23 \cdot 10^{-6} \text{ K}^{-1}$  a temperature variation of 1 K already causes a length change of 460 nm. This example clearly points out the necessity of a very accurate temperature control mechanism.

The specimen temperature control system developed for the laser-dilatometer can be divided into 2 parts:

- Control of the sample temperature with a radiation furnace
- Control of the temperature gradient within the sample with an auxiliary furnace controlling the heat conduction

The primary sample heating is achieved by a radiation furnace which is shown in Fig. 4.5. It consists of an alumina tube with 28 axial holes through which a 0.25 mm tantalum wire is threaded. Such an assembly has the advantage that no net magnetic field occurs. A direct current from a controllable electric power supply is used as heat source. The furnace is controlled by one loop of a Eurotherm 3504 PID- controller which is fully integrated into the control software.

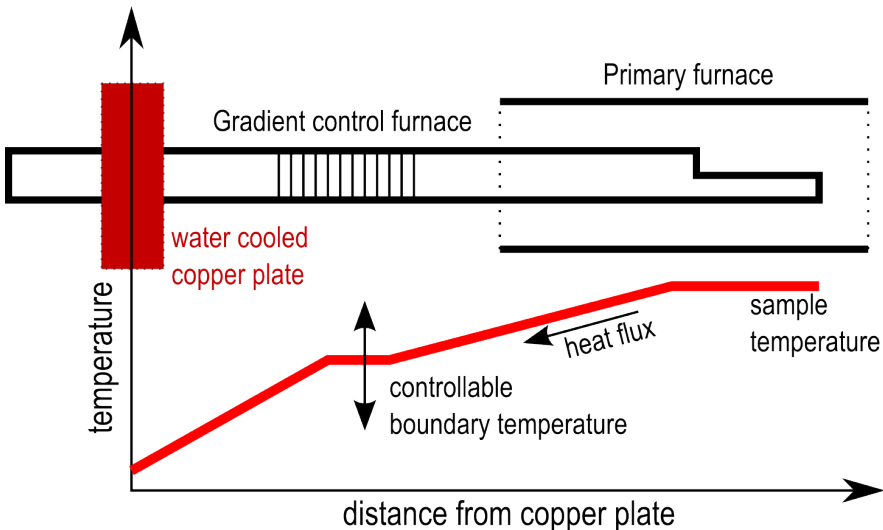


**Figure 4.6:** Schematic explanation of the sample temperature gradient control system. The upper part shows a cross section of the sample holder, the lower part shows the temperature. By changing the boundary temperature the heat flux can be controlled. The red line represents the temperature over the entire specimen holder length.

As shown in Fig. 4.5 the specimen holder is fixed to a water-cooled copper plate. This is necessary because the contact area between the copper and the ceramic tube has to stay at a fixed temperature to prevent thermal stresses due to the different thermal expansion coefficients of the two materials. A drawback of the ceramic material in use is its relatively high thermal conductivity. Whilst this property is very advantageous when it comes to thermo-shock resistance it also creates a significant temperature gradient throughout the sample length. To compensate and even control this problem a temperature gradient control furnace was constructed. The idea is the following: By introducing a fixed temperature boundary condition in the sample holder the heat flux from the specimen to the water-cooled copper plate can be controlled. This principle is clarified in Fig. 4.6. With this setup not only a temperature gradient can be eliminated but, moreover, it is possible to precisely control the temperature difference between the three sample thermocouples (Fig. 4.4) within the measurement uncertainties. To realize a controllable fixed temperature at a certain position of the specimen holder the alumina tube was screw grinded with a diamond grinding device attached to a metal-lathe. With the help of this thread 28 windings of 0.25 mm tantalum wire were wound around the tube and fixed with an alumina sleeve. The windings are schematically shown in Fig. 4.5. The gradient control furnace is controlled by the second loop of the Eurotherm 3504 controller.

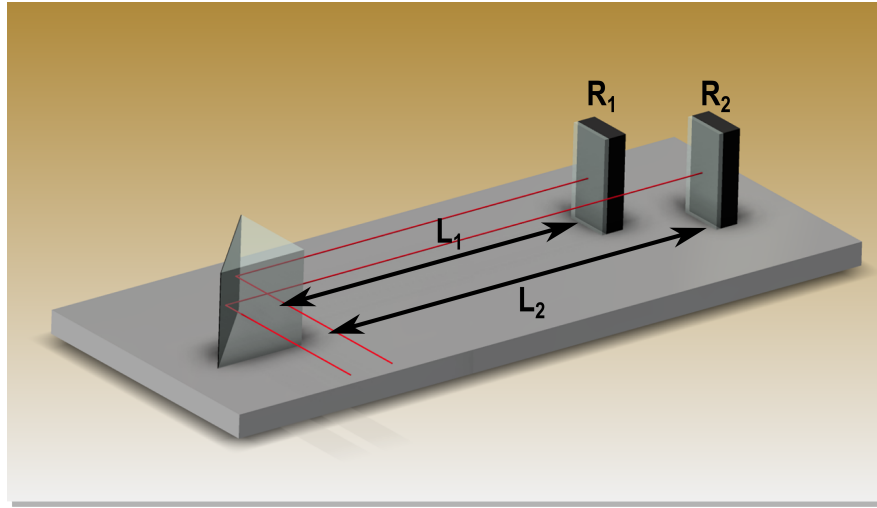


**Figure 4.7:** Schematic drawing of the interferometer baseplate. The primary beam-splitter and the two reference mirrors are shown together with the laser beams. The difference in  $L_1$  and  $L_2$  is the only asymmetry between the two interferometers causing a susceptibility for environment temperature variations during a measurement.

### Cooling water thermostat

A HAAKE DC10 cooling-water thermostat with a temperature stability of  $\pm 0.01$  K is used in the current dilatometer setup. This high temperature stability is necessary because the former water cooler used with a temperature variation of  $\pm 1$  K caused  $\pm 50$  nm ripples in the measured length signal. Although the definite reason for this behaviour is still unclear the most reasonable explanation is that the water temperature change caused a cyclic tilting of the entrance window of the vacuum chamber leading to an asymmetric perturbation of the laser beams. This could be the cause of the apparent length change of the sample.

### Correction of the environmental temperature influences

The environment temperature is the largest influencing factor for the measurement accuracy of the laser-interferometer. The thermal expansion of the components of the measurement device is very large compared to the aimed length change resolution ( $\mu\text{m}$  compared to  $\text{nm}$ ). To cope with these effects the interferometer is constructed in such a way that both laser beams are equally affected by thermal influences. As a consequence the differential signal should be free of any environmental temperature influences. Unfortunately this is only partially the case.

In Fig. 4.7 a schematic drawing of the baseplate of the interferometer is shown. The two reference mirrors  $R_1$  and  $R_2$  are attached to the same baseplate but separated by a distance of 20 mm to match the difference in the focal length of the two laser beams. As a construction material for the baseplate an aluminium alloy was chosen. This is a reasonable choice except when it comes to thermal expansion. The thermal expansion coefficient of the material around room temperature is  $23 \cdot 10^{-6} \text{ K}^{-1}$  which is the largest value found in common metallic construction materials. It should be noted that the original field of application of the interferometer were short time measurements. In such measurements the expansion coefficient of the construction material is not a relevant factor for the resolution.

Each time a measurement is started the measurement signal for both lasers is reset to start with zero length change. Every length change  $\Delta L$  of the sample is than calculated according to

$$\Delta L = S_1(t) - S_2(t), \quad (4.1)$$

where  $S_1(t)$  and  $S_2(t)$  is the measurement signal from laser one and laser two, respectively. As shown in Fig. 4.4 the signal  $S_2(t)$  originates from the more distant reflecting surface. Equation 4.1 is always zero except in the case of a length change of the 20 mm measurement distance in Fig. 4.4. This holds until a temperature change of the interferometer baseplate occurs. Because of the different values of  $L_1$  and  $L_2$ , the reference mirror  $R_2$  moves further away from the beam splitter than reference mirror  $R_1$  when the baseplate expands due to an increase in the environmental temperature. In the case of a decrease in temperature the situation is the same with opposite sign. This behaviour causes a net measurement signal which is not distinguishable from a real measurement signal except the fact that the apparent length change of the sample is an elongation when the baseplate temperature decreases and a contraction when the baseplate temperature increases. To eliminate this influence on the measurements a correction for the extra length change measured by the laser beam 2 was developed. For this purpose the knowledge of the baseplate temperature became necessary. This temperature was already available from the interferometer control unit because it is needed for the correct calculation of the refractive index of the air surrounding the interferometer. Therefore, the only task to do was to measure the thermal expansion coefficient of the aluminium baseplate. For this purpose the length of a reference sample was measured at a constant temperature (around room temperature) while the interferometer was subjected to the normal temperature variations caused by the air conditioning of the laboratory. Because the separation between the reference mirrors  $L_2 - L_1$  is known to be 20 mm the thermal expansion coefficient of the baseplate can

be calculated from the length change signal because at constant reference sample temperature it's the only net signal. It was found that the thermal expansion coefficient is

$$\alpha_{\text{Al}} = (23.0 \pm 0.5) \cdot 10^{-6} \text{ K}^{-1}.$$

With this knowledge it is possible to calculate the correction value for the signal  $S_2(t)$  from the temperature variation of the baseplate. In Fig. 4.8 the temperature of the interferometer during a measurement is shown in black. This signal is damped in comparison with the vacuum chamber surface temperature ( $\pm 0.35^\circ\text{C}$ ) because of the water-cooled poly-acrylic housing placed around the interferometer. The correction factor in nm is calculated according to

$$dL_{\text{corr}}(t) = (L_2 - L_1) \cdot \alpha_{\text{Al}} \cdot (T_{\text{start}} - T(t)), \quad (4.2)$$

$T_{\text{start}}$  is the measurement start temperature and  $T(t)$  the temperature during the experiment. Before the correction factor  $dL_{\text{corr}}(t)$  is calculated the signal is smoothed with a moving average filter to cancel out very fast temperature changes which are not noticeable in the length change signal because of the heat capacity of the aluminium plate. The corrected differential length signal is then given by:

$$\Delta L = S_1(t) - (S_2(t) - dL_{\text{corr}}). \quad (4.3)$$

A plot of the correction factor calculated from the environmental temperature variation in Fig. 4.8 is shown in figure 4.9. This clearly demonstrates the need for such a correction. While the baseplate temperature changes roughly 0.3 K during the experiment the error is larger than 100 nm thus limiting the resolution to effects much larger than the error.

### Practical example of the temperature influence correction

To test the environmental temperature influence correction and the validity of the calculation procedure for the correction factor, various test measurements were made. Especially the exact determination of the thermal expansion coefficient of the interferometer baseplate was the focus of most tests. Here, a practical example of the application of the method in a long time isothermal measurement for a B2-iron aluminide sample is presented. The physics, on which the isothermal length change is based, is quite clear for this material. Therefore, it represents an ideal test system for the laser-dilatometer. The detailed presentation of all measurements for this inter-

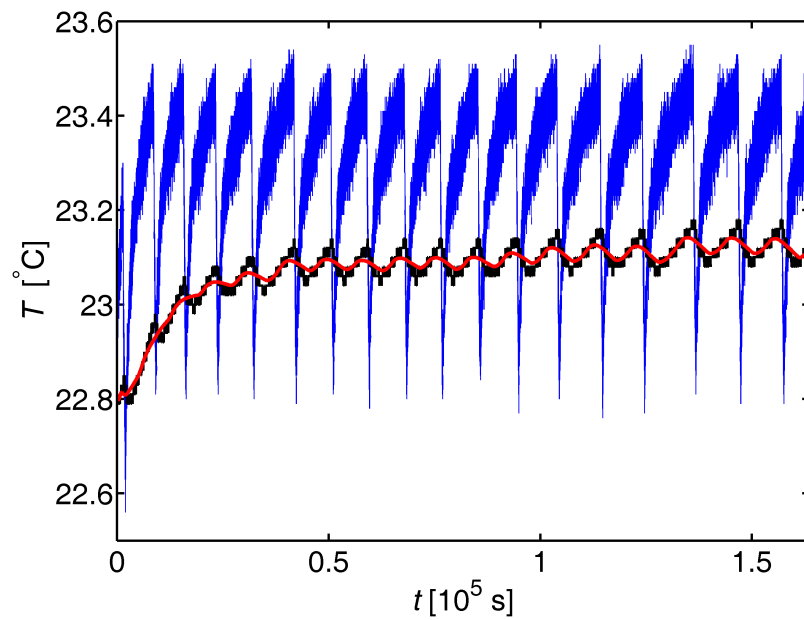


**Figure 4.8:** The temperature variation of the outer surface of the vacuum chamber (blue) together with the temperature variation seen by the interferometer before (black) and after smoothing (red).

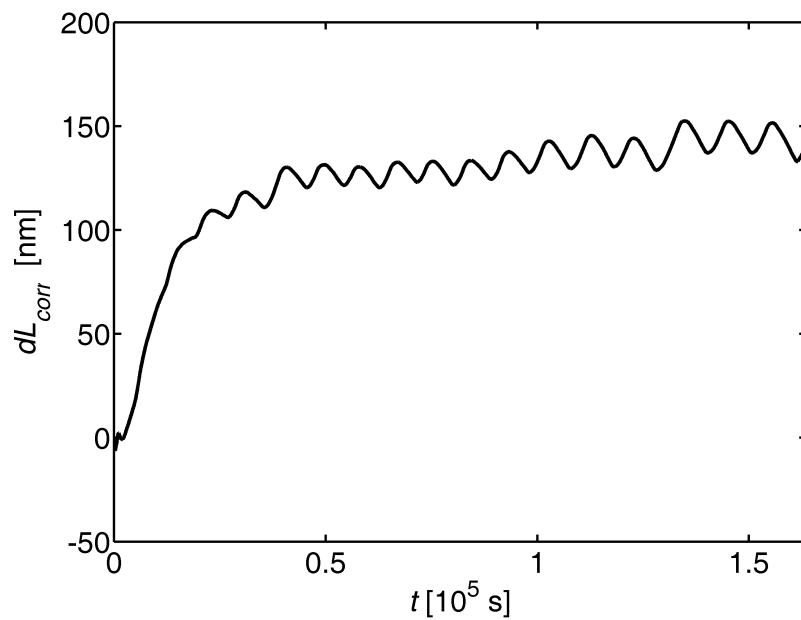


**Figure 4.9:** The calculated length correction for the measurement signal from laser beam number two according to Fig. 4.8.

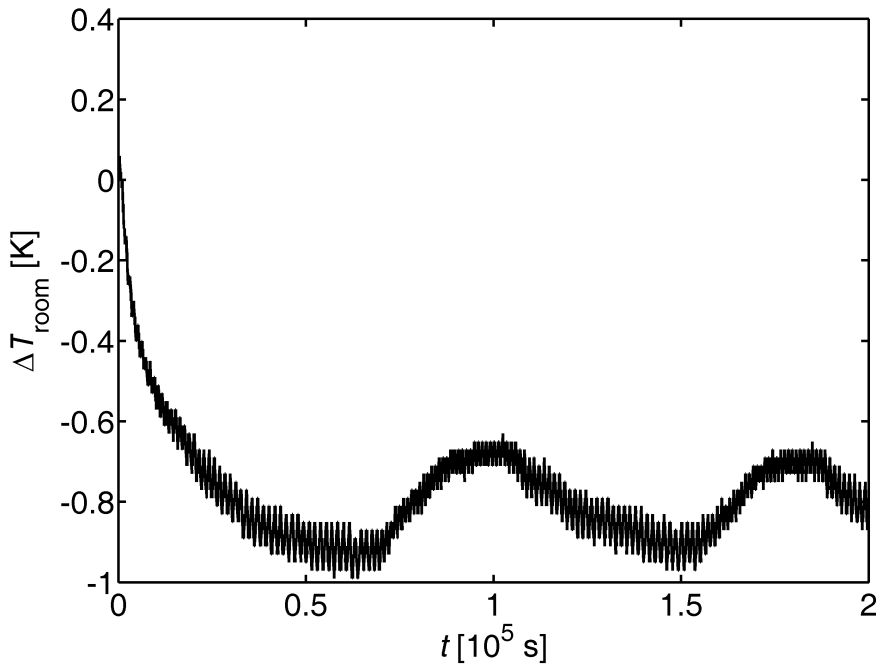


**Figure 4.10:** The interferometer sensor-head temperature variation during an isothermal measurement at 723 K. At first the temperature shows a decrease due to the fact that the sample was quenched from 993 K. The heating is caused by IR-radiation from the sample which can escape from the vacuum chamber through the laser-beam entrance window. Additional variations in the temperature are caused by the day time - night time temperature difference in the lab, with approx.  $8 \cdot 10^4$  s period length and the fast but small temperature variations caused by the air-conditioning. The latter are only recognizable by the low mass Pt-100 temperature sensor and do not affect the interferometer baseplate because of its large heat capacity. Before calculating a useful length change correction it is therefore necessary to attenuate very fast changes. This is done by applying a moving average filter with a filter width of about half an air-condition period to the data.

metallic compound can be found in Sec. 4.4. Here the focus lies on the application of the environment temperature influence correction without going into the details of the physics.

The temperature variation, measured by the interferometer sensor, during one measurement is shown in Fig. 4.10. The time-scale of the experiment is of the order of  $2 \cdot 10^5$  s. Clearly the short time variations caused by the air-condition of the lab are recognizable as a continuous noise with an amplitude of about 0.1 K. Furthermore a variation of the temperature between day and night times of 0.3 to 0.4 K is visible. To calculate the correction factor from this data according to Eq. 4.2 a smoothing based on simple averaging of the temperature signal over approx. half an air-condition

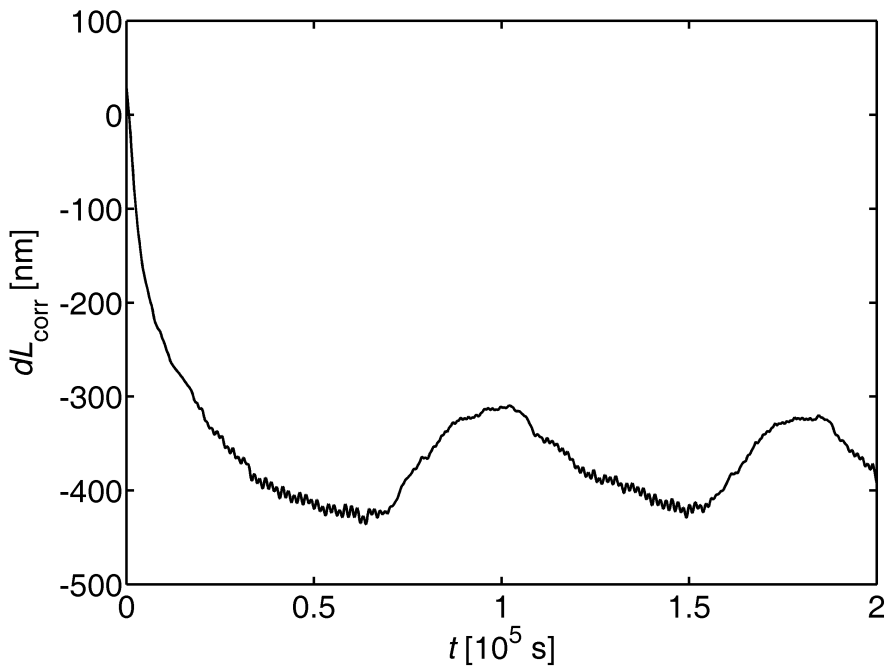


**Figure 4.11:** The calculated length change correction to signal  $S_2(t)$  of the interferometer. The values are linearly proportional to the sensor head temperature variations shown in Fig. 4.10 and calculated according to Eq. 4.2. In comparison with the temperature variation the correction factor does not show up very fast temperature changes due to the application of a moving average filter to the data.

cycle is necessary. This is based on the assumption that the interferometer baseplate exhibits a certain delay of temperature change compared to the Pt-100 temperature sensor which is attached to it for temperature measurement. To capture the real temperature variation of the baseplate the smoothing of the temperature variations to cancel out fast variations is the simplest method. The calculated correction factor for the length measurement signal is shown in Fig. 4.11. It is linear proportional to the temperature variation except for the very fast temperature variations which are attenuated as described. The only remaining step to correct the length measurement signal is the application of Eq. 4.3 to the data. In Fig. 4.12 the un-corrected raw data (blue curve) and the corrected signal (red curve) are shown together. The improvement after the application of the correction is obvious. The red curve is shown together with a fit based on a physical model of vacancy migration which is described in detail in Sec. 4.4. At this point it should only be noted that the application of the environment temperature influence correction really leads to an essential improvement of the measurement resolution. The most important point regarding the process is the fact that it is parameter free and only based on measurable quantities.

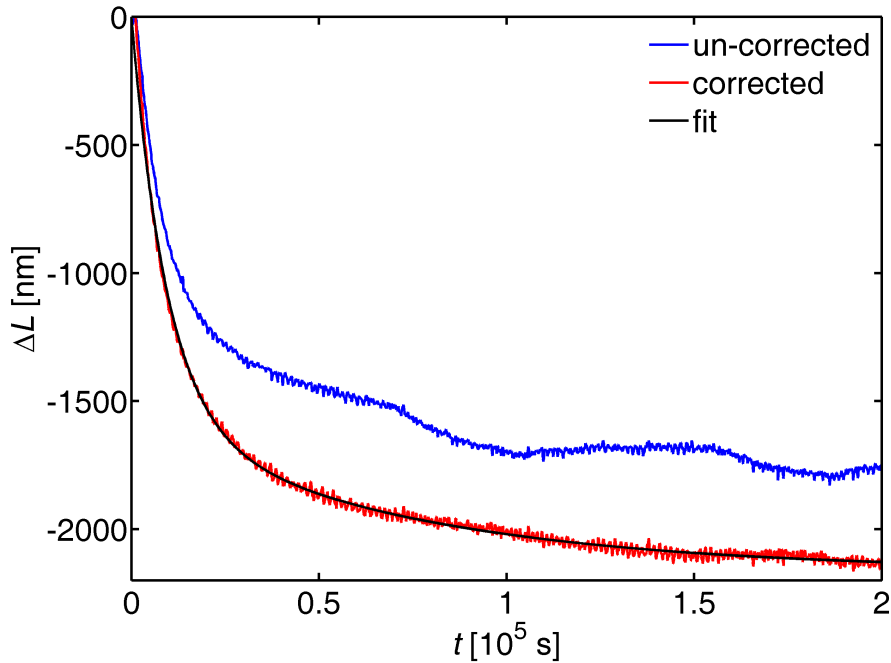


**Figure 4.12:** The example isothermal length change measurement for the correction process in its un-corrected and corrected form for a B2-FeAl sample quenched from a higher temperature. The fit to the corrected signal is based on a physical model of vacancy diffusion in the material and is described in detail in Sec. 4.4 of this work. The temperature variations shown in Fig. 4.10 clearly show up in the un-corrected signal, while they are not noticeable in the corrected curve. At this point it should be noted that the correction process used does not introduce additional uncertainties or errors to the measurement because it is a parameter free calculation based on very accurately measurable quantities.

Therefore, it can be considered as being exact, which assures the universal application in all measurements.

### Control software

The realization of an integrated software environment was another important part of this work because the dilatometer should be as user friendly as possible to be used by everyone to conduct measurements with the device. To do so the complete control software was written from scratch in the programming language C using the software development tool DevCpp. Both the interferometer control unit and the Eurotherm3504 PID controller were attached to a PC by using a RS232 connection. To include the programming of the Eurotherm controller into the software a MODBUS protocol implementation was written to communicate with the PC. The data transmission from the

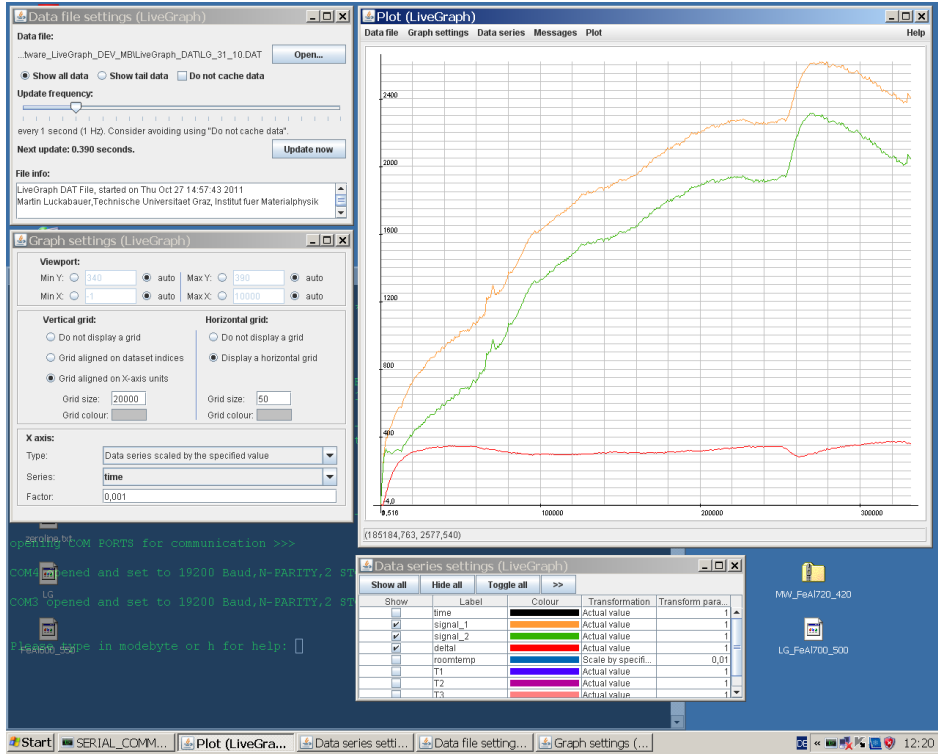


**Figure 4.13:** The dilatometer control software during operation. The real time visualization is done using the free software LiveGraph [44].

interferometer control unit to the PC uses its own simple byte per byte protocol with no error correction or redundancy checks. Therefore, it was necessary to implement a self-developed error correction into the control software. For the purpose of real time visualization the free software LiveGraph [44] is used. In Fig. 4.13 a screen-shot of the software during operation is shown. More information about the control software and its source code can be found in the appendix of this work.

### Sample requirements

In contrast to most available dilatometers the measurement by this dilatometer is contactless meaning the specimen is not affected by any forces acting upon it. This advantage entails that the specimen has to fulfil certain requirements. At first it must be possible to prepare two reflecting surfaces on the sample to get the necessary laser intensity back to the interferometer. Secondly it is important that the surface keeps its reflectivity for long times at the desired measurement temperatures. This is most important if severe structural changes like, e.g., recrystallization are expected close to the measurement temperatures. In this case it is necessary (if this is feasible) to lower

the measurement temperatures. Moreover, up to now the measurements are limited to low vapour pressure samples because of the UHV conditions in connection with elevated temperatures. This is especially important when measuring alloys. In this case every constituent of the material has to fulfil the low vapour pressure condition. In the case of metallic materials the fixing of the thermocouples for temperature control is relatively straight forward by spot-welding the thermocouples to the specimen surface. In other systems like semiconductors the fixing of the thermocouples can be a more sophisticated task. When the thermocouples are not directly attached to the specimen, measurements are still possible but with a lower temperature stability and therefore a lower resolution.

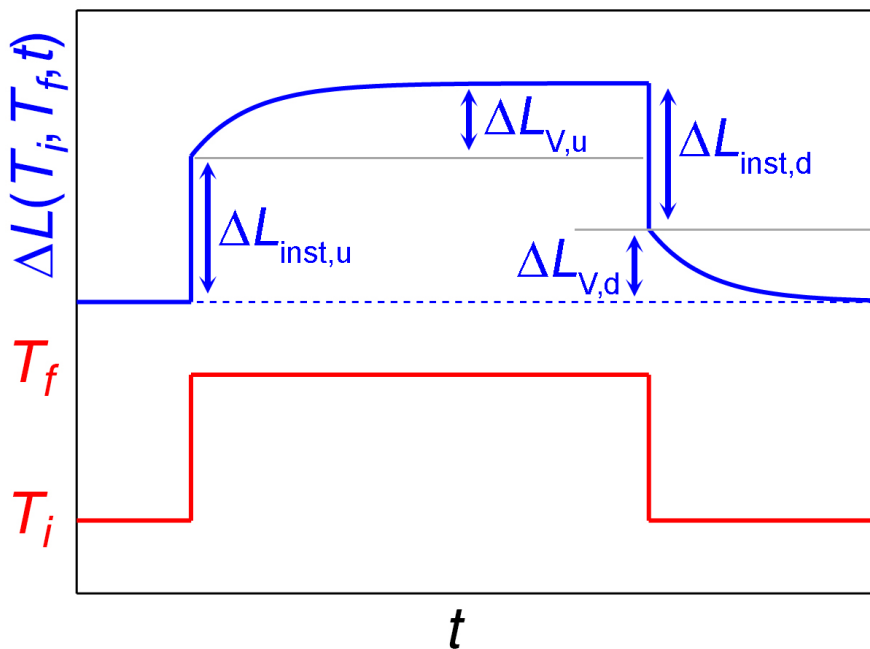


**Figure 4.14:** The schematic representation of the isothermal volume equilibration in a certain material. When the material is in thermal equilibrium at some initial temperature  $T_i$  and the temperature is change to a new value  $T_f$  certain kinetic volume relevant processes can re-establish thermal equilibrium over time (denoted with  $\Delta L_{V,u}$  or  $\Delta L_{V,d}$  if the temperature change is inverse). The  $\Delta L_{inst}$  expansion or contraction symbolizes the quasi instantaneous change of the mean atomic or molecular spacing in the material. If the process studied is fully reversible the equilibrium volume after the measurement at  $T_i$  is the same as for  $t = 0$ .

## 4.3 Dilatometric measurement techniques

With the laser-dilatometer as described in the previous section two measurement modes are possible: Long-time isothermal and long-time isothermal temperature modulated measurements. The basic principles are briefly sketched in the following.

### 1 - Isothermal mode

As already shortly mentioned in the previous subsection isothermal measurements have certain advantages over classic constant heating rate experiments. In the following the implementation and principle of this measurement technique is described.

The isothermal equilibration measurement technique described in this paragraph is schematically shown in Fig. 4.14. When a material is in thermal equilibrium at some

initial temperature  $T_i$  the formation and annihilation rates of thermal defects are equal and therefore, the volume is constant in time except for finite temperature vibrations. To study the equilibration behaviour it is necessary to change the temperature to a new value  $T_f$ . In response to the temperature change the material will expand (or contract) to establish a new equilibrium distance between its constituents. The variation of the equilibrium atomic or molecular spacing with temperature is described by the thermal expansion coefficient usually termed  $\alpha$ . In addition to a new equilibrium mean spacing between the constituents certain kinetic processes will start to re-establish a configurational equilibrium corresponding to the new temperature. These kinetic processes can only be studied in an experiment if the heating time from  $T_i$  to  $T_f$  is much faster than their characteristic equilibration time constants. If this condition is fulfilled one can assess the characteristics of the equilibration process with time. In general one may find a time depended function with a certain number of characteristic parameters

$$\Delta L(t) = f(T_i, T_f, t, p_1 \dots p_n). \quad (4.4)$$

The exact mathematical details of  $f$  strongly depend on the kinetic processes in the material. The parameters  $p_1 \dots p_n$  must not necessarily be time constants, they also can reflect a  $\Delta T$  dependence of the equilibration process or show up as characteristic exponents. In some cases the equilibration behaviour can be captured by a simple exponential function, e.g., in vacancy diffusion processes in crystalline solids. The exact mathematical functions used in this work are given in the respective measurement section. In dilatometric measurements only volume relevant kinetic processes can be studied. Therefore, it is often necessary to use additional measurement techniques to clarify if there are non-volume affecting processes in the material like, e.g., interstitial atoms with a very small lattice relaxation volume.

## 2 – Isothermal mode with temperature modulation

In the previous paragraph it was mentioned that the instantaneous thermal expansion of the material represents the establishing of a new mean spacing between the atoms or molecules in the material. Because the inter atomic potentials strongly depend on the crystal structure or in general on the coordination of atoms in the material it is possible to use the thermal expansion coefficient in equilibrium as a “fingerprint” of the investigated phase. If, e.g., a first order phase transition occurs in the material during a measurement this would cause the expansion coefficient to change. In contrast kinetic processes like defect migration do not have a significant influence on the thermal

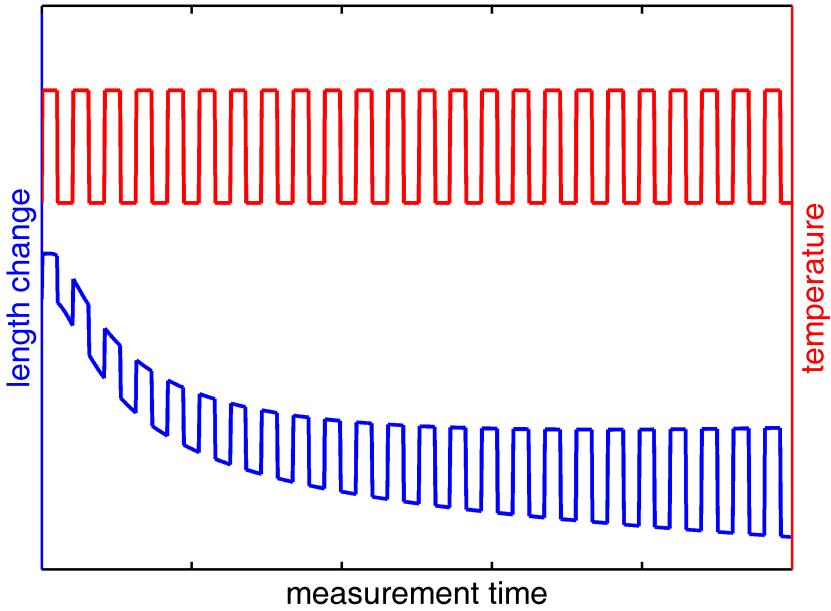


**Figure 4.15:** The basic principle of measuring the thermal expansion coefficient of a material isothermally as a function of time. The red signal represents the temperature which is modulated periodically with small temperature changes (in this work 1-2 K). The blue curve represents a possible length change signal of a material. The global length change amplitude is unaffected by the small periodic temperature modulation, but from the change in the periodic response amplitude possible changes in the thermal expansion can be addressed. In the shown example an increase in the thermal expansion coefficient is visible (the change is shown highly exaggerated).

expansion coefficient at least if their concentration is a few orders of magnitude smaller than the atom concentration of the material. In the course of this work a method for assessing the thermal expansion coefficient at any time in an isothermal dilatometric experiment was developed. This method highly depends on the high resolution capabilities and the capability to perform fast temperature changes of the laser-dilatometer. The starting point is a measurement like the one described in Fig. 4.14. To measure the thermal expansion coefficient during the isothermal phases of the measurement two requirements are necessary:

- The temperature signal has to be modulated in an appropriate way to measure the instantaneous length change of the material.
- The modulation temperature amplitude must be small in order not to significantly change the kinetics of equilibration in the material.

Especially the second point implies the necessity of a very high measurement resolution. The schematic representation of the technique developed for the laser-dilatometer is shown in Fig. 4.15. The isothermal temperature of the sample is modulated with small periodic changes of the order of 1 to 2 K. As a consequence the length change signal is also modulated and the thermal expansion coefficient can be calculated for each modulation step. If a phase change in the material occurs during a measurement the step size in response to the temperature modulation would change. This is indicated in Fig. 4.15 by a growing amplitude of the length modulation. Because most phase transitions are accompanied by a change in the interatomic potentials the described method is universally applicable to various systems. In this work the application of the method to the crystallization behaviour of a bulk-metallic-glass is presented in Sec. 5.4.

## 4.4 Measurements on B2-Fe<sub>61</sub>Al<sub>39</sub>

Before applying the laser-dilatometer to study specific volume equilibration in metallic glasses the experimental setup was tested and checked on the well studied B2-FeAl [45] system with known vacancy equilibration processes. Therefore, these measurements will be discussed in more detail here.

Ordered intermetallic compounds especially those based on the combination of a transition metal like, e.g., nickel, titanium, niobium or iron with aluminium often show outstanding material properties like very high yield strength at high temperatures or superior oxidation resistance in a variety of environments [46, 47]. Beside these favourable properties most intermetallic compounds show a brittle material behaviour at room temperature. For this reason they were used only as precipitation phases in ductile metallic materials like, e.g., Ni-based superalloys for a long time. Recent advances in the field of processing and alloying of these materials now allow to use some of them in their bulk form. A prominent example is the development of titanium-aluminides as light-weight, high-temperature materials [47–49].

Iron-aluminides, mainly with or near the composition Fe<sub>3</sub>Al, were initially investigated as a replacement for stainless steel because of their superior oxidation resistance which is a result of the formation of a thin dense  $\alpha$ -Al<sub>2</sub>O<sub>3</sub> layer on the surface of the material [50]. This layer make these alloys not only oxidation resistant but qualifies them as

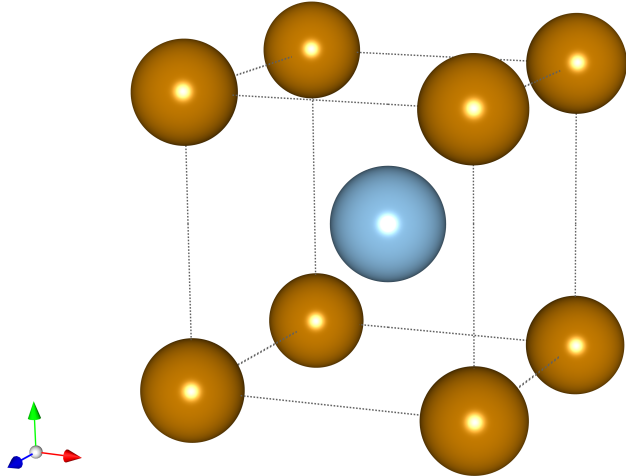


**Figure 4.16:** The B2-crystal structure of FeAl. The primitive unit cell consists of an iron atom at  $(0,0,0)$  and an aluminium atom at  $(0.5,0.5,0.5)$ . The structure was visualized using the software VESTA [53].

construction material in high-demanding applications throughout the chemical industry [51]. Beside these favourable properties B2 iron aluminium compounds suffer from a sharp decrease in strength at temperatures above approximately  $600\text{ }^{\circ}\text{C}$  [47]. This feature, originating from the complex defect diffusion mechanisms in the B2-crystal structure, limits the use of iron aluminides to a relatively low temperature regime compared to other intermetallic compounds. The extension of the maximum application temperature by alloying is an ongoing research topic [52]. To better understand the diffusion mechanisms at all temperatures both macroscopic and microscopic information on the detailed time-temperature behaviour of atom and vacancy migration is needed. In this section measurement results for volume related defect migration and formation at different temperatures in the compound  $\text{Fe}_{61}\text{Al}_{39}$  are presented. Moreover, a detailed comparison to other macroscopic and microscopic measurements is given.

### Thermal defects in the B2 crystal structure

In metallic alloys or pure metals self-diffusion of the constituents is the basic process which establishes an equilibrium vacancy concentration at a given temperature. The driving force for this phenomenon is the minimization of the Gibbs free energy  $G = H - TS$ . The equilibrium concentration is therefore reached when the vacancy annihilation rate at inner or outer surfaces of the material equals the vacancy formation rate. In a

metallic single crystal without any surfaces, a mathematical description of the vacancy migration is possible in the framework of the random walk theory where the mean square displacement (in one dimension) of a vacancy at time  $t_1$  from its position at time  $t_0$  is given by

$$\langle (x(t_1 - t_0) - x(t_0))^2 \rangle = 2D(t_1 - t_0), \quad (4.5)$$

where  $D$  is a diffusion coefficient with an Arrhenius-like temperature dependence. From this starting point the construction of a complete microscopic description of vacancy self-diffusion in metals and metallic alloys is possible. For further details the reader is referred to the text book by Mehrer [54].

The above mentioned assumptions of a random walk process for the description of the motion of point defects no longer hold in the case of stoichiometric intermetallic compounds. In Fig. 4.16 the cubic unit cell of a B2 iron aluminide with strict stoichiometry  $\text{Fe}_{50}\text{Al}_{50}$  is shown. The central aluminium atom is surrounded by iron atoms at the corners of the cube. The structure can also be interpreted as two inter-penetrating simple cubic sublattices. In general, different energies are needed to form a single vacancy on the iron or the aluminium sublattice, respectively. The same is true for the migration process where one sub lattice is favourable because of a lower vacancy migration enthalpy. Beside this antisymmetry in energies additional defects like anti-site atoms play also an important role in minimizing  $G$  in stoichiometric compounds. From a microscopic point of few it is immediately clear that a simple random walk description for defect migration is not feasible if atomic jump processes have different probabilities for different crystallographic directions with respect to the instantaneous position of the vacancy. The simple microscopic formulation for vacancy migration due to Eq. 4.5 is therefore no longer valid in the case of ordered intermetallic compounds. Based on the fact that the vacancy distribution and the vacancy motion is subjected to certain constraints a few atomistic diffusion models can be found in literature [54]. For the iron aluminium system Faehnle et al. [55] calculated activation energies for certain diffusion paths in B2- $\text{Fe}_{50}\text{Al}_{50}$ . Those calculations are in good agreement with experimental data from Mehrer et. al. [56] obtained by tracer diffusion experiments. More details about diffusion in various complex materials especially different types of intermetallic compounds can be found in the text book by Mehrer [54].

## Sample material and preparation

In this work the composition Fe<sub>61</sub>Al<sub>39</sub> was used for all measurements. The samples were brought into the L-shaped geometry by using a low-speed diamond saw. Details about sample preparation procedure can be found in Chap. 3. After carefully polishing the two parallel measurement surfaces, three type-K thermocouples were spot-welded onto the sample surface.

## Measurement procedure and evaluation

For the B2-iron aluminium sample a relatively low vacancy formation enthalpy and a very high migration enthalpy has already been reported [38]. Therefore, a suitable measurement procedure is an isothermal volume measurement after a fast temperature change from an initial annealing temperature at which the sample is in thermal equilibrium. The basic dilatometric measurement idea is described in Sec. 4.3. If it is assumed that each volume affecting process is independently describable by a single exponential function with a time constant  $\tau_j$  then the whole volume change after time  $t$  can be described as

$$\Delta L_V(T_i, T_f, t) = \sum_{j=1}^n A_j \left( 1 - \exp \left( -\frac{t}{\tau_j} \right) \right), \quad (4.6)$$

where  $n$  is the number of independent volume equilibration processes and  $A_j$  are the corresponding amplitudes. It should be noted that this equation only holds if no interaction between the processes occurs. For the B2 structure the validity of Eq. 4.6 would be given, e.g., if no interchange between vacancy diffusion on the two sub-lattices is possible. Impossibility for real systems means that the activation energy for such a process is very high and therefore its probability is very low. If all thermally activated processes obey Eq. 4.6 it is possible to deduce each  $\tau_j$  by fitting the experimental data. Without additional information from complementary measurement techniques this method is usually limited to a maximum of two processes because of the strong interaction between amplitudes and time constants in Eq. 4.6.

All time constants  $\tau_j$  are measured for different  $T_f$  to derive their  $T$ -dependence. If no phase transition occurs in the temperature range under investigation the temperature

variation of every  $\tau_j$  in the case of vacancies should follow an Arrhenius law:

$$\frac{1}{\tau_j} = \frac{1}{\tau_{0,j}} \exp\left(-\frac{H_V^M}{k_B T}\right) \quad (4.7)$$

By plotting the logarithm of  $\frac{1}{\tau_j}$  versus the reciprocal temperature the activation enthalpy for migration,  $H_V^M$ , can directly be deduced from the slope of the linear function. The preexponential factor  $\frac{1}{\tau_{0,j}}$  is simply the ordinate intersect in the Arrhenius plot. The second information obtained from Eq. 4.6 are the process amplitudes  $A_j$  which are directly linked to the defect or, more specifically, to the vacancy concentration  $C_{V,j}$ . To link the length change amplitudes  $\Delta L$  to the volume change amplitudes  $\Delta V$  the following relation valid for isotropic materials is used:

$$\frac{\Delta V}{V} = \frac{3\Delta L}{L} + 3 \cdot \left(\frac{\Delta L}{L}\right)^2 + \left(\frac{\Delta L}{L}\right)^3. \quad (4.8)$$

Higher order terms in  $\frac{\Delta L}{L}$  can be neglected because they are below the experimental resolution limit for  $\frac{\Delta L}{L} = 10^{-6}$  to  $10^{-4}$ . Therefore, the relation reads

$$\frac{\Delta V}{V} \approx \frac{3\Delta L}{L}, \quad (4.9)$$

and was used in this form for the conversion of all measurement results. The measured amplitudes  $A_j$  are then connected to the vacancy concentration  $C_{V,j}$  via:

$$3 \frac{A_j}{A_{j,0}} = \frac{\Delta V}{V} = C_{V,j}^i - C_{V,j}^f = \Delta C_{V,j} \quad (4.10)$$

If the final vacancy concentration  $C_{V,j}^f$  is orders of magnitude smaller than the initial vacancy concentration  $C_{V,j}^i$  and therefore negligible, the equilibrium vacancy concentration at  $T_i$  is approximated by

$$3 \frac{A_j}{A_{j,0}} \approx C_{V,j}^i. \quad (4.11)$$

From statistical thermodynamics the thermal vacancy concentration reads as follows [54]:

$$C_V^{\text{eq}} = \exp\left(\frac{S_V^F}{k_B}\right) \exp\left(-\frac{H_V^F}{k_B T}\right). \quad (4.12)$$

Therefore, the vacancy formation entropy  $S_V^F$  and vacancy formation enthalpy  $H_V^F$  is directly accessible from the temperature variation of the length change amplitudes.

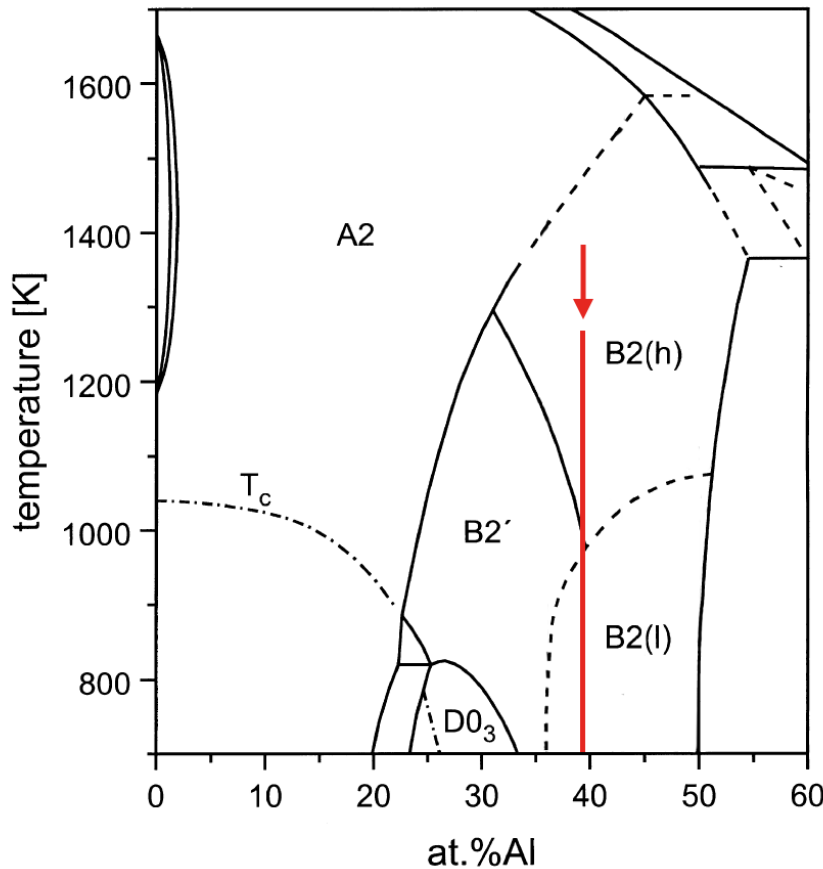


**Figure 4.17:** Iron-rich side of the binary system iron-aluminium after Kubaschewski [57]. According to Kubaschewski the B2 phase field is subdivided into three regions: B2', B2(l) and B2(h). The composition  $\text{Fe}_{61}\text{Al}_{39}$  is indicated by the red line and the arrow.

## Results

### Vacancy formation

All measured isothermal equilibration curves were best fitted by a two-component model. In Fig. 4.18 two measured curves are shown together with their fits and measurement temperatures. As a specific fitting model the following function was used:

$$\Delta L_V(T_i, T_f, t) = A_1 \left( 1 - \exp \left( -\frac{t}{\tau_1} \right) \right) + A_2 \left( 1 - \exp \left( -\frac{t}{\tau_2} \right) \right), \quad (4.13)$$

with two characteristic time constants  $\tau_1$  and  $\tau_2$  and amplitudes  $A_1$  and  $A_2$ . As all fits had a coefficient of determination  $R^2 > 0.99$  the model was considered to completely describe the kinetics, except for very fast processes which are in general not visible

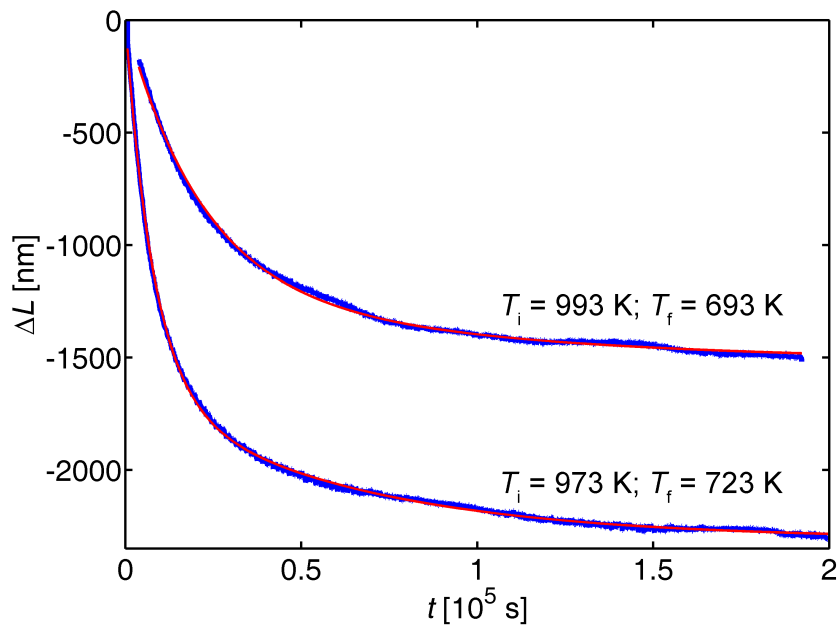


**Figure 4.18:** Isothermal contraction curves for the Fe<sub>61</sub>Al<sub>39</sub> sample after cooling from different initial temperatures  $T_i$ . A strong decrease in the  $\Delta L$  amplitude is observed between 973 K and 993 K. This behaviour can be attributed to the B2(l) /B2(h) transition. While at 973 K the system is still in the B2(l) state this is no longer the case for 993 K indicated by a significantly smaller defect concentration. The red lines are fits using a two component model. For details about the fitting procedure see text.

in dilatometric measurements. The temperature of  $T_f$  for all measurements covered a range between 823 and 693 K and the initial equilibration temperature  $T_i$  was between 993 and 823 K. In Fig. 4.19 the amplitudes  $A_1$  and  $A_2$  are plotted versus the reciprocal initial temperatures  $T_i^{-1}$ . According to the approximation of Eq. 4.11 this diagram directly shows the variation of vacancy concentration with initial temperature. A remarkable feature of the data points in Fig. 4.19 is that the values for  $T_i = 993$  K, i.e., the highest temperature, show a significantly lower defect concentration. This behaviour can be attributed to a phase transition in the B2 structure. In Fig. 4.17 a part of the binary iron-aluminium phase diagram is shown. The actual composition used in this work is indicated by the red line. From this diagram it can be expected that at around 1000 K a transition from the B2(l) to the B2(h) state occurs. Kerl et al. [58] were able to confirm this transition for B2-FeAl by differential dilatometry, i.e., simultaneous measurement of the macroscopic and microscopic volume change of a sample. They concluded that above this transition temperature vacancies are no longer formed as easily as below. This is directly confirmed by the data in Fig. 4.19. The vacancy formation enthalpies for the B2(l) state were deduced from the slopes of

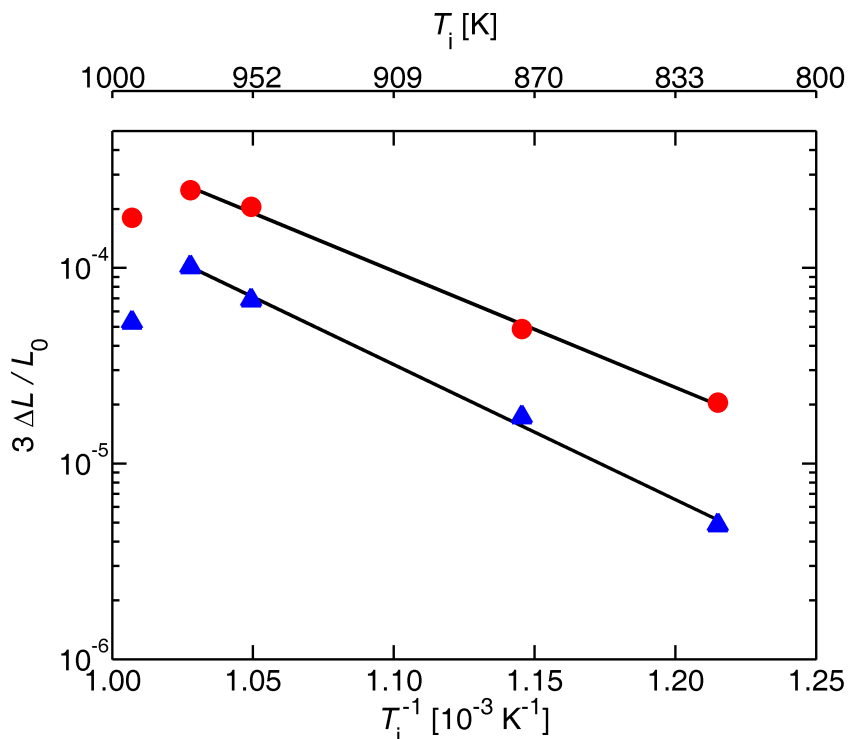


**Figure 4.19:** Variation of the length change amplitudes for the two volume equilibration processes according to Eq. 4.12 under the assumption that the thermal vacancy or defect concentration at the final temperature  $T_f$  is very small compared to the concentration at  $T_i$ . Above approximately 970 K a change in the vacancy concentration is observed this can be attributed to the B2(l) B2(h) transition in Fig. 4.17. A similar result for a slightly different composition was obtained by Kerl et al. [58].

**Table 4.1:** Comparison of vacancy formation enthalpies  $H_V^F$  and entropies  $S_V^F$  with literature data. Values for this work are derived from fits according to Eq. 4.12 (see Fig. 4.19). DIL denotes dilatometric results, PAS positron annihilation spectroscopy and HM hardness measurement. For the PAS and HM results only one defect type was considered.

method	compound	$H_V^{F,1}$ [eV]	$H_V^{F,2}$ [eV]	$S_V^{F,1}$ $k_B^{-1}$	$S_V^{F,2}$ $k_B^{-1}$	Ref.
DIL	Fe <sub>61</sub> Al <sub>39</sub>	1.2 ± 0.1	1.4 ± 0.1	5.8	7.1	this work
DIL	Fe <sub>55</sub> Al <sub>45</sub>	0.9 ± 0.1	1.0 ± 0.1	2.7	4.3	[38]
PAS	Fe <sub>61</sub> Al <sub>39</sub>	0.98 ± 0.07	—	5.7	—	[43]
PAS	Fe <sub>63</sub> Al <sub>37</sub>	1.04 ± 0.07	—	6.5	—	[43]
HM	Fe <sub>61</sub> Al <sub>39</sub>	0.7	—	—	—	[59]

the lines and are shown in Tab. 4.1 together with literature data. In Tab. 4.1 also the formation entropies are listed. Unfortunately, there are no directly comparable measurements for Fe<sub>61</sub>Al<sub>39</sub> available. In comparison with Fe<sub>55</sub>Al<sub>45</sub> all values are considerably higher. This behaviour was in principle theoretically predicted by Fähnle et al. [55] for single vacancies on the Fe-sublattice of the structure. For the positron and hardness measurements only one equilibration process was considered. Therefore, these measurements are difficult to compare with the present results. A comparable single process fit to the data was discarded because of the very weak correlation (low  $R^2$  value). Possible atomistic origins of the formation enthalpies are discussed at the end of this section.

## Vacancy migration

For the vacancy migration enthalpies the time constants  $\tau_1$  and  $\tau_2$  from Eq. 4.13 were evaluated. Their variation with the equilibration temperature  $T_f$  is shown in Fig. 4.20. Only time constants from fits where the corresponding amplitude was larger than 300 nm are shown in this plot. At lower amplitudes the fitting algorithm tends to converge to more than two distinct time constants. Therefore, a meaningful physical interpretation of the two component model Eq. 4.13 is no longer possible. For the data in Fig. 4.20 the initial annealing temperature was 973 K except for the points at  $T_f = 693$  K where the initial temperature was 993 K. From the slopes of the two lines

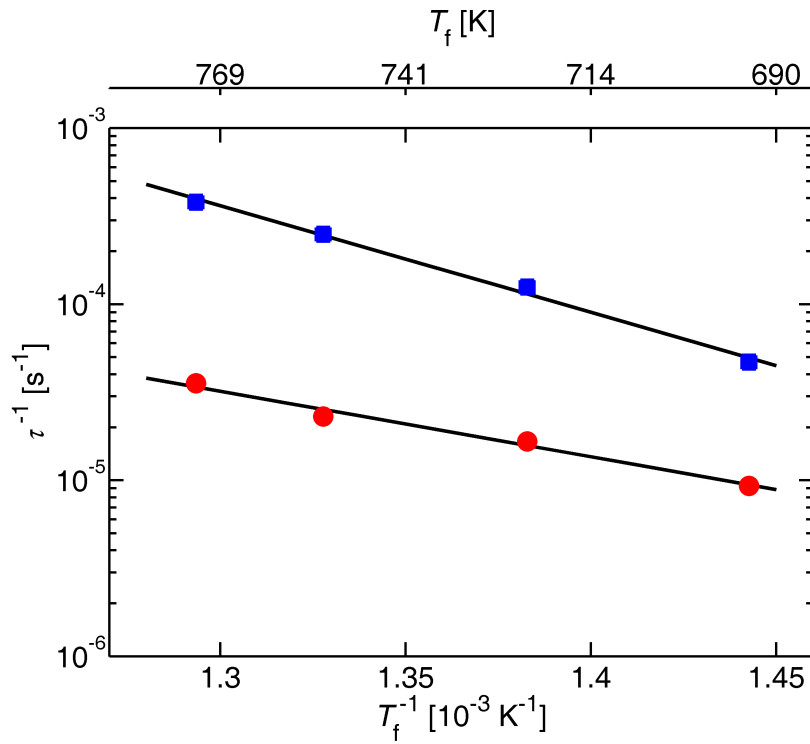


**Figure 4.20:** Arrhenius-plot of the time constants  $\tau_1$  (blue) and  $\tau_2$  (red) obtained by fitting Eq. 4.13 to the measured volume equilibration data.

**Table 4.2:** Comparison of vacancy migration enthalpies  $H_V^M$  and pre-exponential factors  $\tau_0^{-1}$  with literature data. Values are according to Eq. 4.13. Enthalpies are derived from linear fits as shown in Fig. 4.20. DIL denotes dilatometric results, PAS positron annihilation spectroscopy and HM hardness measurement. For the PAS and HM results only one defect type was considered.

method	compound	$H_V^{M,1}$ [eV]	$H_V^{M,2}$ [eV]	$\tau_{0,1}^{-1} [\text{s}^{-1}]$	$\tau_{0,2}^{-1} [\text{s}^{-1}]$	Ref.
DIL	$\text{Fe}_{61}\text{Al}_{39}$	$1.2 \pm 0.1$	$0.7 \pm 0.1$	$2.7 \cdot 10^4$	2.2	this work
DIL	$\text{Fe}_{55}\text{Al}_{45}$	$1.5 \pm 0.2$	$0.6 \pm 0.1$	$4 \cdot 10^5$	0.8	[38]
PAS	$\text{Fe}_{61}\text{Al}_{39}$	$1.7 \pm 0.2$	—	$1.9 \cdot 10^8$	—	[43]
PAS	$\text{Fe}_{63}\text{Al}_{37}$	$1.7 \pm 0.2$	—	$1.9 \cdot 10^8$	—	[43]
HM	$\text{Fe}_{61}\text{Al}_{39}$	2.4	—	—	—	[59]

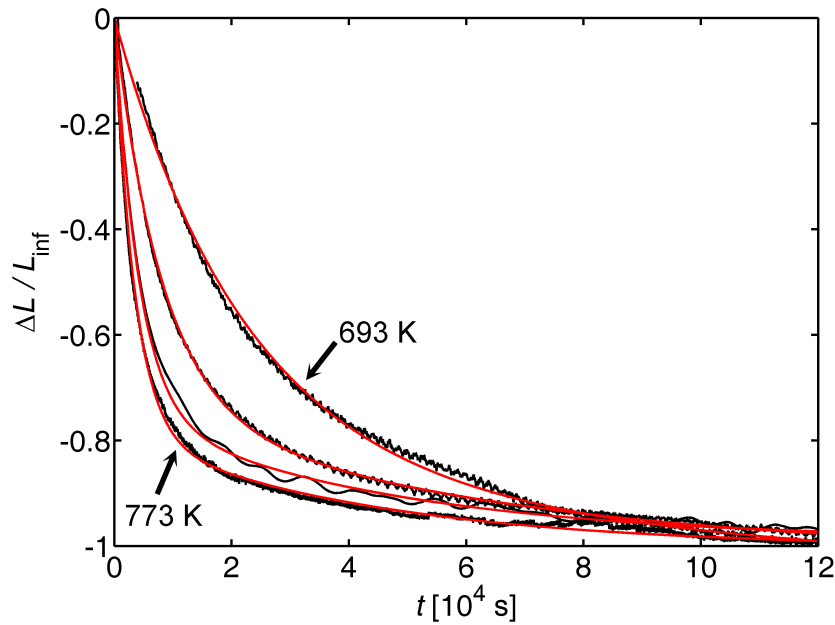


**Figure 4.21:** Volume equilibration curves for the Fe<sub>61</sub>Al<sub>39</sub> sample after fast cooling from different initial temperatures  $T_i$ . The equilibration temperatures  $T_f$  were: 773 K (represented by the steepest decrease), 753, 723 and 693 K (represented by the slowest decrease). All curves are normalized to their final amplitude  $L_{\text{inf}}$  at  $t = \infty$ . The amplitude was derived by fitting the data according to Eq. 4.13. In this representation the systematic decrease of the equilibration time constants is clearly visible.

the vacancy migration enthalpies were deduced. They are shown together with their pre-exponential factor  $\tau_{0,j}^{-1}$  in Tab. 4.2 in comparison with available literature data. The results are in principle in good agreement with the data measured by Frenner et al. for Fe<sub>55</sub>Al<sub>45</sub> [38]. However, a comparison with this different composition can only deliver information about the order of magnitude of the quantities. The one component models are only shown for completeness. The normalized volume equilibration curves used for vacancy migration measurements are shown in Fig. 4.21. In this representation the change in equilibration time with temperature is clearly visible. As seen from the coherence of the length change curves for different temperatures it is very likely that the same atomistic processes are the origin of contraction for all four curves. However, without an additional microscopic measurement technique it is not possible to clarify this point completely.

## Discussion

### Vacancy formation

Two volume related defects with formation enthalpies  $H_V^{F,1} = (1.2 \pm 0.1)$  eV and  $H_V^{F,2} = (1.4 \pm 0.1)$  eV could be measured. Especially the second process with a very high formation entropy of  $7.1 k_B$  can be attributed to a more collective atomic process like, e.g., a triple-defect formation in the B2 structure. Triple-defect in this case denotes the formation of two vacancies on the Fe sub-lattice combined with an anti-site atom on the Al lattice for structural stabilization. Theoretically the formation enthalpy for such a defect in FeAl was calculated by Bakker et al. [60] to be around 1.3 eV, which is in good agreement with the present results. A single vacancy formation process on the Fe sub lattice which should have a formation enthalpy of 0.65 eV [60] was not observed. Also the first process with a formation entropy of  $5.8 k_B$  and an enthalpy of 1.2 eV can hardly be attributed to single vacancy formation. As a conclusion it can be inferred that most likely the defect formation in B2-Fe<sub>61</sub>Al<sub>39</sub> is a more complex process than in metallic alloys.

An interesting fact is that the B2(l) to B2(h) transition proposed by Kubaschewski [57] and confirmed by Kerl et. al. [58], was clearly visible in the amplitudes of both measured processes but it seems that it has no influence on the kinetics or the defect type. This is confirmed by the migration enthalpies as shown in Fig. 4.20 where the data-points for an initial temperature of  $T_i = 993$  K fit very well to the data in terms of the time constants.

### Vacancy migration

The enthalpy values for defect migration  $H_V^{M,1} = (1.2 \pm 0.1)$  eV and  $H_V^{M,2} = (0.7 \pm 0.1)$  eV are up to now not completely explainable. The value of  $H_V^M = 1.2$  eV together with the  $H_V^F = 1.4$  eV value for the formation enthalpy results in an activation energy for self diffusion of about  $H_V^M + H_V^F = 2.6$  eV which is exactly the value found by Mehrer et. al. [56] for the activation energy for <sup>95</sup>Fe tracer diffusion in Fe<sub>66</sub>Al<sub>34</sub>. The second process with activation enthalpy 0.7 eV and a very small pre-exponential factor  $\tau_{0,2}^{-1}$  is more difficult to explain. Such a small value for the pre-exponential factor would suggest a very high migration entropy and therefore a complex process of atomic motion. Probably the motion is a collective jump process where more than one atom/vacancy is involved. Further measurements especially with systematic variations of the iron/aluminium content would be necessary to gather further information about the nature of this process.

The dilatometric measurements on B2-FeAl clearly demonstrated that high-resolution laser-dilatometry as developed in the course of this work is an indispensable tool for the investigation of open volume defects in structurally complex materials such as intermetallic compounds or metallic glasses. It was possible to directly measure defect migration and formation processes without using any additional parameters or conversions. Additionally the direct volume measurement also clearly showed that a single defect mechanism is not sufficient to describe the point defect kinetic in the investigated intermetallic compound.

The measurements in this section were also the first test of the new specimen holder design of the dilatometer as described in the dilatometer section. The concept proved to fulfil the desired criteria. No perturbations of the measurements, except for the external temperature variations caused by the laboratory environment were recognizable for all isothermal length change curves. Thermal perturbations produced cyclic 50 nm ripples in the signal which, however, did not influence the fitting quality.



---

## 5 Results and Discussion

---

In this chapter all measurements on metallic glasses together with their results which were conducted during this work are presented. Two zirconium based bulk metallic glasses,  $Zr_{56}Al_7Cu_{24}Ni_{10}Co_3$  and  $Zr_{52.5}Ti_5Cu_{17.9}Ni_{14.6}Al_{10}$  were analysed in terms of their sub  $T_g$  volume kinetics (Sec. 5.1) and the specific volume evolution upon approaching the glass transition temperature from the low temperature glassy state (Sec. 5.2). Additionally dynamic mechanical analysis (DMA) measurements on the  $Zr_{56}Al_7Cu_{24}Ni_{10}Co_3$  alloy are presented for comparison. To get deeper insights into the specific volume on a local atomic scale, positron annihilation measurements are presented in Sec. 5.3. Finally, the crystallization kinetics of  $Zr_{52.5}Ti_5Cu_{17.9}Ni_{14.6}Al_{10}$  is investigated with a self-developed measurement principle based on the simultaneous measurement of the thermal expansion coefficient and the isothermal length change of the material (Sec. 5.4).

### 5.1 Kinetics in the glassy state

#### 5.1.1 $Zr_{56}Al_7Cu_{24}Ni_{10}Co_3$ : Volume equilibration

The bulk glass forming alloy  $Zr_{56}Al_7Cu_{24}Ni_{10}Co_3$  is a direct derivation from the basic  $Zr(Cu,Ni)Al$  alloy system discovered by Inoue et al. in the early nineteen nineties [1, 61–64]. The glass forming ability of these alloys is based on the unconventionally slow crystal growth rate of  $Zr(Cu,Ni)$  intermetallic compounds [65, 66] in combination with a well-defined aluminium content. The aluminium plays an important role as

an oxygen-scavenger [67] and in controlling the viscosity of the undercooled liquid [68]. The combination of nickel and copper in many of these alloys is more or less based on empirical findings regarding the glass forming ability [69–72]. The same is true for cobalt, except for the fact that the influence on the material costs is much higher. Therefore, the need for cobalt is discussed in literature [73, 74]. In general the Zr(Cu,Ni)Al based bulk metallic glasses are besides those with beryllium addition the best glass forming metallic alloys without the need for noble metals like palladium or platinum.

In this subsection comprehensive sub  $T_g$  isothermal laser-dilatometric measurements for the alloy  $Zr_{56}Al_7Cu_{24}Ni_{10}Co_3$  are presented. A detailed analysis of the time-temperature variation of the equilibration time constants is performed to derive useful effective activation energies. At the end of this section these energies are compared, together with results for another glass alloy, to results obtained by other techniques especially to results obtained in tracer diffusion experiments. For completion the results of dynamic mechanical analysis measurements at higher temperatures (at and above  $T_g$ ) are presented.

## Sample material and preparation

The raw materials with a purity better than 99.9 wt% were first mixed and remelted two times in a vacuum arc furnace under high-purity argon atmosphere. After remelting they were cast in the form of prismatic ingots by the copper mould suction casting process. The ingots had a length of 40 mm, a height of 4 mm, and a width of 5 mm. To prepare the L-shaped sample geometry necessary for the dilatometric measurements they were first cut with a circular low-speed diamond saw and then carefully polished with a specially developed polishing device (see Sec. 3 for details). This device guarantees parallelism of the laser reflecting surfaces of better than  $\pm 2'$  (minutes of arc). For the temperature measurement three type-K thermocouples were spot-welded onto the surface as described in Chap. 4.

For the DMA measurements plates of  $20 \times 4 \times 0.5 \text{ mm}^3$  were cut from the ingot with a diamond saw. Details about the necessary geometry are given in the DMA part of this section.

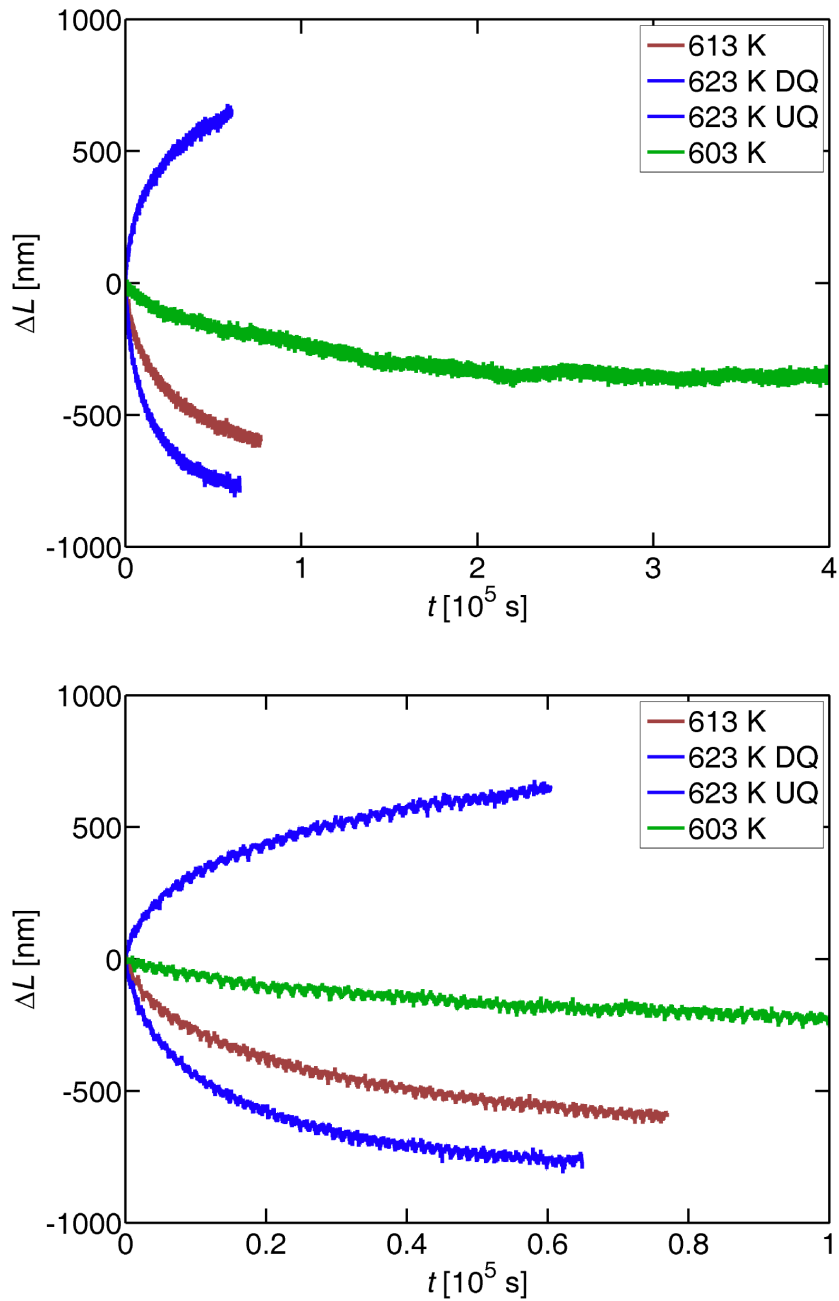


**Figure 5.1:** Example of laser-dilatometric measurement curves for the  $\text{Zr}_{56}\text{Al}_7\text{Cu}_{24}\text{Ni}_{10}\text{Co}_3$  glass after up- and down-quenching the equilibrated sample. The reversibility of the equilibration process is shown by the 623 K DQ (down quenching) and UQ (up quenching). In both cases the temperature step was  $\Delta T = 20$  K according to Tab. 5.1. In the  $4 \cdot 10^5$  seconds scaling of the abscissa in the upper panel the long-time equilibration curve at 603 K demonstrates the stability of the measurement system and the robustness of the environmental temperature influence correction method, as described in Sec 4.2, even at this small amplitude of about 350 nm. All curves were first fitted and analysed according to Eqs. 5.1 and 5.2.

**Table 5.1:** Measurement sequence with initial and final temperatures  $T_i$  and  $T_f$ , temperature steps  $\Delta T$  and time constants  $\tau(T_f)$  for the Zr<sub>56</sub>Al<sub>7</sub>Cu<sub>24</sub>Ni<sub>10</sub>Co<sub>3</sub> glass. The sign of the temperature step indicates whether the measurement was an up (+) or a down (-) quench according to the schematic in Fig. 4.14. All values are plotted in Fig. 5.2 together with their fitting function.

Measurement No.	$T_i$ [K]	$T_f$ [K]	$\Delta T$ [K]	$\tau(T_f)$ [10 <sup>3</sup> s]
1	583	643	+60	2.63
2	643	623	-20	18.60
3	623	633	+10	6.95
4	633	613	-20	33.50
5	613	648	+35	1.87
6	648	603	-45	84.40
7	603	623	+20	18.50
8	623	603	-20	—
9	603	613	+10	51.30

### Dilatometric measurements

Prior to the sub  $T_g$  measurements with the laser dilatometer the as-received ingots were sealed in evacuated glass ampoules and annealed for 44 days at 583 K, which is 81 K below  $T_g$  as determined from DSC measurements at 20 K/min [75]. This treatment assures that the expected large amount of quenched in free volume of the supercooled liquid state anneals out. Moreover, macroscopic and microscopic stresses, possibly present due to the high cooling rates in the copper mould casting process, are relieved.

The measurement procedure for the isothermal volume equilibration measurements is described in Sec. 4.3. Starting at the final pre-annealing temperature 583 K the volume equilibration measurements were conducted in the order as shown in Tab. 5.1. In Fig. 5.1 some example measurement curves are shown with two different abscissa scalings. The curves for 623 K DQ (down quench) and 623 K UQ (up quench) demonstrate the reversibility of the equilibration process. No irreversible volume reduction is observed in these measurements which confirms that the quasi equilibrium was reached due to the long-time pre-annealing procedure. To further analyse the equilibration behaviour,

an equilibration following a simple exponential behaviour in time was assumed. The isothermal curves were fitted with the following model

$$\Delta L(T_i, T_f, t) = A(T_i, T_f) \cdot \left( 1 - \exp \left( -\frac{t}{\tau(T_f)} \right) \right), \quad (5.1)$$

with  $A < 0$  for  $T_i > T_f$ , and  $A > 0$  for  $T_i < T_f$ . The time constants  $\tau$  are shown together with their final  $T_f$  values in Tab. 5.1. In Fig. 5.2 the inverse time constants are plotted versus the reciprocal temperature  $T_f$ . The up and down quenching measurements are indicated by up and down pointing triangles, respectively. In this Arrhenius-type plot a linear behaviour for the time constants covering two orders of magnitude is clearly visible. Therefore, an effective activation energy was deduced by assuming an exponential variation with temperature

$$\frac{1}{\tau(T_f)} = \frac{1}{\tau_0} \cdot \exp \left( -\frac{E_A}{k_B T} \right). \quad (5.2)$$

By fitting this function to the data points in Fig. 5.2 an effective activation energy  $E_A$  for volume migration together with a pre-exponential factor  $\tau_0^{-1}$  could be derived. Their values read as follows:

$$E_A = (2.9 \pm 0.1) \text{ eV}$$

$$\tau_0^{-1} = 1.42 \cdot 10^{(19 \pm 3)} \text{ s}^{-1}$$

The activation energy for migration is very high compared to the activation energies for vacancy diffusion mechanisms in crystalline alloys but comparable to values obtained for a bulk metallic glass in a comparable experiment [21]. The same is true for the very large pre-exponential factor. A detailed comparison of the measured values from this section with literature data and values from an alternative evaluation method is given in Sec. 5.1.4.

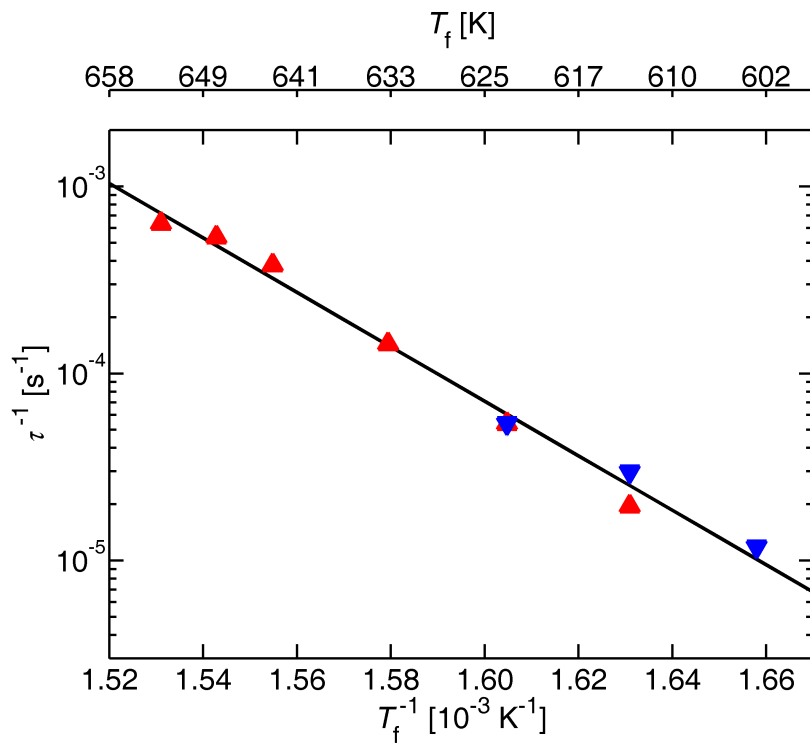


**Figure 5.2:** The time-temperature variation of the measured inverse time constants  $\tau(T_f)^{-1}$  from Tab. 5.1. The measurements performed after up-quenching are represented by the red up-pointing triangles, the down-pointing triangles represent the measurements after a down quench. The points at 623 and 613 K were measured both after up- and down-quenching. The reversibility of the volume equilibration process is clearly demonstrated by these data. No irreversible annealing-out of volume was detected in any of the measurements.

### X-ray diffraction

For all X-ray diffraction measurements a Bruker D8 Advance powder diffractometer equipped with  $\text{CuK}_\alpha$  radiation in Bragg-Brentano geometry was used. The total measurement time for all diffractograms was 24h with a step size of  $0.02^\circ$ . Diffraction patterns of the sample were measured in the as-received state, after the 44d / 583 K pre-annealing procedure and after the laser-dilatometric measurements. For comparison another sample of the material was crystallized in a vacuum furnace at 691 K for 3h. In Fig. 5.3 the diffractograms for the as received (blue) and long-time pre-annealed sample (red) are shown. No significant change in the diffractogram is visible, indicating that no structural changes occurred during the pre-annealing heat treatment. It should be noted that the sensitivity for distinct phases in this bulk sample is between one and three volume percent. In Fig. 5.4 the diffraction pattern for the sample after the dilatometric measurements is shown in red, together with the deliberately crys-

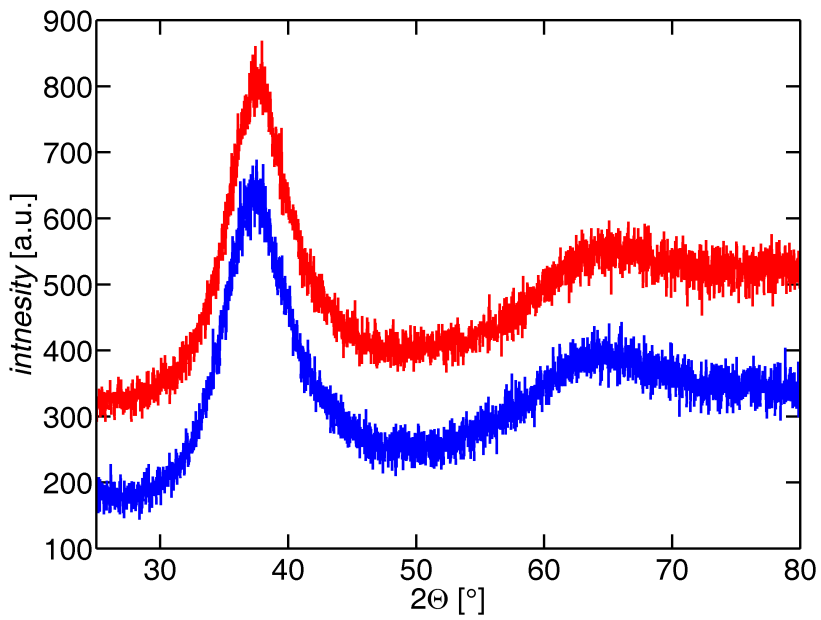


**Figure 5.3:** Diffraction patterns of the  $\text{Zr}_{56}\text{Al}_7\text{Cu}_{24}\text{Ni}_{10}\text{Co}_3$  dilatometer sample. The blue pattern represents the as-received state of the material. The red curve was measured after the 44d pre-annealing treatment at 583 K. No significant change in the X-ray diffraction behaviour is visible. The red pattern is offset for clarity.

tallized sample. The two sharp reflexes between 50 and 60° can hardly be attributed to crystallization from the supercooled liquid state because this process should first be visible around the intensity maximum. Furthermore, comparison with the partly crystalline sample (blue pattern in Fig. 5.4) shows that in this case no peaks at the relevant positions are visible. The most reasonable explanation for the observation is that the peaks are caused by crystals which were already in the alloy after manufacturing. These crystals were too small to be detected in the as-received state but grew during the higher temperature measurements in the dilatometer. This conclusion is confirmed by the results presented in the next paragraph.

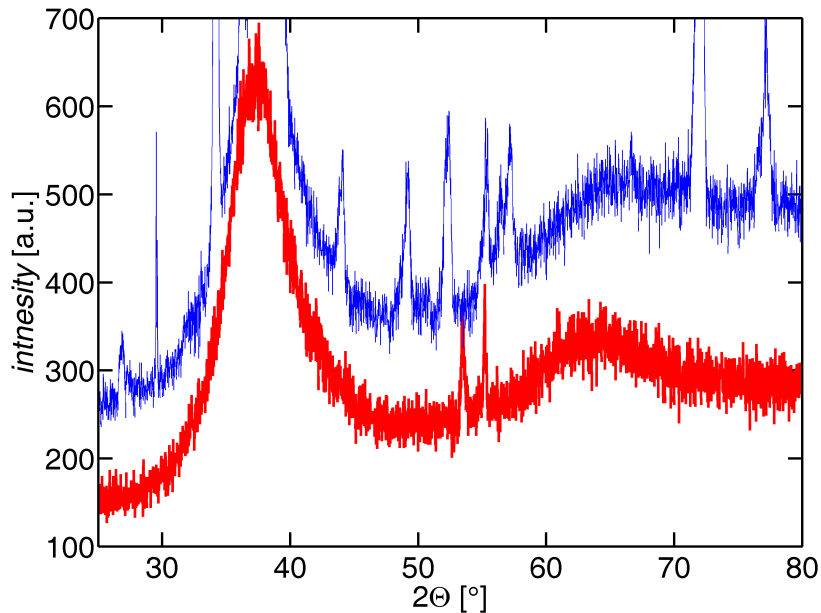


**Figure 5.4:** Diffraction pattern of the  $\text{Zr}_{56}\text{Al}_7\text{Cu}_{24}\text{Ni}_{10}\text{Co}_3$  sample after the dilatometric measurements (red) in comparison with a pattern from a partly crystalline sample (blue). The sharp reflexes between  $50$  and  $60^\circ$  in the pattern of the dilatometer sample do not show up in the artificially crystallized sample. These reflexes probably originate from crystals already formed during the casting process of the glass (see text for details).

## Optical microscopy

As a consequence of the non-assignable diffraction peaks in Fig. 5.4 the dilatometer sample was prepared for an inspection by an optical microscope. After it was cold embedded and grinded down to 1000 grid the polishing was conducted with diamond paste down to a particle size of  $2\mu\text{m}$ . For this Zr based alloy no etching solution for light microscopy is available in standard literature. Therefore, an etching solution, containing 20 ml H<sub>2</sub>O, 20 ml HCl (37%), 20 ml HNO<sub>3</sub> (65%) and 5 ml HF (40%) as, e.g, used for aluminium alloys was used. Empirically it turned out that a dilution 1:10 with distilled water delivers useful results. An Olympus BX41 microscope was used to study the specimen. In Fig. 5.5 pictures with different magnifications are shown. It is obvious that the amorphous glass matrix, which is characterized by a uniform darker brown appearance, contains a crystalline fraction at one area. The grain size of this crystals is in the  $100\ \mu\text{m}$  range and therefore not attributable to homogeneous crystallization of a deeply undercooled melt. The grain size of homogeneous crystallized Zr<sub>56</sub>Al<sub>7</sub>Cu<sub>24</sub>Ni<sub>10</sub>Co<sub>3</sub> at 691 K was measured to be in the 30 nm range [42]. In Fig. 5.5 a dendritic structure which is located in the centre of a crystallized region is visible. Most probably this was the nucleus for heterogeneous crystal growth into the amorphous matrix. As there was no homogeneous nucleation observed in the glass during dilatometric measurements, it is reasonable that large, low energy grains are formed instead of small ones with a large combined surface energy. The initial nuclei for the crystallization from the melt are not identifiable with light microscopic techniques. Possible explanations would be oxide impurities or a fast decomposition in the liquid state creating two phases with low glass forming ability. Nevertheless, the volume amount of crystals formed during the measurements was too low to significantly influence the volume equilibration of the glassy matrix. Furthermore, the observed reversibility of the equilibrium volume formation is a clear indication, that the crystals had no effect on the specific volume measurements.

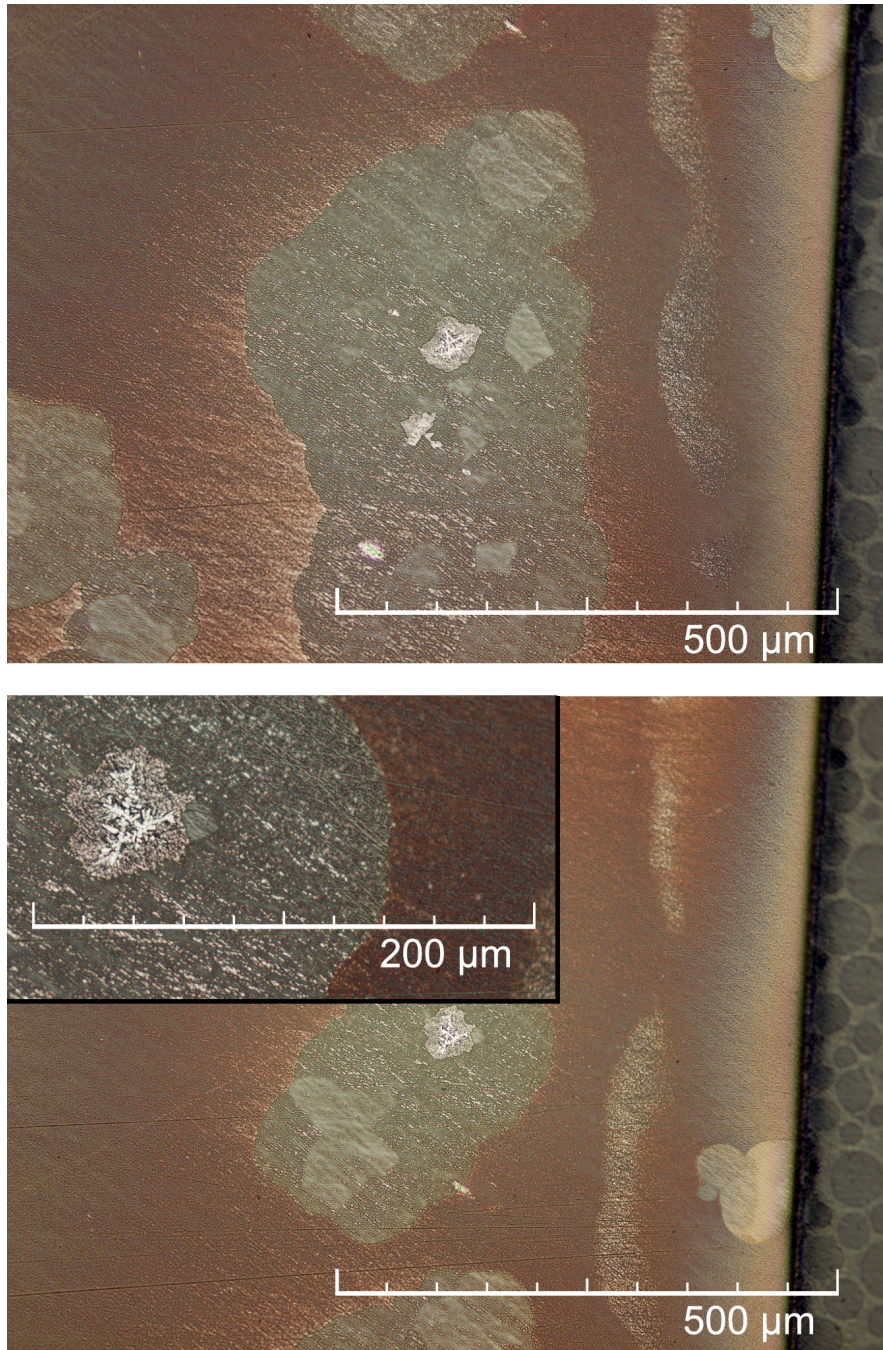


**Figure 5.5:** Light microscopic pictures of  $Zr_{56}Al_7Cu_{24}Ni_{10}Co_3$  after the laser-dilatometric measurements. In the amorphous matrix crystalline regions are visible. The glass matrix can be identified by the smoothly round shaped boundaries to the crystalline phases. In the crystalline regions a small dendritic structure can be found (shown in the inset in the lower panel), which is the possible heterogeneous seed for the crystallization process (see text).

**Table 5.2:** Time constants  $\tau^*$  and  $\tau_{\text{eff}}$  together with the stretching parameter  $\beta$  for different measurement temperatures  $T_i$  and  $T_f$  and temperature steps  $\Delta T$ . The measurement numbers correspond to the measurements in Tab. 5.1. The time temperature variation of the effective time constant  $\tau_{\text{eff}}$  is plotted in Fig. 5.8.

Measurement No.	$T_i$ [K]	$T_f$ [K]	$\Delta T$ [K]	$\beta$	$\tau^*(T_f)$ [10 <sup>3</sup> s]	$\tau_{\text{eff}}(T_f)$ [10 <sup>3</sup> s]
4	633	613	-20	0.65	31.10	47.80
2	643	623	-20	0.68	14.70	21.50
3	623	633	+10	0.88	7.04	8.02
1	583	643	+60	0.91	2.60	2.87
5	613	648	+35	0.92	1.92	2.09

### Stretched exponential analysis

The exponential analysis of the equilibration curves in Fig. 5.1 is based on the ideas first discussed in Ref. 21. In that paper a former version of the laser-dilatometer with lower measurement resolution was used. A closer look on the equilibration curves in Fig. 5.1 shows that especially at the lower measurement temperatures at shorter times the kinetics are not well described by a simple exponential function. In fact, the curves are too steep at the beginning, while they are not flat enough at very long measurement times. This behaviour is a typical feature of a stretched exponential equilibration as discussed in Sec. 2.3. Therefore, the analysis of the measurement results for the glass was repeated with a stretched exponential fitting function

$$\Delta L(T_i, T_f, t) = A(T_i, T_f) \cdot \left( 1 - \exp \left( - \left( \frac{t}{\tau^*(T_f)} \right)^\beta \right) \right). \quad (5.3)$$

The meanings of the variables are the same as in Eq. 5.1 except for  $\tau^*$  and the stretching parameter  $\beta$ . The basics developed in Chap. 2.3 were used to derive an effective time constant of equilibration

$$\tau_{\text{eff}} = \frac{1}{\beta} \cdot \tau^*. \quad (5.4)$$

In Fig. 5.6 two measured curves with different fitting functions are shown. At 613 K (upper panel) single exponential functions (black) are only able to describe either the

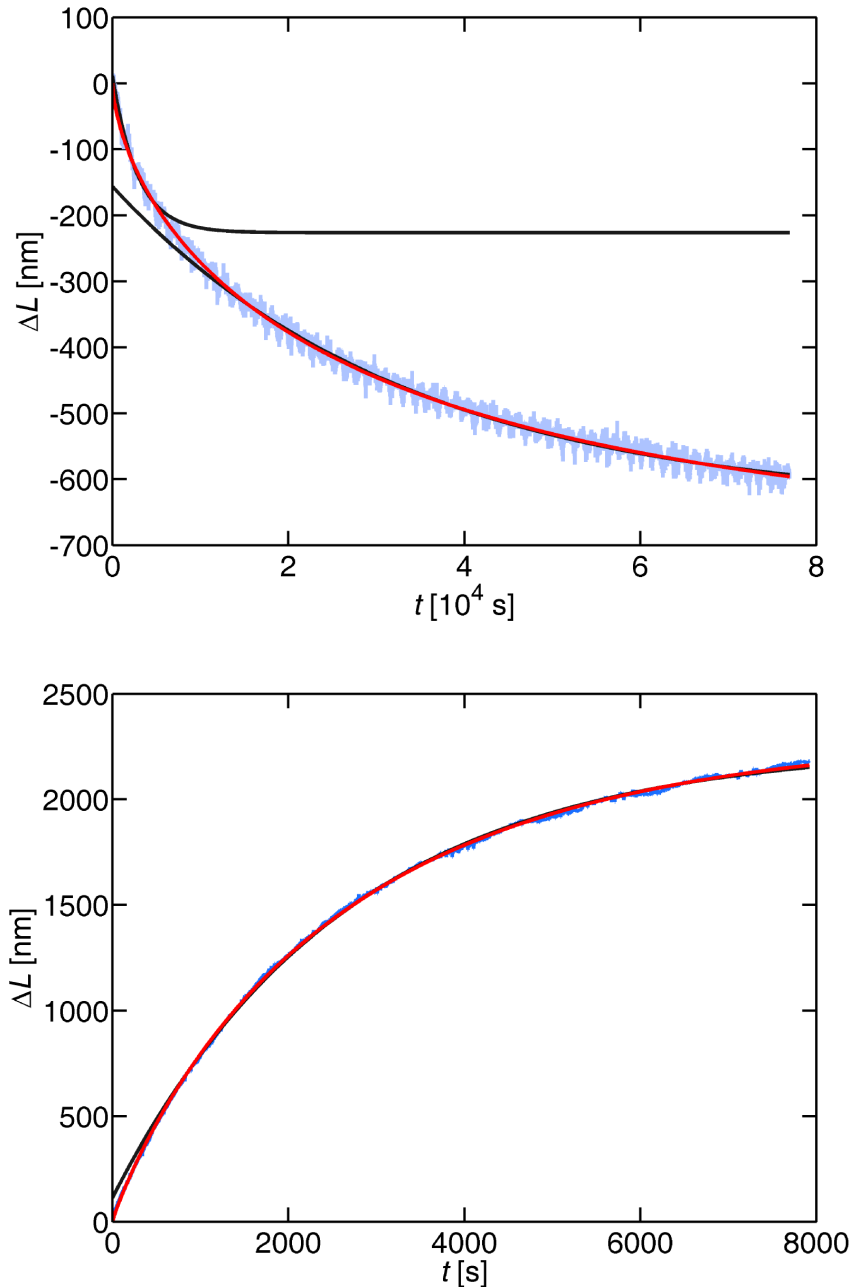


**Figure 5.6:** Comparison of exponential and stretched exponential fits to the length change curves  $\Delta L(t)$  for two different temperatures. At 613 K (60 K below  $T_g$ ) in the upper panel an exponential function (black) is either able to capture the short or the long time behaviour of the equilibration curve, while the stretched exponential function can describe both regimes. At the higher temperature of 643 K (30 K below  $T_g$ ) only minor deviations between the two models exist.

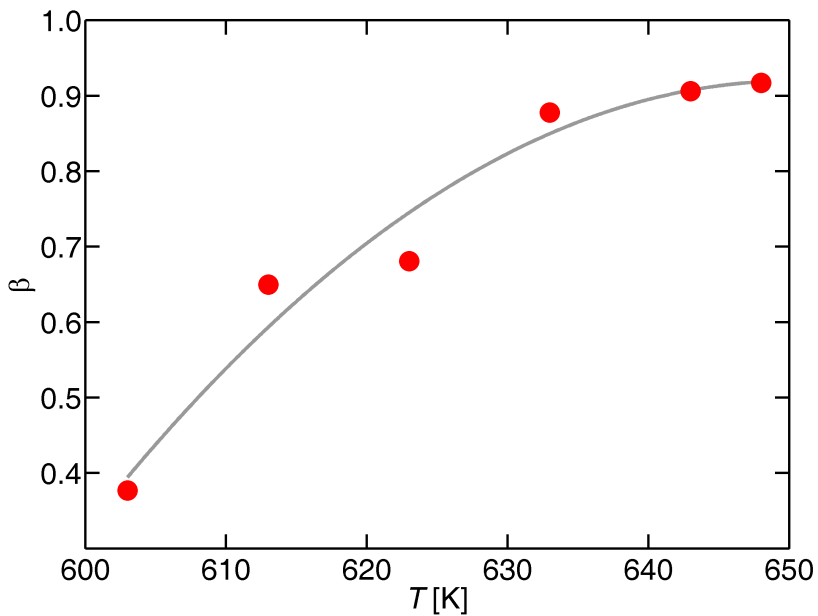


**Figure 5.7:** The temperature variation of the stretching parameter  $\beta$  for the  $Zr_{56}Al_7Cu_{24}Ni_{10}Co_3$  glass. The volume equilibration becomes more exponential ( $\beta \rightarrow 1$ ) as the glass reaches its glass transition temperature, which is in this case 673 K for a heating rate of 20 K/min. The estimated error from the fitting algorithm for each  $\beta$  value is smaller than 0.01. The grey line should serve as an indication for the tendency.

slow or the fast equilibration behaviour. The stretched exponential function, shown in red is able to describe both time regimes. In the lower panel a dilatometric curve measured at a higher temperature of 643 K is shown. In this case a single exponential function (black) deviates only slightly at very short times from the result of the stretched exponential function. This is a commonly observed behaviour in measurements on glasses. The equilibration becomes more and more exponential like upon approaching the glass transition from lower temperatures, see e.g. Refs. 6, 8, 9.

All measurement curves with an amplitude larger than 400 nm were fitted using the stretched exponential function. The lower amplitude curves were not taken into account because of too large uncertainties. An effective time constant was derived using Eq. 5.4. In Tab. 5.2 the results for the fitting-parameters are shown. The time constants were further analysed in terms of their temperature dependence. An Arrhenius plot is shown in Fig. 5.8. There, the linear temperature variation of  $\tau_{\text{eff}}$  is a clear sign for the presence of a distinct atomic volume equilibration process in the glassy state for this material. Therefore, the derivation of an activation energy for atomic motion is again possible according to Eq. 5.2, i.e., from the slope in Fig. 5.8. The obtained values for

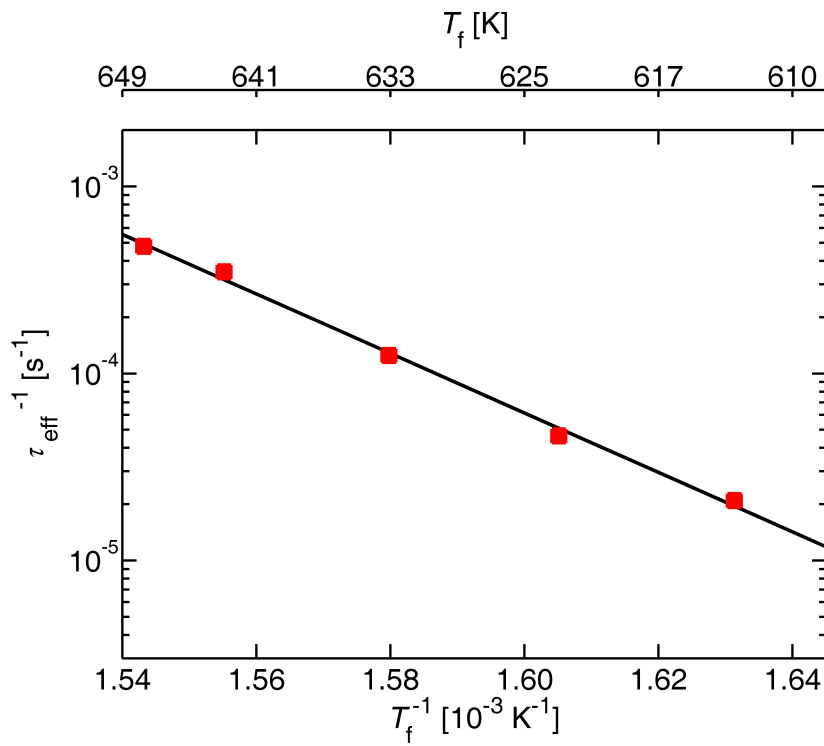


**Figure 5.8:** The temperature variation of the inverse effective time constants  $\tau_{\text{eff}}^{-1}$  (Tab. 5.2) derived using a stretched exponential analysis of the measurement curves. The observed linear behavior in the Arrhenius plot is an indication for the presence of the same dominant atomic process at all measurement temperatures.

the activation energy  $E_A$  and the pre-exponential factor  $\tau_0^{-1}$  are:

$$E_A = (3.2 \pm 0.1) \text{ eV}$$

$$\tau_0^{-1} = 1.76 \cdot 10^{(21 \pm 3)} \text{ s}^{-1}$$

These values are again fairly high compared to vacancy migration processes in crystalline materials. In Fig. 5.7 the temperature variation of the stretching parameter  $\beta$  is shown together with a tendency fit. For a detailed comparison with the results from the exponential analysis see Sec. 5.1.4.

As described in Sec. 2.3 the origin of the description of the equilibration with a stretched exponential function can be interpreted as the consequence of a continuous spectrum of defect sizes in the material. The different defect sizes have different time constants for the migration process. The probability distribution of time constants is then directly proportional to the probability of a certain defect size and can be calculated from the stretched exponential parameters according to Eq. 2.13. The time constant probability distributions for the presented measurements are shown in

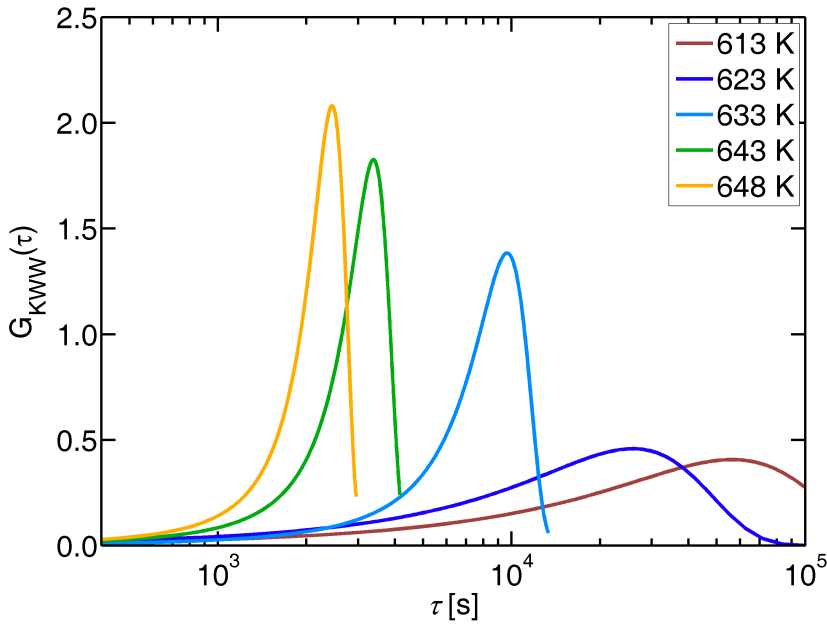


**Figure 5.9:** The probability distribution of the time constants as calculated from the stretched exponential parameters in Tab. 5.2. At higher measurement temperatures and for larger  $\beta$  values the distributions are becoming narrower. In the limit of  $\beta = 1$  they converge towards a Dirac- $\delta$  function with one defined time constant. This is equivalent to an exponential single process behavior. Some theoretical background of the functions can be found in Sec. 2.3.

Fig. 5.9. The distributions are becoming narrower with increasing temperature this is equivalent to a more and more exponential behaviour. In terms of defect sizes and/or defect mechanisms this means that one distinct process is becoming more and more dominant with increasing temperature.

### 5.1.2 Zr<sub>56</sub>Al<sub>7</sub>Cu<sub>24</sub>Ni<sub>10</sub>Co<sub>3</sub>: Dynamic mechanical analysis

In dynamic mechanical analysis (DMA) experiments the response of a material to an external mechanical perturbation is studied. In most measurements the stimulation of the sample is periodic in time, e.g., sinusoidal. Such a sinusoidal stimulation and response curve is shown in Fig. 5.10. For a real material the response to a mechanical perturbation cannot be instantaneous because of certain internal friction losses. A useful quantity to define such losses is the phase shift angle  $\delta$  (Fig. 5.10). The DMA measurements are a classical example of a linear response experiment (see Sec. 2.2 for details) the complex linear response function can be defined as

$$E^* = E' + iE'', \quad (5.5)$$

$E^*$  is called the complex modulus of the material and consists of the real part  $E'$  which is, depending on measurement geometry, the Young's-modulus or the shear modulus of the material. The imaginary part  $E''$  in Eq. 5.5 is the so called loss- modulus and represents the internal losses due to non-elastic effects. Geometrically these two quantities are linked by the simple relation

$$\frac{E''}{E'} = \frac{E \cdot \sin \delta}{E \cdot \cos \delta} = \tan \delta. \quad (5.6)$$

Another fundamental property of Eq. 5.5 is the connection between real and imaginary part by the Kramers - Kronig relation. Without going into detail it basically states that the real and imaginary parts of Eq. 5.5 are not independent and the whole function can be calculated by knowing just one of its parts [76].

In a real DMA measurement the quantity  $E^*$  is either measured as a function of temperature at a fixed stimulation frequency (temperature sweep) or as a function of frequency at a fixed temperature (frequency sweep). The relations mentioned above hold for both cases.

### Application to glasses

In glass science the DMA method is a well-established tool to investigate certain properties of the glass and the supercooled liquid. Especially bulk metallic glasses are the target of interest of many publications in the last years. A few examples for fundamental property studies can be found in Refs. 14, 77, 78. Based on the finding that glass forming supercooled liquids only relax in a liquid like manner at higher temperatures (with respect to their equilibrium melting temperature) many DMA measurements are focused on the splitting of relaxation into different regimes when the supercooled liquid approaches the glass transition. Beside the well-known  $\alpha$ -relaxation which is the fingerprint of liquid like behaviour, other relaxations usually termed  $\beta$  were found in many metallic glass forming systems [12, 13, 79, 80]. The nature and diversity of these secondary relaxations is a highly debated subject in glass science.

### DMA and the glass transition

When a glassy system approaches its glass transition temperature from lower temperatures its properties change continuously from a nearly ideal elastic material via a

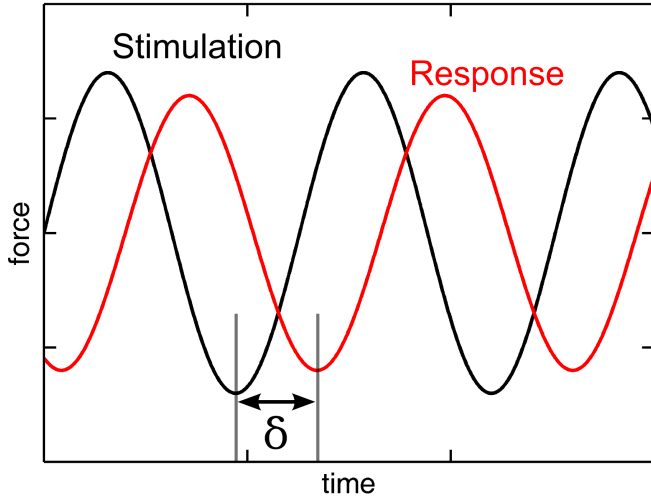


**Figure 5.10:** A typical sinusoidal DMA stimulation and response curve of a real material. In the ideal elastic case the stimulation and response curves are identical. In all other cases a distinct phase shift  $\delta$  occurs which is linked to the complex linear response function via Eq. 5.6. In glassy materials the phase shift strongly depends on the measurement temperature and/or the frequency, especially in the vicinity of the glass transition temperature.

viscoelastic regime towards a liquid like behavior at temperatures significantly higher than the calorimetric glass transition. In a fixed frequency DMA measurement the glass transition is characterized by a maximum in the loss modulus  $E''$ , i.e., the thermal particle fluctuation frequency in the liquid is in resonance with the stimulation frequency of the DMA (maximum loss). In other words the stimulation frequency  $\nu$  is directly connected to the structural relaxation time  $\tau_\alpha$  at a given peak temperature  $T_{max}$  by

$$\nu_{\text{stimulus}} = \tau_\alpha^{-1}(T_{max}). \quad (5.7)$$

This relation originates from the validity of the fluctuation-dissipation theorem which directly links microscopic equilibrium fluctuations to the macroscopic dissipation part of the response function. Some basics are given in Sec. 2.2. In Fig. 5.11 a typical behaviour of  $E'$  and  $E''$  in a temperature sweep is shown. The loss-peak shifts to higher or lower temperatures with stimulation frequency.

#### Temperature variation of the relaxation time $\tau_\alpha$

By changing the stimulation frequency the loss-peak as shown in Fig. 5.11 is shifted

to higher or lower temperatures. This variation can be analysed in terms of the temperature dependence of  $\tau_\alpha$ . Usually the behaviour is described by the empirical Vogel-Fulcher-Tamman (VFT) equation

$$\tau_\alpha(T) = \tau_0 \cdot \exp\left(\frac{B}{T - T_0}\right), \quad (5.8)$$

where  $T_0$  is the temperature at which the  $\alpha$ -relaxation time diverges, i.e., an ideal glass is formed, and  $B$  is a fitting parameter. The parameter  $B$  is usually linked to a quantity called fragility which is defined as

$$D^* = \frac{B}{T_0}. \quad (5.9)$$

The fragility  $D^*$  is a measure of the non-Arrhenius temperature dependence of  $\tau_\alpha$ . To link the results from low-temperature DMA measurements, which are usually conducted at temperatures around the glass transition, to high temperature melt viscosity measurements the simple Maxwell relation is used which is valid for viscoelastic materials

$$\tau_\alpha = \frac{\eta}{E_\infty}, \quad (5.10)$$

where  $\eta$  denotes the viscosity and  $E_\infty$  is the instantaneous elastic modulus of the material. It should be noted that the viscoelastic nature of a Maxwell material is only given at short times. On long time-scales the material exhibit flow, i.e., low stresses for long times lead to large irreversible strains. This is exactly the definition of liquid-like behaviour.

## Results

All measurements with the alloy Zr<sub>56</sub>Al<sub>7</sub>Cu<sub>24</sub>Ni<sub>10</sub>Co<sub>3</sub> were conducted in a single cantilever setup where a flat sample with a thickness of  $\approx 0.5$  mm is clamped on one side to a fixed sample holder and connected to a movable sample holder on the other side. This setup has the advantage that measurements are possible up to very low viscosities. Unfortunately, the available DMA was only equipped with a temperature sweep program. As a consequence for every frequency, i.e., every relaxation time measurement, a new sample was necessary because of the relatively fast crystallisation of the metallic glass at temperatures 40 K above the calorimetric glass transition. For this reason the

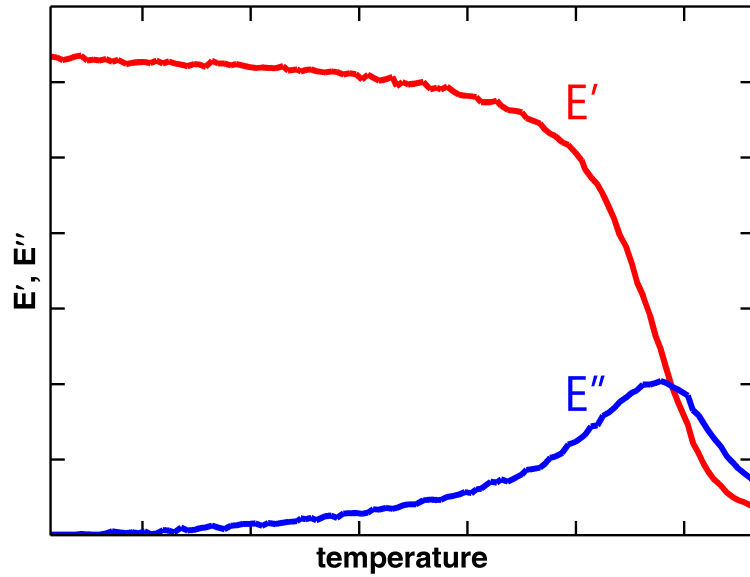


**Figure 5.11:** The typical behaviour of the elastic moduli  $E'$  and  $E''$  at the glass transition here as an example measured for  $Zr_{56}Al_7Cu_{24}Ni_{10}Co_3$  at a frequency of  $0.4\text{ s}^{-1}$  and a heating rate of  $3\text{ K/min}$ . The temperature at which the loss modulus has its maximum for a give stimulation frequency defines the  $\alpha$ -relaxation time at this temperature according to Eq. 5.7.

measurements were limited to five different frequencies only:  $0.02, 0.10, 0.40, 0.8$  and  $1\text{ s}^{-1}$ . In Fig. 5.12 the normalized real part of the complex modulus for the measurements is shown. As expected the elastic behaviour is shifted to higher temperatures for higher stimulation frequencies. All measurement curves are shown until the onset of crystallisation. In Fig. 5.13 the loss peaks corresponding to Fig. 5.12 are plotted. The stagnation of the shift to higher temperatures for the  $1\text{ s}^{-1}$  peak is attributed to possible structural variations between the different samples. At higher temperatures the loss peak for this material was not resolvable anymore because of interfering crystallisation.

#### Evaluation of the results assuming an Arrhenius behaviour

As a first step the variation of the loss-peak maximum temperature with frequency was analyzed in terms of a simple Arrhenius behavior:

$$\tau_\alpha(T) = \tau_0 \cdot \exp\left(\frac{E_A}{k_B T}\right) \quad (5.11)$$

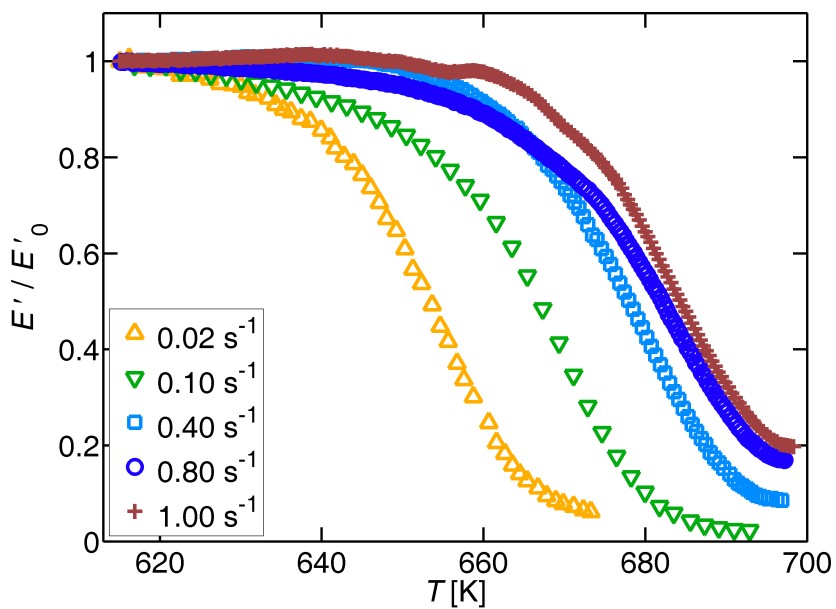


**Figure 5.12:** The normalized real part of the complex modulus for the  $\text{Zr}_{56}\text{Al}_7\text{Cu}_{24}\text{Ni}_{10}\text{Co}_3$  glass for different frequencies  $\nu$ . The elastic behaviour is shifted to higher temperatures with stimulation frequency. Some deviations are visible in the data for  $\nu = 1 \text{ s}^{-1}$  possibly caused by crystalline "drag" in the material. All curves are plotted until the onset of crystallization. The used heating rate was 3 K/min for all measurements except for the  $0.02 \text{ s}^{-1}$  measurement where it was 0.5 K/min.

With  $E_A$  as distinct activation energy,  $k_B$  Boltzmann's constant and  $\tau_0$  a pre-exponential factor. Such a behavior is expected for very "strong" glass formers such as  $\text{SiO}_2$ . In Fig. 5.14 the results are shown. From the slope and ordinate intersect the following values could be derived:

$$E_A = (5.2 \pm 0.2) \text{ eV}$$

$$\tau_0 = 2.49 \cdot 10^{(-39 \pm 5)} \text{ s}$$

Those values are very high but in good agreement with literature data from Ref. 81 also obtained from internal friction measurements. In this measurement the alloy  $\text{Zr}_{55}\text{Al}_{10}\text{Ni}_5\text{Cu}_{30}$  was investigated. The values obtained were  $E_A = (5.9 \pm 0.2)$  eV and  $\tau_0 = 2.49 \cdot 10^{43}$  s. At least the high activation energy values are reasonable because relaxation in liquids is a highly collective process where the movement of constitutional units is highly correlated. The very large pre-exponential factor is mainly caused by the uncontrolled extrapolation to infinitely high temperatures. This extrapolation would only be correct if the liquid would show Arrhenius behavior over the whole temperature range, which is highly unlikely for a bulk metallic glass.

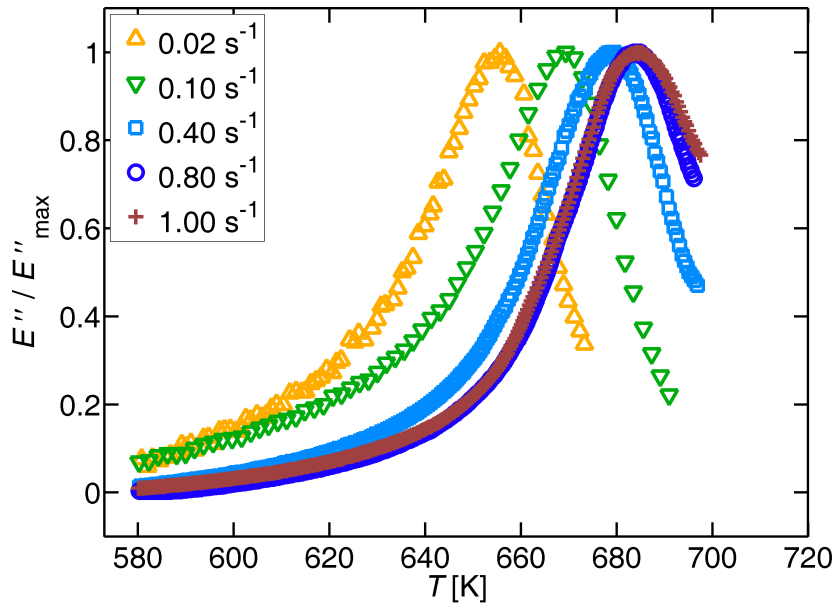


**Figure 5.13:** The normalized imaginary part of the complex modulus for the  $\text{Zr}_{56}\text{Al}_7\text{Cu}_{24}\text{Ni}_{10}\text{Co}_3$  glass. The resonance peaks for the  $\alpha$ -relaxation are shifted to higher temperatures with increasing stimulation frequency. The stagnation of shifting for the  $1 \text{ s}^{-1}$  data points to a higher temperature are possibly caused by the same deviations which are visible in the real part of  $E^*$  in Fig. 5.12.

### Evaluation of the results assuming a VFT behaviour

In next step the relaxation times were analysed with the Vogel-Fulcher-Tamman (VFT, Eq. 5.8). Because of the very limited time range the fitting procedure showed large uncertainties. Nevertheless it is interesting to see how the  $\text{Zr}_{56}\text{Al}_7\text{Cu}_{24}\text{Ni}_{10}\text{Co}_3$  alloy fits into the so-called Angell plot [82]. The values derived by fitting the data are:

$$\begin{aligned}T_0 &= (370 \pm 30) \text{ K} \\B &= (1.07 \pm 0.03) \cdot 10^4 \text{ K} \\D^* &= (29 \pm 2)\end{aligned}$$

The fragility parameter  $D^*$  fits very well into the range of literature values for bulk metallic glasses [17, 83–87]. In Fig. 5.15 the Angell plot for the alloy is shown together with literature data for different bulk glass forming systems as well as  $\text{SiO}_2$ . The literature data where viscosity was measured was converted to relaxation times using Eq. 5.10 together with the values for the elastic moduli from Refs. 88–90. It should be noted that the abscissa in Fig. 5.15 is normalized to the glass transition temperature

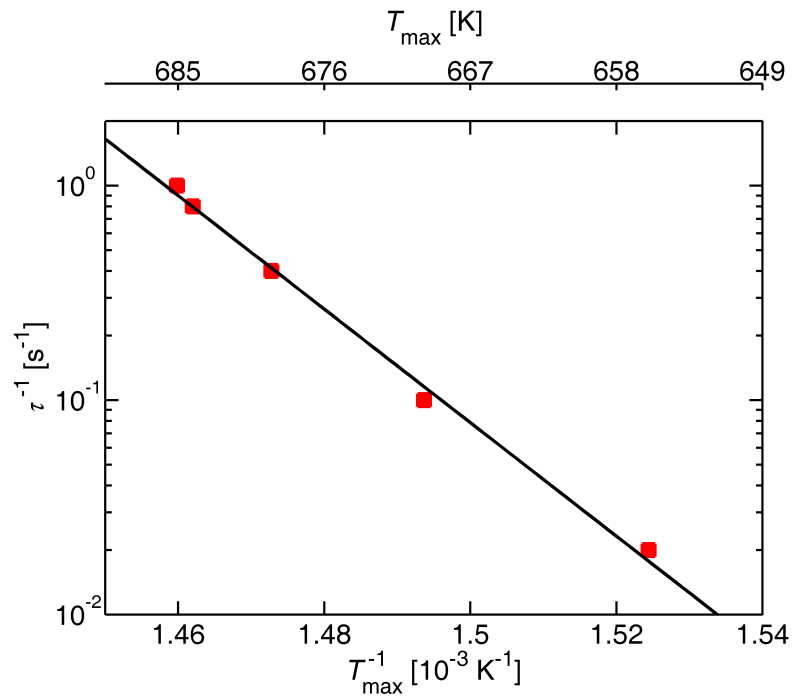


**Figure 5.14:** The temperature variation of the inverse mechanical relaxation time  $\tau_\alpha$  from DMA measurements. In the investigated temperature regime the variation is Arrhenius conform with a very high activation energy of  $E_A = (5.2 \pm 0.2)$  eV.

of the respective material. This procedure is certainly a source for large errors because of the strong heating rate dependence of the glass transition. For the alloy of this work the onset of glass transition from Ref. 75,  $T_g = 643$  K was used.

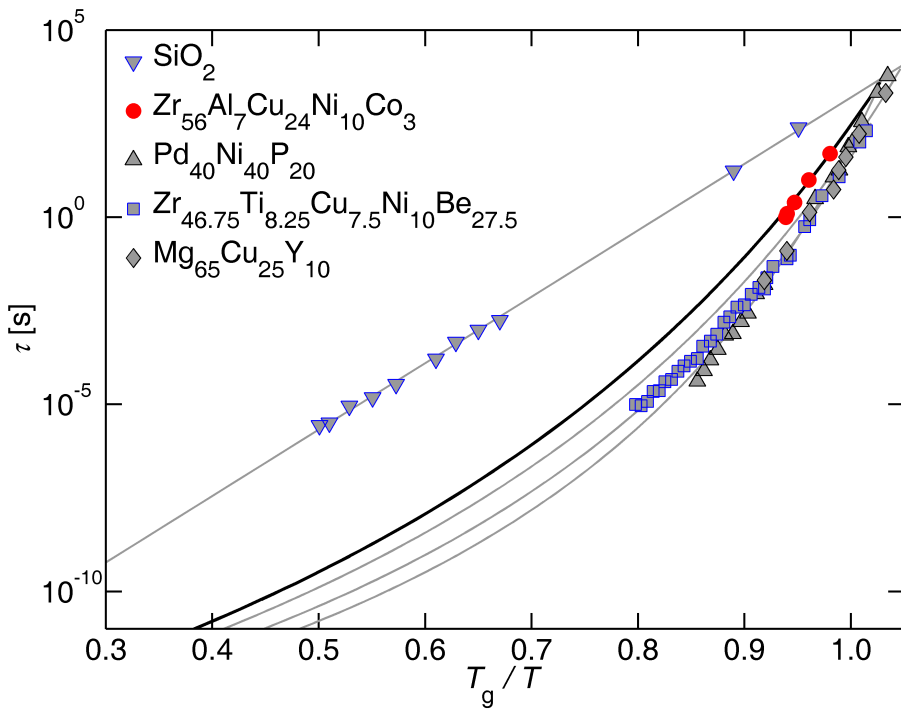


**Figure 5.15:** The Angell-plot for the  $\text{Zr}_{56}\text{Al}_7\text{Cu}_{24}\text{Ni}_{10}\text{Co}_3$  alloy (red filled circles), together with literature data for bulk metallic glasses and  $\text{SiO}_2$ . The presented glass shows an intermediate fragility of  $D^* = (29 \pm 2)$  which is well in the range of other bulk glass forming alloys. The value of  $T_g$  for  $\text{Zr}_{56}\text{Al}_7\text{Cu}_{24}\text{Ni}_{10}\text{Co}_3$  was taken from Ref. 75. All fits were derived using Eq. 5.8 and 5.11 ( $\text{SiO}_2$ ). Literature data for viscosity and/or relaxation time was taken from Refs. 17, 83–87 values for elastic moduli are from Refs. 88–90.

### 5.1.3 $\text{Zr}_{52.5}\text{Ti}_5\text{Cu}_{17.9}\text{Ni}_{14.6}\text{Al}_{10}$ : Volume equilibration

Like the glass discussed in the previous section the alloy  $\text{Zr}_{52.5}\text{Ti}_5\text{Cu}_{17.9}\text{Ni}_{14.6}\text{Al}_{10}$  (Vit105) is a member of the  $\text{Zr}(\text{Cu},\text{Ni})\text{Al}$  family of bulk metallic glasses. In contrast the aforementioned alloy Vit105 was developed in the group of William Johnson at Caltech in the early nineteen nineties [2, 91]. The alloy Vit105 was one of the first bulk metallic glass forming alloys without the need for beryllium, and therefore producible with less precautions in a physiological sense.

In this section reversible sub  $T_g$  volume measurements are presented and analyzed by means of the stretched exponential analysis described in Sec. 2.3. The deduced measurement results are compared to the previously measured alloy and a comparison with results from other measurement techniques is given. Especially the available data on tracer diffusion in bulk metallic glasses is reviewed to get possible insights into atomistic origins of the reversible volume migration process.

#### Sample material and preparation

The production process for the  $\text{Zr}_{52.5}\text{Ti}_5\text{Cu}_{17.9}\text{Ni}_{14.6}\text{Al}_{10}$  ingots is described in Sec. 3.1. The preparation of the L-shaped sample geometry, the polishing process and the thermocouple attachment was conducted in the same way as for the  $\text{Zr}_{56}\text{Al}_7\text{Cu}_{24}\text{Ni}_{10}\text{Co}_3$  alloy, explained in Sec. 5.1.1 and Sec. 3.1.

#### Dilatometric measurements

Prior to the dilatometric measurements the samples were sealed in evacuated glass ampoules and pre-annealed for 27 days at 573 K which is 80 K below the onset of glass transition at a heating rate of 5 K/min. From the time constant temperature variation for the  $\text{Zr}_{56}\text{Al}_7\text{Cu}_{24}\text{Ni}_{10}\text{Co}_3$  alloy one month of annealing was expected to be sufficient for complete structural equilibration at this temperature.

The isothermal measurement procedure was again the same as described in Sec. 4.3. The temperature steps, measurement order and time constants are shown in Tab. 5.3. In Fig. 5.16 measurement curves with two different abscissa scalings are presented. The reversibility is shown by the two curves for 613 K (red) which are denoted with "UQ" for up-quench and "DQ" for down-quench. In comparison with the measurements in the last section the measurement stability and temperature gradient over the sample length

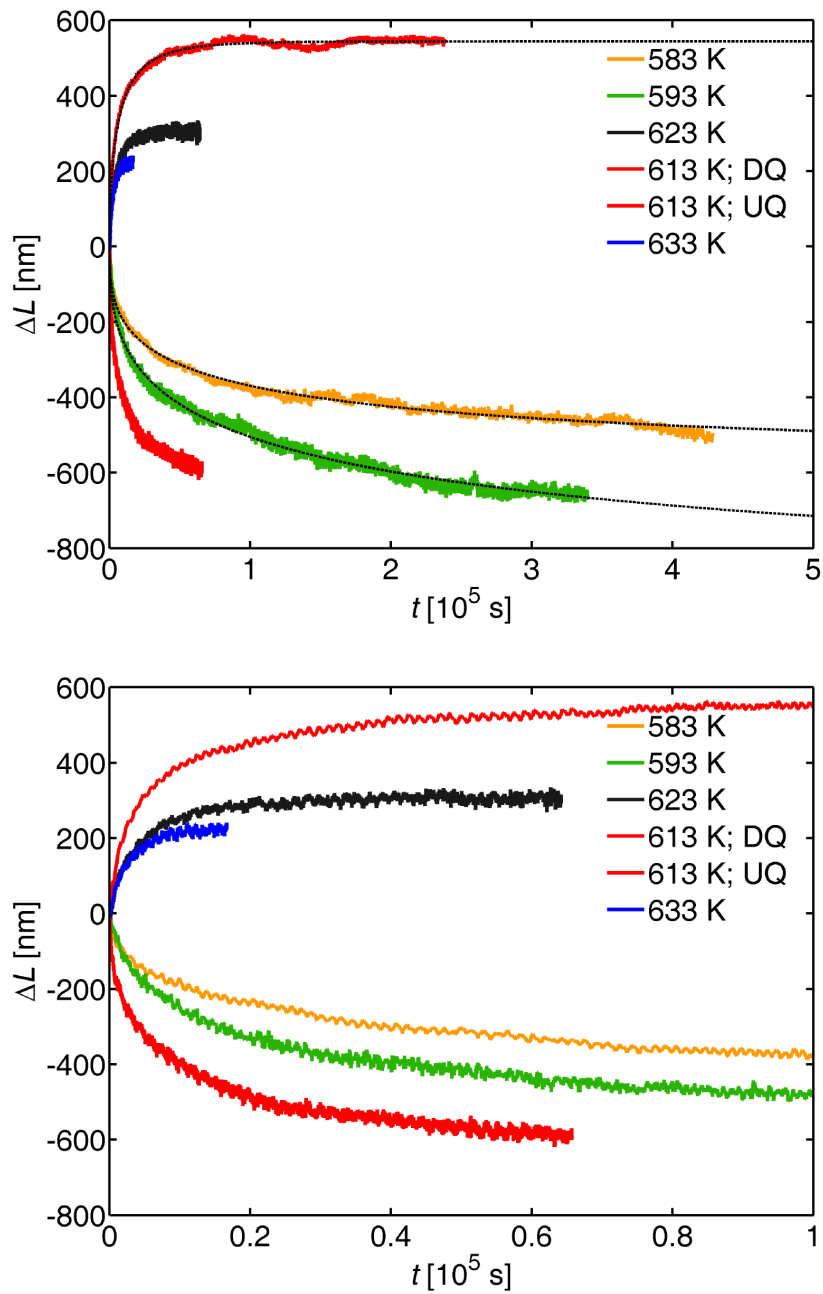


**Figure 5.16:** Examples for isothermal measurement curves for the Zr<sub>52.5</sub>Ti<sub>5</sub>Cu<sub>17.9</sub>Ni<sub>14.6</sub>Al<sub>10</sub> bulk glass. The further improved measurement stability and temperature gradient minimization in comparison to the Zr<sub>56</sub>Al<sub>7</sub>Cu<sub>24</sub>Ni<sub>10</sub>Co<sub>3</sub> glass reveals a very steep increase or decrease in volume at shorter times while at longer times especially in the upper panel very slow volume equilibration is detected. In the lower panel, which is limited to a time range of 10<sup>5</sup> s the reversibility is again demonstrated for the two 613 K curves where "DQ" means down-quenching and "UQ" means up-quenching. Because of the appearance of the curves a single process exponential equilibration was not taken into account. In the upper panel the long-time curves are shown together with their KWW fits. All stretched exponential fits are shown together with the data in Fig. 5.17. ( $\Delta L > 0$  up-quench;  $\Delta L < 0$  down-quench)

**Table 5.3:** Time constants  $\tau^*$  and  $\tau_{\text{eff}}$  together with the stretching parameter  $\beta$  for different initial temperatures  $T_i$  and final temperatures  $T_f$ . The sign of the temperature step  $\Delta T$  indicates if the measurement was an up- or a down-quench.

Measurement No.	$T_i$ [K]	$T_f$ [K]	$\Delta T$ [K]	$\beta$	$\tau^*(T_f)$ [10 <sup>3</sup> s]	$\tau_{\text{eff}}(T_f)$ [10 <sup>3</sup> s]
1	573	613	+40	0.51	6.03	11.70
2	613	633	+20	0.80	2.79	3.48
3	633	593	-40	0.35	42.30	121.00
4	593	623	+30	0.67	4.10	6.13
5	623	643	+20	0.86	3.43	3.98
6	643	613	-30	0.55	10.30	18.80
7	613	583	-30	0.24	116.00	476.00
8	583	653	+70	0.91	6.17	6.81

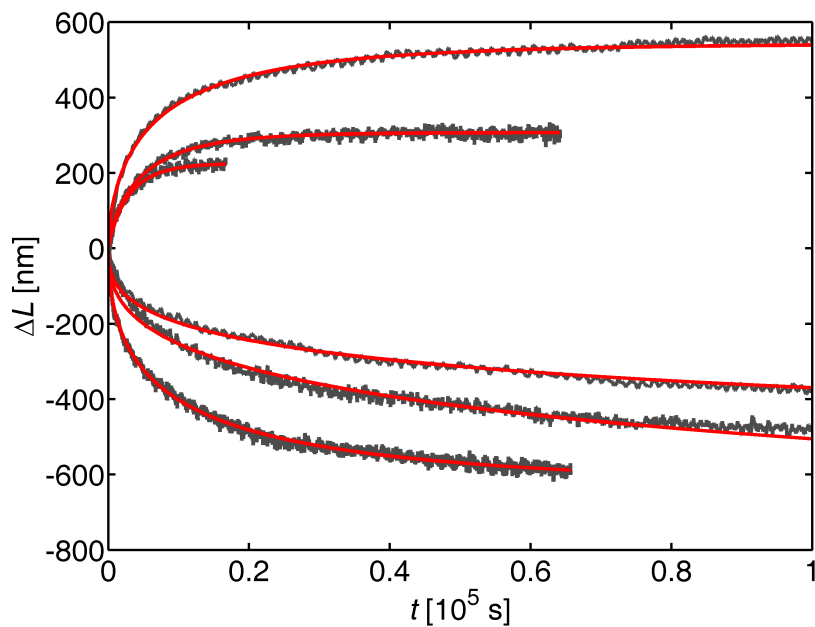


**Figure 5.17:** The isothermal volume equilibration curves from Fig. 5.16 together with their KWW fits. The agreement with the measured data is excellent, especially the slower and faster processes are captured by the stretched exponential analysis. The values for the stretching parameter  $\beta$  and the time constants of the fits are given in Tab. 5.3.

was further improved. For all measurements the temperature difference  $\Delta T$  between the thermocouples was below 2 K which is in the range of the temperature measurement uncertainty of the type-K spot-welded wires used. With this improvements the already noticed appearance of fast and very slow processes at a fixed temperature is even better resolved than for the measurements presented in Sec. 5.1.1. For this reason a simple exponential analysis was discarded from the beginning. All measurements were fitted with the previously described function (see section 5.1.1)

$$\Delta L(T_i, T_f, t) = A(T_i, T_f) \cdot \left( 1 - \exp \left( - \left( \frac{t}{\tau^*(T_f)} \right)^\beta \right) \right). \quad (5.12)$$

Effective time constants were calculated according to

$$\tau_{\text{eff}} = \frac{1}{\beta} \cdot \tau^*. \quad (5.13)$$

In Fig. 5.16 in the upper panel the fits for the long-time curves are shown. It should be noted that even for this very long equilibration processes the agreement with the fitting function is excellent. Therefore, it can be inferred that all the kinetic information is included in the stretched exponential fit. In Fig. 5.17 all fits to the measurements are shown with a different abscissa scaling to better estimate the short time fitting quality. At very short times compared to the time constant  $\tau_{\text{eff}}$  minor deviations from the measurements are visible for the 583 and 593 K fits. However, the coefficient of determination  $R^2$  is better than 0.98 for all functions. In Fig. 5.18 the variation of the stretching parameter  $\beta$  with temperature shows a smooth increase towards unity which is again attributable to the very high temperature stability and specimen quality. It is noteworthy to say that the increase in  $\beta$  which is also found in enthalpy relaxation experiments is not a trivial feature of the glass. An atomistic interpretation like proposed in Sec. 2.3 is only one out of a few possibilities. For more details the reader is referred to the discussion section. The Arrhenius plot for the  $\tau_{\text{eff}}$  values from Tab. 5.3 are shown in Fig. 5.19. The values derived in up-quenching experiments are marked with up-pointing red triangles and the values from down-quenching experiments are symbolized by blue down-pointing triangles. From the slope and ordinate intersect the following values could be derived:

$$E_A = (3.1 \pm 0.1) \text{ eV}$$

$$\tau_0^{-1} = 2.35 \cdot 10^{(21 \pm 3)} \text{ s}^{-1}$$

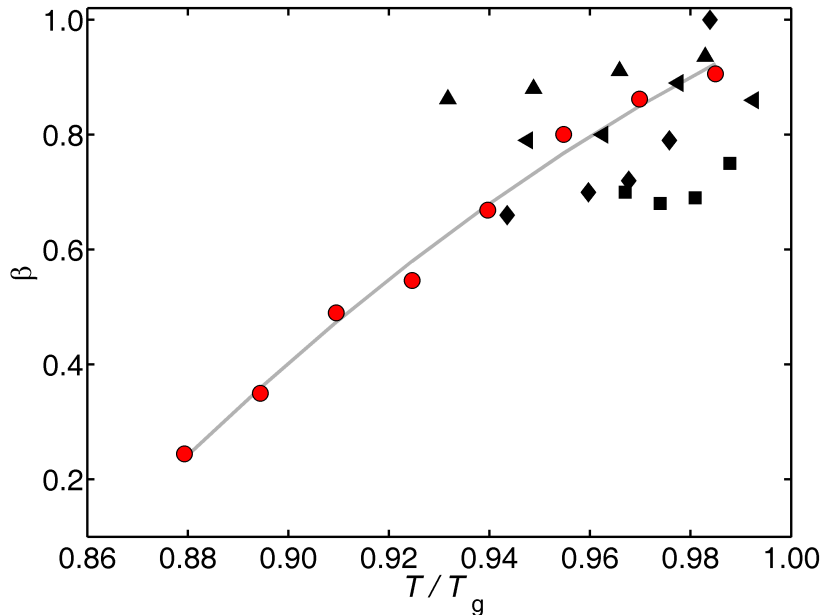


**Figure 5.18:** The temperature variation of the stretching exponent  $\beta$  (red filled circles) obtained for  $\text{Zr}_{52.5}\text{Ti}_5\text{Cu}_{17.9}\text{Ni}_{14.6}\text{Al}_{10}$  in the present work. The value increases towards unity upon reaching the glass transition temperature, which in this case is at 663 K for a heating rate of 5 K/min. In Tab. 5.3 the  $\beta$  values are listed together with the time constants. For comparison  $\beta$  values from literature are also shown. The left pointing triangles ( $\blacktriangleleft$ ) and diamond shaped data points ( $\blacklozenge$ ) are from DSC and conventional dilatometric measurements for Zr based glasses from Refs. 6 and 9. The up-pointing triangles ( $\blacktriangleright$ ) are from DSC measurements on a Ti-based glass [7] and the squares ( $\blacksquare$ ) represent DSC data for a Pd-based glass from Ref. 92. In all measurements an irreversible annealing-out of quenched-in volume from the supercooled liquid state was studied below  $T_g$ . Therefore, the kinetics are not necessarily comparable with the presented fully reversible sub- $T_g$  results.

The values are discussed at the end of this section. Also a comparison with tracer diffusion experiments is presented. The time constants probability distributions, calculated from the values in Tab. 5.3 are plotted in Fig. 5.20 the ordinate is given by

$$G_{\text{KWW}}(\tau) = \rho(\tau) \cdot \tau, \quad (5.14)$$

which is the link to the density function  $\rho(\tau)$  in Eq. 2.13. In comparison with the results for the  $\text{Zr}_{56}\text{Al}_7\text{Cu}_{24}\text{Ni}_{10}\text{Co}_3$  alloy in Fig. 5.9 the variation of the maxima with measurement temperature is more steady with less abrupt jumps.

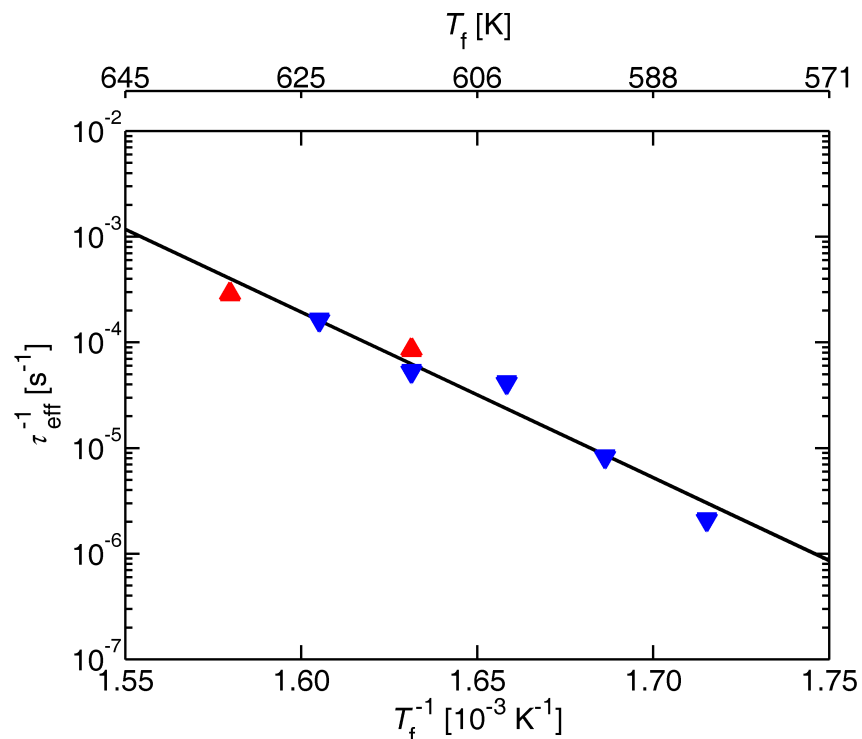


**Figure 5.19:** Arrhenius plot of the effective time constants for volume equilibration for Zr<sub>52.5</sub>Ti<sub>5</sub>Cu<sub>17.9</sub>Ni<sub>14.6</sub>Al<sub>10</sub> as taken from Tab. 5.3. The blue triangles are data values derived from down-quenching curves and the red triangles indicate up-quenches. The corresponding values for  $\tau_{\text{eff}}$  shown in this plot can be found in Tab. 5.3. From the slope of the linear fitting function an effective activation energy of  $E_A = (3.1 \pm 0.1) \text{ eV}$  was derived. The pre-exponential factor from the ordinate intersect is:  $\tau_0^{-1} = 2.35 \cdot 10^{(21 \pm 3)} \text{ s}^{-1}$ .

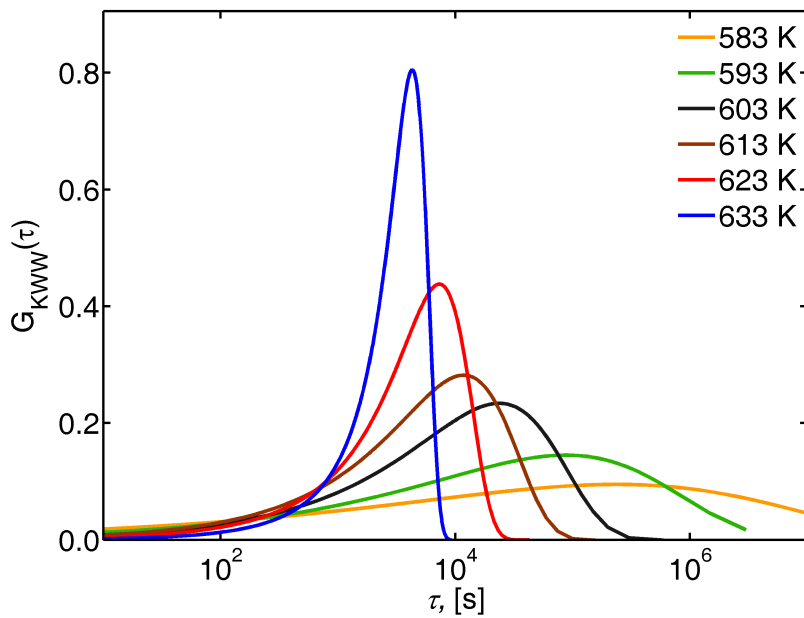


**Figure 5.20:** The probability distribution of the time constants calculated from the stretched exponential parameters in Tab. 5.3. A very smooth broadening of the distributions towards lower temperatures is observed. Although the maxima shift to longer times with decreasing temperature, a long tail to shorter times remain which is responsible for the very steep initial increase or decrease in volume even at the lowest measurement temperatures.

### X-ray diffraction

X-ray diffraction patterns were measured in the as-received state, after the 27d pre-annealing and after the dilatometric measurements. The measurement time was  $\approx 24\text{h}$  with a step size of  $0.02^\circ$ . In Fig. 5.21 the patterns are shown. After the dilatometric measurements a sharpening of the second diffuse peak in the diffractogram is visible. A possible reason is an increasing short range order in the material. The last dilatometric measurement was made at 653 K and measurement time was  $> 10^4 \text{ s}$ . From available TTT diagrams an onset of crystallization could be expected for this combination [93]. Also the time constant in Tab. 5.3 for 653 K does not fit the other measurements, which is an indication for the existence of additional volume affecting processes at this temperature.

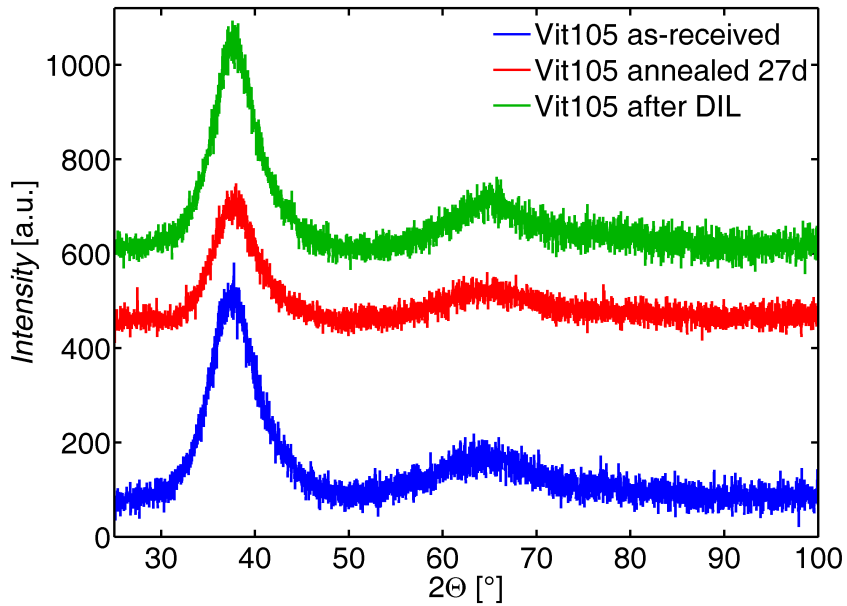


**Figure 5.21:** X-ray diffraction patterns for the Vit105 alloy in the as-received, long time annealed and measured state. After the dilatometric measurements a sharpening of the second diffuse diffraction maximum is visible. This is probably attributed to an increasing short range order of the glass. Especially in the last measurements the sample was kept in the vicinity of the calorimetric glass transition for times exceeding  $10^4$  s. From available TTT diagrams this time was estimated to be the onset time for crystallization [93].

### 5.1.4 Discussion

#### $\text{Zr}_{56}\text{Al}_7\text{Cu}_{24}\text{Ni}_{10}\text{Co}_3$ - Activation energies

In Sec. 5.1.1 the sub- $T_g$  dilatometric measurements for the alloy  $\text{Zr}_{56}\text{Al}_7\text{Cu}_{24}\text{Ni}_{10}\text{Co}_3$  were analysed with two different methods. As a first guess the isothermal equilibration curves were fitted with a single-process exponential equilibration. The variation of the deduced time constants with temperature was analysed by means of an Arrhenius equation. An activation energy for volume migration together with a pre-exponential factor was derived. As a second evaluation method the data were fitted using a stretched exponential function. Based on the assumptions made in Sec. 2.3 again useful effective time constants could be derived from the data. Their variation with temperature delivered a mean activation energy for atomic motion during the equilibration process. The measured values are shown again in Tab. 5.4 together with a straight forward Arrhenius analysis of DMA measurements. Due to the large difference in the activation energy values the basic mechanism of the primary  $\alpha$ -relaxation of glass forming liquids

**Table 5.4:** Activation energies  $E_A$  and pre-exponential factors  $\tau_0$  derived from the simple exponential and the stretched exponential analysis (KWW) of the reversible volume equilibration curves. The deviation between the two evaluation methods is low. For comparison also the activation energy for the primary  $\alpha$ -relaxation from DMA measurements is shown. It is not expected that the very low  $\tau_0$  value in this case has a physical meaning. This is also discussed in ref. [81]. (DIL = dilatometer, DMA = dynamic mechanical analysis)

Process	Method	$E_A$ [eV]	$\tau_0$ [s]
Volume equilibration	DIL - exponential	$(2.9 \pm 0.1)$	$7.04 \cdot 10^{(-20 \pm 3)}$
	DIL - KWW	$(3.2 \pm 0.1)$	$5.68 \cdot 10^{(-22 \pm 3)}$
Relaxation	DMA - Arrhenius	$(5.2 \pm 0.2)$	$2.49 \cdot 10^{(-39 \pm 5)}$

should be different to the atomic processes involved in reversible volume equilibration. Basically this behaviour was expected because the reversible volume equilibration process is more likely based on a kind of defect diffusion mechanism. Moreover the response to a significant temperature step is a non-linear process which leads to a new thermodynamic equilibrium and therefore to a new mean energy of the system. This is completely different to the equilibrium relaxation measured in DMA experiments, where the system stays in equilibrium at all times. In Fig. 5.22 the variation of the time constants with temperature are shown in one diagram. It is interesting to notice how the results from the simple exponential analysis (blue and red) fit the results from the much more sophisticated KWW analysis. The reason for this is due to the fact that by fitting the data with one exponential equilibration function very fast and very slow processes are suppressed. The same is true for the calculation of an effective time constant from the KWW fit as described in Sec. 2.3. Nevertheless, the volume equilibration curves, especially at lower temperatures are not well fitted by the simple exponential function.

### Zr<sub>56</sub>Al<sub>7</sub>Cu<sub>24</sub>Ni<sub>10</sub>Co<sub>3</sub> - Fragility

From the DMA measurements the fragility parameter was derived by fitting a VFT-function to the temperature variation of the  $\alpha$ -relaxation time constant. The value reads:

$$D^* = (29 \pm 2)$$

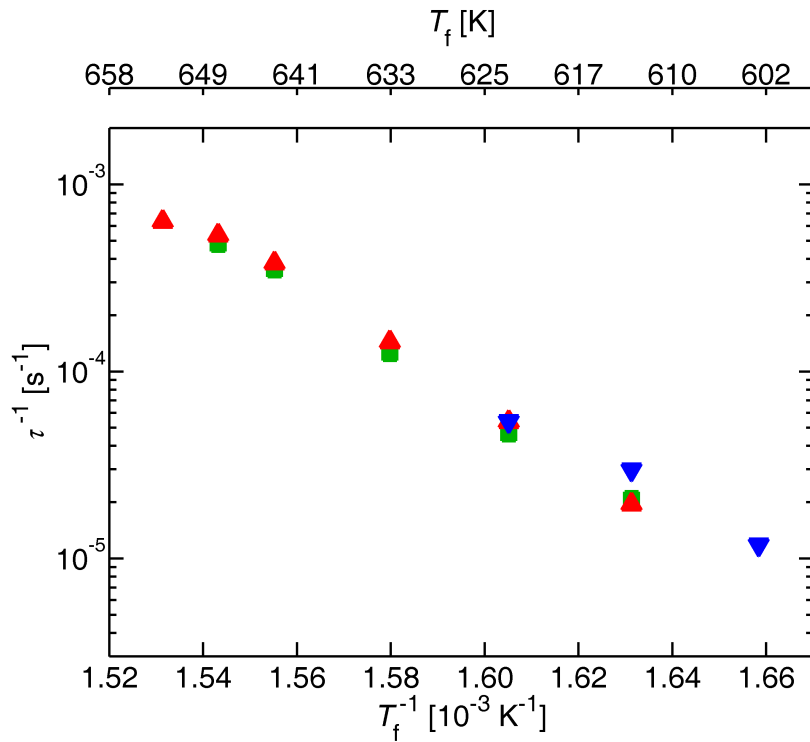


**Figure 5.22:** Arrhenius plot of the time constants derived by fitting an exponential equilibration function (red and blue triangles) and a stretched exponential function (green squares) to the measured Zr<sub>56</sub>Al<sub>7</sub>Cu<sub>24</sub>Ni<sub>10</sub>Co<sub>3</sub> equilibration curves. It is interesting to see how well the two methods are in agreement. No stretched exponential analysis was conducted for the 603 K equilibration because of the very low process amplitude of  $\approx 300$  nm.

This value is very well in the range of values derived for other bulk metallic glasses. In the context of Angell's fragility concept the value defines an intermediate "strength" of the glass. The measured values are shown in Fig. 5.15 in the form of an Angell-plot together with measurements for other glasses from literature. In this plot the abscissa is normalized to the glass transition temperature  $T_g$  which is highly sensitive to the measurement method and heating rate used. Therefore, the assumption that at the glass transition all glasses exhibit a comparable relaxation time is highly questionable. Also the extrapolated value for infinitely high temperatures is only valid in the limit of non-interacting fluid particles. This assumption is reasonable but more high-temperature measurements are necessary to confirm the fitting predictions. At the moment the fitting procedure for most bulk metallic glasses is only possible with strong constraints for the parameters in the VFT equation.

**Zr<sub>52.5</sub>Ti<sub>5</sub>Cu<sub>17.9</sub>Ni<sub>14.6</sub>Al<sub>10</sub>**

In Sec. 5.1.3 extensive reversible isothermal equilibration measurements in the sub  $T_g$  temperature regime for the bulk metallic glass Zr<sub>52.5</sub>Ti<sub>5</sub>Cu<sub>17.9</sub>Ni<sub>14.6</sub>Al<sub>10</sub> were analyzed in terms of a stretched exponential equilibration function. From the fitting functions effective time constants for volume equilibration were calculated according to Eq. 5.13. Their values are tabulated in Tab. 5.3. In an Arrhenius plot (Fig. 5.19) a linear variation of the time constants with temperature was found. Therefore, an activation energy and pre-exponential factor could be derived.

**Atomistic origin of the reversible volume equilibration**

For both glasses under investigation a fully reversible volume equilibration process in the equilibrated glassy state was measured, with respect to the measurement accuracy. This finding is in agreement with results from Ref. 21 where comparable values for the activation energy and the pre-exponential factor were found. The primary volume relaxation of the glass towards equilibrium during annealing below  $T_g$  was not measureable after the long time annealing procedure and, therefore, had no influences on the measurement results. Although the reversible volume equilibration is a phenomenon with very large time constants it is faster than the extrapolation of the primary liquid relaxation time  $\tau_\alpha$  would suggest especially at lower temperatures. In fact, the observed behavior fits much more to a defect-diffusion mechanism such as vacancy migration with a very high migration enthalpy. Because of the difficulties of a vacancy concept in amorphous solids a possibly better explanation would be a free volume migration process for establishing configurational equilibrium in analogy to the equilibrium vacancy concentration in crystalline solids. Because dilatometric measurements could only give information about the absolute amount of volume change, no information about the diffusing species can be derived. Considering the complexity of the discussed quaternary alloys in combination with their amorphous structure a large variety of possible diffusion mechanisms arise. The concept of a more or less continuous spectrum of atomic free volume sizes developed in Sec. 2.3 can help to explain the non-exponential behaviour of the equilibration curves but it cannot give information about the atoms involved in the diffusion process. To get deeper insights and a possible conformation of the proposed diffusion mechanism the results have to be compared with diffusion measurements in comparable materials. In Tab. 5.5 an overview of available tracer diffusion data for bulk metallic glasses is given. For a direct comparison the

results from laser dilatometric measurements are shown in the first lines of the table. Most diffusion experiments were conducted in the supercooled liquid state as well as in the glassy state. This is denoted by the index of the activation energy value in Tab. 5.5. In most experiments much lower activation energies for tracer diffusion are found in the glassy state. There is still an ongoing discussion if this is only a non-equilibrium effect or a true feature of the glassy state [94]. In fact only in Ref. 95 in Tab. 5.5 the glass was long time pre-annealed (up to 1 year) below the calorimetric glass transition temperature to establish an equilibrium prior to the diffusion measurements. In this publication no difference in activation energy for the supercooled liquid and the glass is found after equilibration. Moreover the value found for iron perfectly fits the results from the laser dilatometric measurements in this work and in Ref. 21.

An interesting fact in this context is the vanishing free-volume formation enthalpy if the measured energy values in this work are really the signature of a self-diffusion process. The time dependent behaviour of the isothermal volume equilibration for different temperatures only includes information about the migration enthalpy. If one is interested in the formation enthalpy this is only possible by measuring the process amplitudes when starting from a known free volume concentration. As such a starting concentration is unknown only relative changes in the amplitude can be inferred from the dilatometric measurements. Interestingly it is found that in most measurements (see, e.g., Fig. 5.16) the amplitudes only show very little variation with starting temperature  $T_i$ . It seems as if the energy barrier for formation is very low while it is very high for migration. In this context the equality of the activation energy for tracer diffusion and reversible volume migration is reasonable.

**Table 5.5:** Listing of tracer diffusion activation energies in comparison with laser dilatometric measurement results.  $E_{A,SL}$  denotes the activation energy in the supercooled liquid state and  $E_{A,Glass}$  the activation energy in the glassy state. TD means tracer diffusion and LDIL laser-dilatometer. For the Zr<sub>56</sub>Al<sub>7</sub>Cu<sub>24</sub>Ni<sub>10</sub>Co<sub>3</sub> glass the result of the exponential (this work,1) and the stretched exponential analysis (this work,2) is shown.

Alloy	Atom	$E_{A,SL}$ [eV]	$E_{A,Glass}$ [eV]	Method	Reference
Zr <sub>52.5</sub> Ti <sub>5</sub> Cu <sub>17.9</sub> Ni <sub>14.6</sub> Al <sub>10</sub>	—	—	$3.1 \pm 0.1$	LDIL	this work
Zr <sub>56</sub> Al <sub>7</sub> Cu <sub>24</sub> Ni <sub>10</sub> Co <sub>3</sub>	—	—	$2.9 \pm 0.1$	LDIL	this work,1
Zr <sub>56</sub> Al <sub>7</sub> Cu <sub>24</sub> Ni <sub>10</sub> Co <sub>3</sub>	—	—	$3.2 \pm 0.1$	LDIL	this work,2
Zr <sub>57</sub> Cu <sub>15.4</sub> Ni <sub>12.6</sub> Nb <sub>5</sub> Al <sub>10</sub>	—	—	3.34	LDIL	[21]
	B	2.97	1.80	TD	[96]
Zr <sub>41</sub> Ti <sub>14</sub> Cu <sub>12.5</sub> Ni <sub>10</sub> Be <sub>22.5</sub>	Fe	3.48	1.91	TD	[96]
	Be	4.47	1.05	TD	[96]
	Be	1.90	1.10	TD	[97]
	B	2.59	1.87	TD	[96]
	Fe	3.16	2.11	TD	[96]
Zr <sub>46.7</sub> Ti <sub>8.3</sub> Cu <sub>7.5</sub> Ni <sub>10</sub> Be <sub>27.5</sub>	Co	3.00	2.01	TD	[96]
	Al	4.10	—	TD	[96]
	Ni	2.76	—	TD	[98]
	B	2.59	2.56	TD	[95]
	Fe	3.16	3.14	TD	[95]
Zr <sub>65</sub> Cu <sub>17.5</sub> Ni <sub>10</sub> Al <sub>7.5</sub>	Ni	2.96	—	TD	[99]
Zr <sub>55</sub> Cu <sub>25</sub> Ni <sub>10</sub> Al <sub>10</sub>	Ni	—	0.95	TD	[100]
Pd <sub>40</sub> Cu <sub>30</sub> Ni <sub>10</sub> P <sub>20</sub>	Ni	—	2.89	TD	[100]
	Pd	—	3.45	TD	[100]
Ni <sub>18</sub> Zr <sub>65</sub> Al <sub>17</sub>	Co	—	1.50	TD	[101]
Ni <sub>18</sub> Zr <sub>57</sub> Al <sub>25</sub>	Co	—	2.10	TD	[101]
Ni <sub>19</sub> Zr <sub>62</sub> Al <sub>19</sub>	Cu	—	1.80	TD	[101]
Ni <sub>17</sub> Zr <sub>64</sub> Al <sub>19</sub>	Ti	—	1.95	TD	[101]

## 5.2 The glass transition

In the previous section the kinetics of reversible volume equilibration in two different metallic glasses was studied. This was done by analyzing the time-dependent equilibration after fast, up- or down-quenching steps in the order of 20 K. In contrast to these measurements, the aim of the experiments and results described in this section is to analyze the sub- $T_g$  equilibrium volume evolution upon slow, continuous heating. One of the most challenging open questions regarding the glassy state of matter is whether the glass transition is a purely kinetic phenomenon or a real phase transition in the limit of infinitesimal small heating or cooling rates [4, 102]

$$\frac{\Delta T}{\Delta t} \rightarrow 0. \quad (5.15)$$

A fundamental property of a liquid is the existence of a main structural relaxation time  $\tau_\alpha$  with the meaning that after a mechanical perturbation the system relaxes back to its equilibrium without retaining any information about the interfering event. When a glass forming system falls out of equilibrium due to a kinetic glass transition the relaxation time  $\tau_\alpha$  becomes usually strongly time dependent at lower temperatures. This behaviour is called ageing and is observed in all glass forming materials [17]. As long as the system is not in equilibrium the primary relaxation behaviour is not accessible because the fluctuation-dissipation theorem does not hold for out-of-equilibrium systems (see Sec. 2.2 for details). An exception from this rule is only possible if the equilibration, i.e., the change of the expectation value of thermodynamic variables of the system like energy or volume, is orders of magnitude slower than the structural relaxation [4]. The divergence of the main structural relaxation time at a finite temperature would cause the system to form an ideal glass because not all points in phase space would be accessible anymore. Therefore, the measurement of  $\tau_\alpha$  is crucial to decide experimentally whether there exists an ideal glassy state. This is an experimentally challenging task and up to now no measurements in this direction were able to answer the glass transition question.

An alternative approach to the proof of a divergence of the structural relaxation time at finite temperatures would be a distinct change in a thermodynamic variable like, e.g., volume or energy in equilibrium at a fixed temperature. Like every phase transition also an ideal glass transition would have a distinct signature in the thermodynamic variables of the system. In Fig. 5.23 a schematic illustration of the change of volume or energy of a glass forming liquid with temperature is shown. The question of the

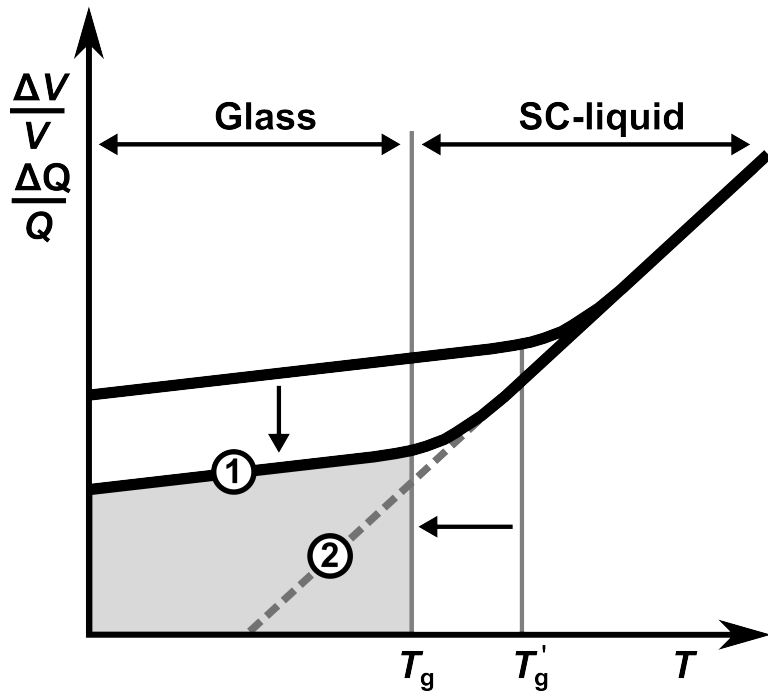


**Figure 5.23:** Schematic representation of the change in volume or energy of a glass forming liquid. At an apparent glass transition temperature  $T'_g$  the system falls out of equilibrium because the cooling rate becomes faster than the structural relaxation. In equilibrium two behaviors are possible. (1) The liquid forms an ideal glass, i.e., a glass transition also exists in the equilibrium state and therefore the glass transition is a true thermodynamic phase transition at  $T_g$ . (2) The material equilibrates to the liquid state at all temperatures when the equilibration time is chosen long enough.

existence of a true thermodynamic glass transition can be reduced to the question whether there is a distinct change in the volume or energy of the system at a certain, fixed temperature in equilibrium. However, the equilibrium condition Eq. 5.15 is difficult to fulfil because in most dilatometric or calorimetric measurements heating rates in the order of a few Kelvin per minute are used [8, 10, 11]. This limitation is due to the resolution limits of conventional measurement devices. In the following an approach for overcoming these limitations with a high resolution laser-dilatometer is presented and the obtained experimental results are discussed.

### Measurement procedure

The same sample equilibration procedure as in the measurements from the previous sections was used to establish an equilibrated starting point for the measurements. The specimen was pre-annealed for 27d with a final annealing temperature of 573 K which is 83 K below the calorimetric glass transition determined at 5 K/min. The basic idea

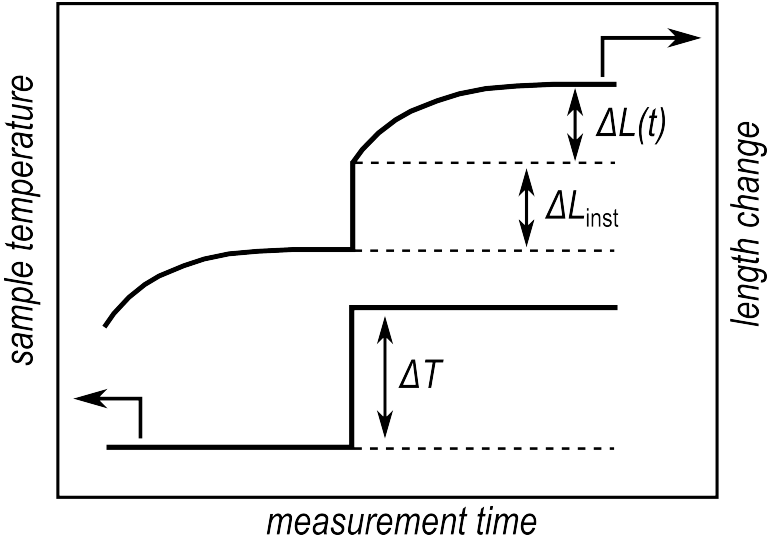


**Figure 5.24:** Schematic drawing of the measurement procedure to best fulfill Eq. 5.15. Starting at a temperature where the system is equilibrated, small temperature steps with subsequent equilibration phases are conducted. The length change of the sample can be split into two parts: The instantaneous part  $\Delta L_{\text{inst}}$  described by the thermal expansion coefficient  $\alpha$  and the time dependent part  $\Delta L(t)$  caused by volume equilibration.

to fulfil the condition of a heating rate as low as possible (Eq. 5.15) is the introduction of finite but small (5 or 10 K) temperature steps followed by long, isothermal volume equilibration phases. The process is schematically shown in Fig. 5.24. The whole length change  $\Delta L$  of the sample after such a single step can be defined as

$$\Delta L = \Delta L_{\text{inst}} + \Delta L(t) \quad (5.16)$$

where  $\Delta L_{\text{inst}}$  is the instantaneous length change caused by the thermal expansion of the material and  $\Delta L(t)$  is the volume change due to the volume equilibration process. From  $\Delta L_{\text{inst}}$  in Eq. 5.16 the variation of the thermal expansion coefficient of the material with temperature is directly accessible. The total amount of the specific volume change is calculated using the approximation already defined in Eq. 4.9. The total amount of relative volume  $\frac{\Delta L}{L}$  created after  $N$  temperature steps is then given by

$$\frac{\Delta V}{V} = \sum_{i=1}^N \frac{3\Delta L(t)_i}{L_0}. \quad (5.17)$$

The thermal expansion coefficient  $\alpha$  can be calculated according to

$$\alpha(T) = \frac{1}{L(T)} \cdot \frac{\Delta L_{\text{inst}}(T)}{\Delta T}, \quad (5.18)$$

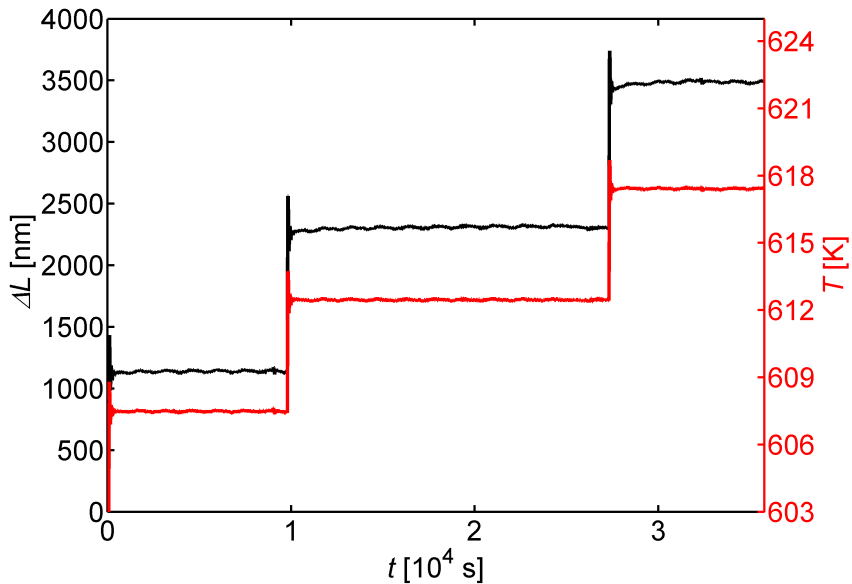


**Figure 5.25:** Three subsequent length change measurement steps as a function of time as recorded by the laser-dilatometer. The instantaneous length change upon every temperature step of 5 K is in the order of 1000 nm. The length change due to time dependent equilibration is about an order of magnitude smaller and therefore not visible in this representation.

where  $L(T)$  is the total sample length at the measurement temperature  $T$ .

### Measurement results

The measurement process as sketched in Fig. 5.24 is shown for a real measurement in Fig. 5.25. The instantaneous length change  $\Delta L_{\text{inst}}$  upon every temperature step is of the order of 1000 nm at a temperature step size of  $\Delta T = 5$  K. The time dependent length changes  $\Delta L(t)$  following the instantaneous expansions  $\Delta L_{\text{inst}}(t)$  are more than one order of magnitude smaller ( $\Delta L(t) \ll \Delta L_{\text{inst}}$ ) and therefore hard to recognize in the representation. In Fig. 5.26 four time dependent equilibration curves  $\Delta T = 10$  K (upper left panel),  $\Delta T = 5$  K (upper right and lower left panel) and  $\Delta T = 25$  K (lower right panel) are shown. In these figures the contribution of  $\Delta L_{\text{inst}}$  has been omitted. The curve in the upper left panel was also the first measurement after the long-time equilibration of the sample. In this measurement the equilibrium state of the sample was ensured by choosing a measurement time approximately 7 times longer than expected for the volume equilibration. With respect to the measurement resolution no length change is visible up to a measurement time of approximately  $8 \cdot 10^4$  s. Thus, the volume change is solely due to the specific volume change upon temperature increase

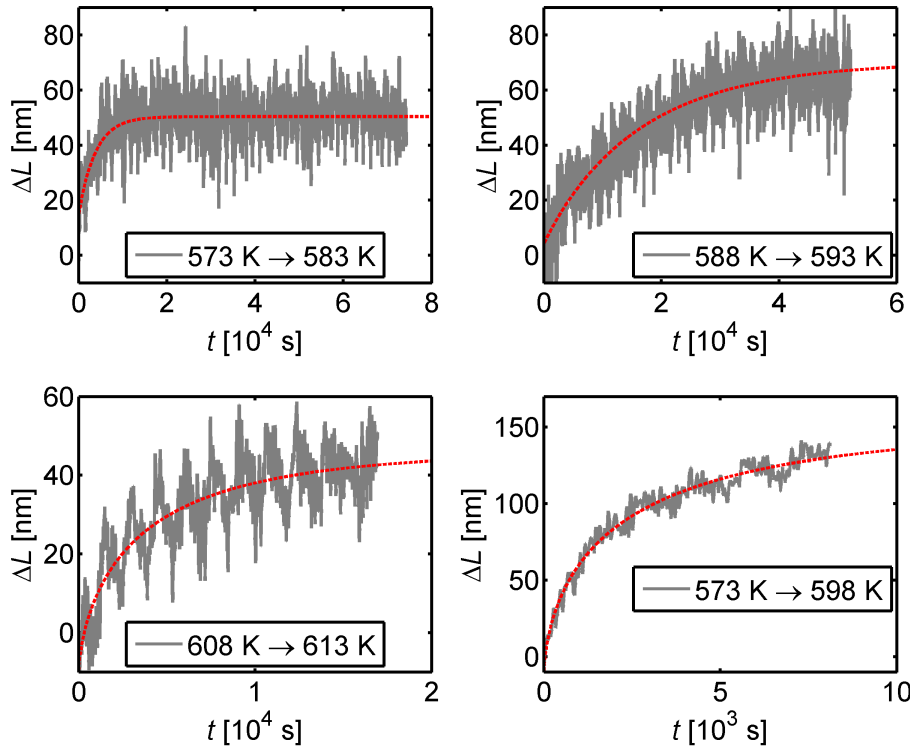


**Figure 5.26:** Examples of time dependent length change equilibration curves. The temperature steps are indicated by the insets in the panels. The fits are only used to better estimate the finale amplitude of the curves. The noise in the curves can be attributed to the air-conditioning of the laboratory, causing effective temperature changes of the interferometer base plate of about  $\pm 0.02$  K.

starting from a completely equilibrated state and ending in an equilibrated state. The noise which is visible in all measurements is caused by thermal influences on the interferometer, mainly caused by the air-flow of the air-conditioning system in the laboratory. The larger temperature step of 25 K depicted in the lower right panel of Fig. 5.26 was a check for reversibility and is later on explained in more detail. All fits in Fig. 5.26 are only used for "de-noising", i.e., smoothing, of the measurement curves to obtain reproducible results for the total length change after the equilibration. In Fig. 5.27 equilibration curves for higher measurement temperatures and larger temperature steps are shown. The 653 K measurement was the last dilatometric measurement and interrupted because of the large volume gain.

The cumulated volume gain according to Eq. 5.17 that is due to equilibration is shown in Fig. 5.28. Starting at the final pre-annealing temperature of 573 K the equilibrium volume increases linearly up to about 630 K where a distinct change in slope is visible

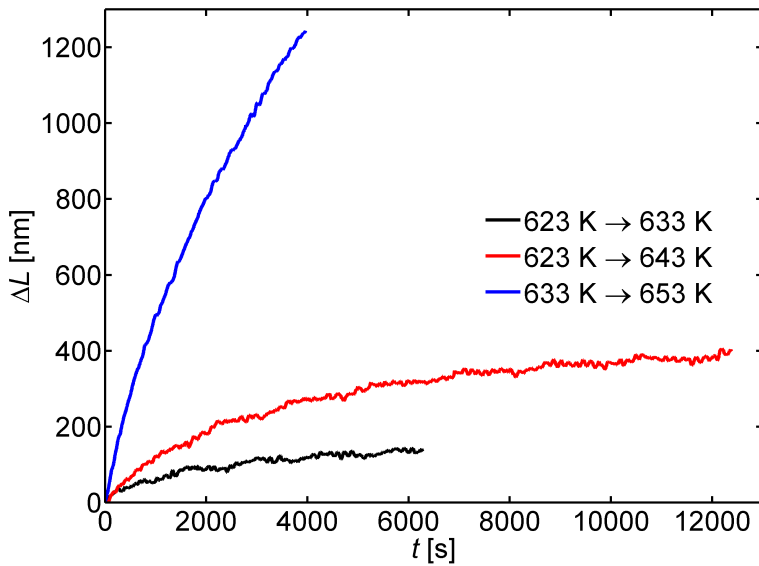


**Figure 5.27:** Higher temperature equilibration curves. The last measurement for 653 K was interrupted because of the large volume formation.

as indicated by the vertical blue dashed line in Fig. 5.28. The lower temperature data points were checked for reversibility. This is indicated by the green triangle data point at 598 K. To get this data the sample in equilibrium at 598 K was annealed again at 573 K until no more change in length, i.e., shrinkage, was measurable. Subsequently the temperature was increased in one step to 598 K causing the volume to increase to exactly the same value as in the four cumulated smaller temperature steps before. The red data points in the higher temperature regime are results from a second, higher temperature measurement run. For this purpose the glass was re-equilibrated at 623 K as a new starting point. The calorimetrically determined glass transition temperature for the alloy is indicated in the graph of Fig. 5.28 by the red vertical line at 659 K. It was determined as the onset of glass transition in a 5 K/min DSC experiment with the same sample material.

From the instantaneous length changes  $\Delta L_{\text{inst}}$  the actual value of the thermal expansion coefficient  $\alpha$  was determined according to Eq. 5.18. Its equilibrium value evolution is shown together with the relative specific volume change of the sample in Fig. 5.29. The expected parabola like increase upon approaching the calorimetric glass transition is interrupted at approximately 620 K, which is near to the kink of the temperature behaviour of the cumulated volume change.

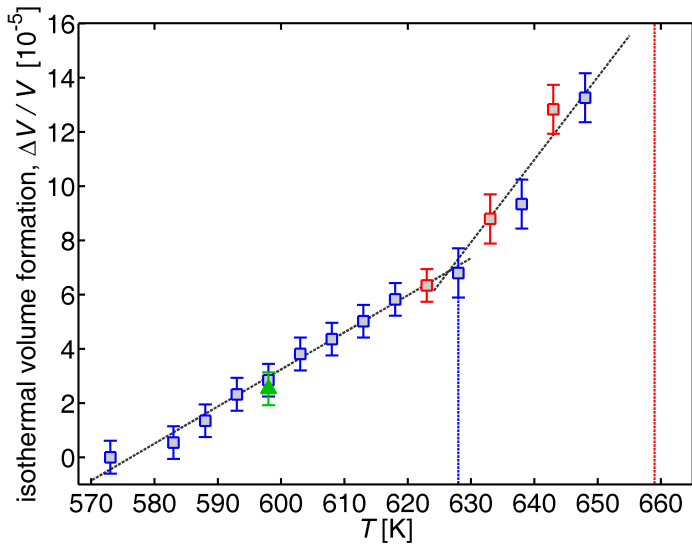


**Figure 5.28:** The cumulated relative volume change of the sample according to Eq. 5.17. A distinct change in volume formation at approximately 628 K indicated by the blue vertical dotted line, is visible. This temperature is about 30 K lower than the calorimetrically determined onset of the glass transition measured at 5 K/min, indicated by the red vertical dotted line. The green and red data points indicate reversibility checks. The reader is referred to the main text for details.

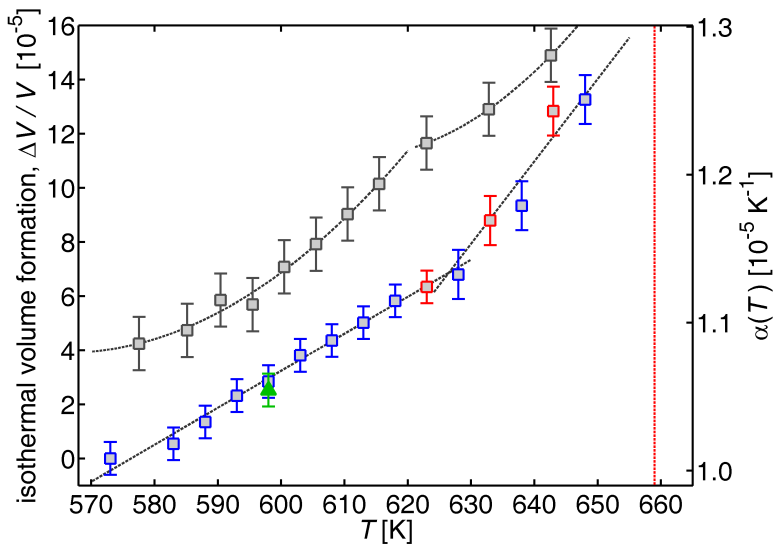


**Figure 5.29:** The equilibrium thermal expansion coefficient  $\alpha$  of the material (grey squares, right ordinate) and the relative volume change (data points are the same as in Fig. 5.28, left ordinate). The monotonically increasing behaviour of the expansion coefficient changes at approximately 620 K, which is in the same temperature region as the kink in the specific volume evolution.

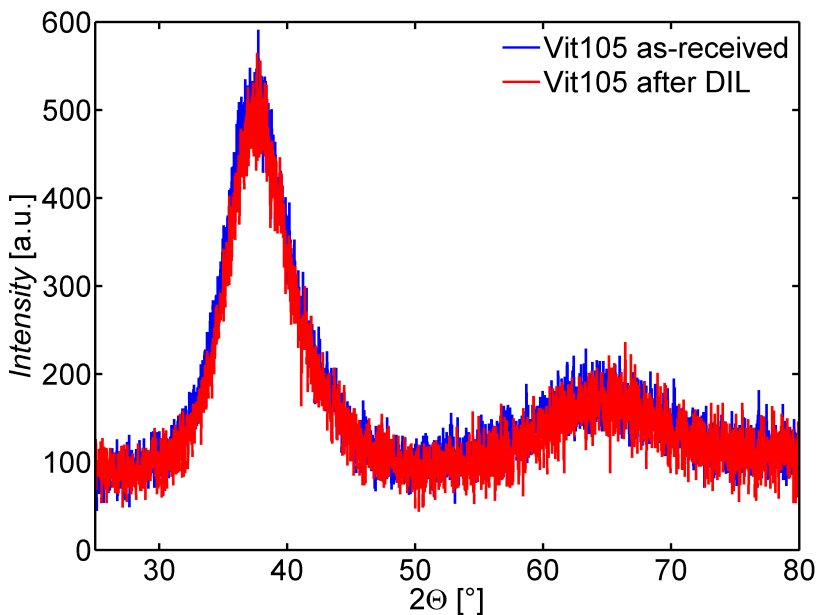


**Figure 5.30:** X-ray diffraction patterns of the as received sample (blue) and the sample after the long-time pre-annealing of the dilatometric measurements (red). The patterns are superimposed to better assess differences.

### X-ray diffraction

The X-ray diffraction patterns for the as-received state of the material and the material after the long-time pre-annealing of the dilatometric measurements are shown in Fig. 5.30. The two patterns are plotted over each other to better assess differences. With respect to the sensitivity of the diffractometer, no signs of structural changes are visible after the dilatometric measurements.

### Discussion

The presented results in this section show a distinct change in the equilibrium volume as well as in the equilibrium thermal expansion coefficient of a bulk metallic glass far below its calorimetrically determined glass transition temperature. Considering the resolution of the dilatometer of  $\frac{\Delta V}{V} = 1.5 \cdot 10^{-6}$  and the fact that no irreversible behavior was observed on timescales of  $10^6$  s the observations can be attributed to a glass transition in the equilibrated state at  $T_g = 628$  K.

Traditional dilatometric or calorimetric measurements are difficult to compare with the presented results because of significant differences in the measurement procedure.

At first conventional dilatometers are usually less stable to perform long-time isothermal measurements. Second, the resolution of a conventional push-rod dilatometer is not high enough to perform an equal measurement procedure as presented in this section. Calorimetric measurements would be a possibility for comparative studies but no equilibrium measurements below  $T_g'$  are known to the author.

One quantity which is directly linked to the equilibrium volume of the glass is the elastic modulus. As long as the volume is equally distributed the change in the mean interatomic spacing would have an impact on the Young's or shear-modulus, respectively. In measurements where the isothermal equilibration of the moduli was studied a similar time dependent behaviour as for the volume in the presented measurements was found [103–105]. Especially in Ref. 106 it is reported that the shear modulus of strongly pre-annealed Pd-based bulk metallic glass shows a distinct deviation, i.e, kink in the temperature behaviour approximately 40 K below the calorimetrically determined glass transition. This result perfectly agrees with the results presented here. However, in Ref. 106 the kink temperature is discussed in the framework of the Kauzmann temperature introduced by Walter Kauzmann to resolve the paradoxon of a vanishing entropy difference between the liquid and its corresponding crystal at finite temperatures [107]. In the author's opinion the much more interesting question is whether the kink temperature corresponds to some divergence point of the primary relaxation time  $\tau_\alpha$  of the liquid. This would directly entail that the system cannot reach every point in phase space at lower temperatures and therefore would form an ideal glass. To clarify this, additional measurements in equilibrated glassy systems are necessary. Especially a convenient answer to the origin of the reversible volume formation process in terms of a microscopic theory would probably contain the solution to the glass transition problem.

### 5.3 The specific volume on a local atomic scale

I this section results from the positron annihilation measurements on the bulk glassy alloy Zr<sub>52.5</sub>Ti<sub>5</sub>Cu<sub>17.9</sub>Ni<sub>14.6</sub>Al<sub>10</sub> performed by coincident Doppler broadening spectroscopy at the NEPOMUC positron beam line of FRM II are presented. A short introduction to standard and coincident Doppler-spectroscopy is given in Sec. 3.3 to get an idea of possible interpretations of the presented measurement results and the used parameters.

#### Measurement procedure

Plates with dimensions 6 x 20 x 0.5 mm<sup>3</sup> were cut from the same Vit105 ingots as used for the dilatometric measurements presented in the previous sections. The plates were placed on a sheet of molybdenum inside the vacuum chamber of the positron spectrometer. Variable sample potentials between 1 and 30 kV were used for all measurements. Sample heating was realized with a controlled halogen-bulb located underneath the molybdenum sheet. The sample temperature was measured with a calibrated pyrometer.

#### Parameter $S(E)$ and $W(E)$ in the glassy state

As a first step the S and W-parameter for an equilibrated Vit105 sample as a function of positron energy were measured. The pre-annealing procedure for equilibration was the same as described in the previous section (27d at 573 K see: 5.1.3). In Fig. 5.31 the S parameter is plotted versus energy for four different temperatures. All measurements are in the glassy state, the last temperature of 593 K is 60 K below the onset of the glass transition as calorimetrically determined at 5 K/min. The penetration depth of the positrons varies with their kinetic energy. Below approx. 10 keV the value for the S parameter has not reached its bulk value because of surface effects, e.g., crystalline oxides and escape of positrons from the sample surface. Above 10 keV a steady value for the S parameter because of predominant bulk annihilation is reached for all temperatures. The bulk value of the S parameter decreases with increasing temperature. This is an indication that, at least at this timescales no localized free volume is formed in the glass. The recording time for one data point was 1 min for all measurements. In Fig. 5.32 the corresponding W-parameters for the same measurements are shown. As for the S-parameter the bulk value is reached at approx. 10 keV. The value for The W parameter is significantly higher for the two higher

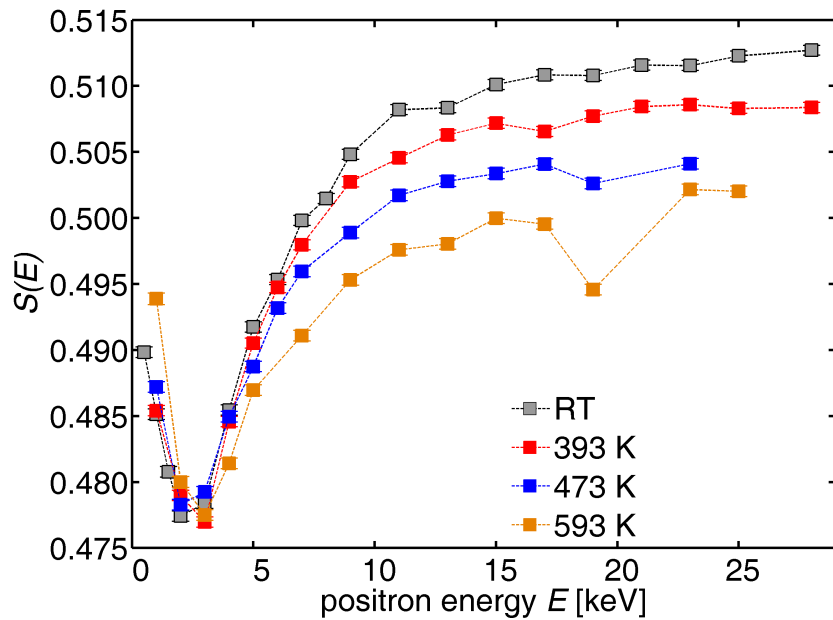


**Figure 5.31:** The S-parameter measured for different temperatures and energies. RT denotes room temperature, measurement time for each data point was 1 min. A continuous decrease in the bulk value of the S-parameter with temperature can be observed. The behavior at low energies can be attributed to surface and positron escape effects.

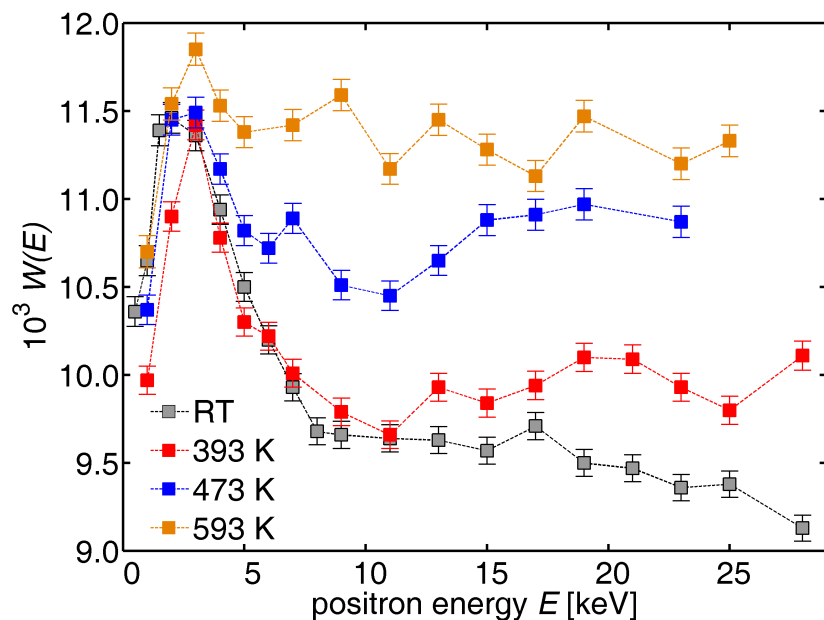


**Figure 5.32:** The W-parameter measured for different temperatures and energies. Measurement time was 1 min for each data point as in Fig 5.31. The bulk value is significantly higher for the higher measurement temperatures.

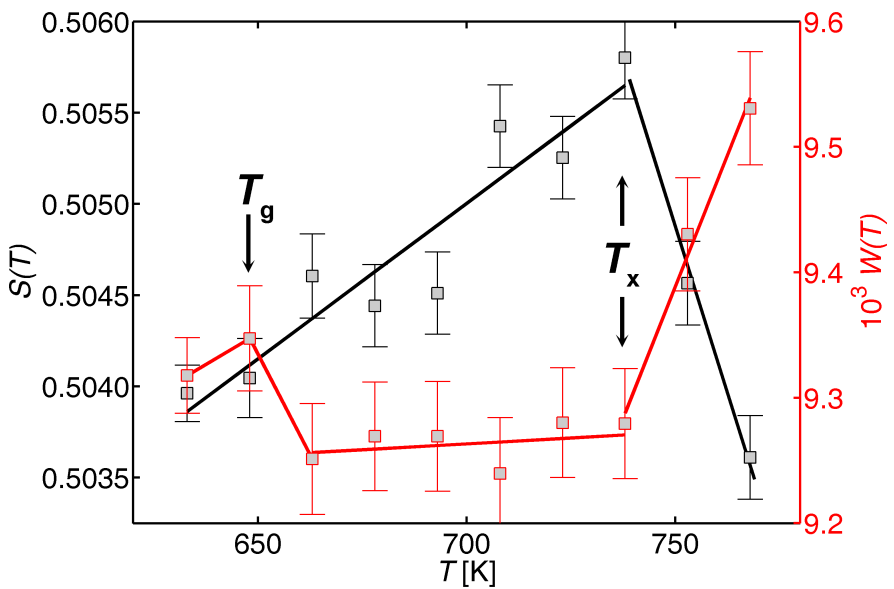


**Figure 5.33:** The variation of the S and W-parameter with temperature in the supercooled liquid state. The glass transition temperature  $T_g$  is indicated by a crossover at 653 K. In the supercooled liquid the S-parameter increases monotonically while the W-parameter stays constant. A strong change is observed upon crystallization at approx.  $T_x = 750$  K.

temperature measurements, thus the annihilation probability with core electrons seems to increase.

### Glass transition and crystallization

In Fig. 5.33 changes of the S and W-parameter with temperature for the glass transition, the supercooled liquid state and the crystallization temperature region is shown. The glass transition temperature is 653 K for a heating rate of 5 K/min. Upon reaching the supercooled liquid the S parameter starts to increase while the W-parameter stays more or less constant. This can be attributed to rapid, de-localized free volume generation in the glass at temperatures higher than the calorimetric glass transition. In contrast the annihilation with core electrons should not be affected significantly by this phenomenon which is confirmed by the W-parameter. As a consequence of crystallization a strong change in the parameters is visible at 750 K. This is expected because the structure of the material changes completely at this point.

### Parameter $S(E)$ and $W(E)$ : glass - crystal

In Fig. 5.34 the S-parameter is plotted versus energy for the glassy sample at room temperature (RT), two high temperature measurements in the glassy state (613 and

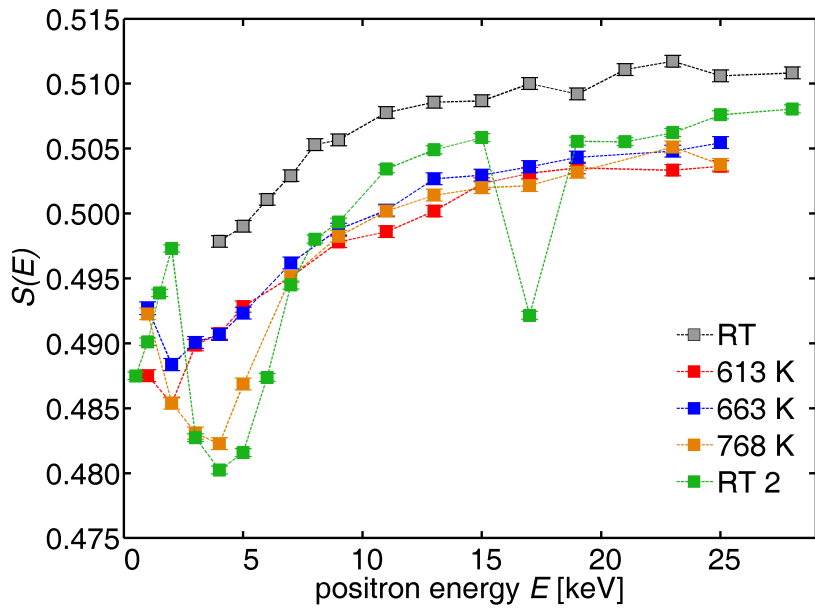


**Figure 5.34:** The S-parameter for different temperatures in the amorphous and crystalline state. Here RT denotes room temperature measurements measurement time for each spectrum was 1 min. The S-parameter for the higher temperature measurements in the glassy state are comparable to the crystalline results at 768 K and RT 2.

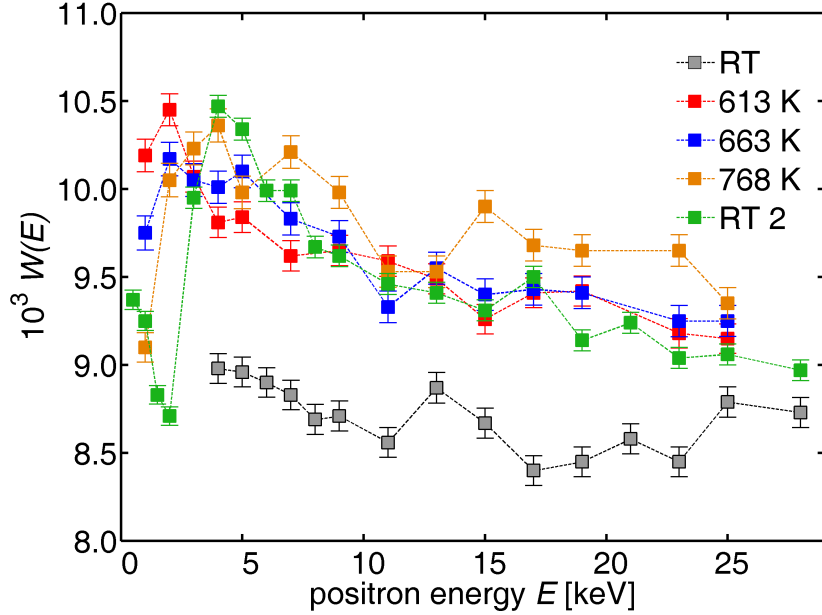


**Figure 5.35:** The W-parameter for different temperatures in the amorphous and crystalline state of the investigated material; RT denotes room temperature measurements. The equivalence of measurement results for the higher temperature glassy measurements and the crystalline material indicate a comparable chemical environment of the annihilation site in both states.

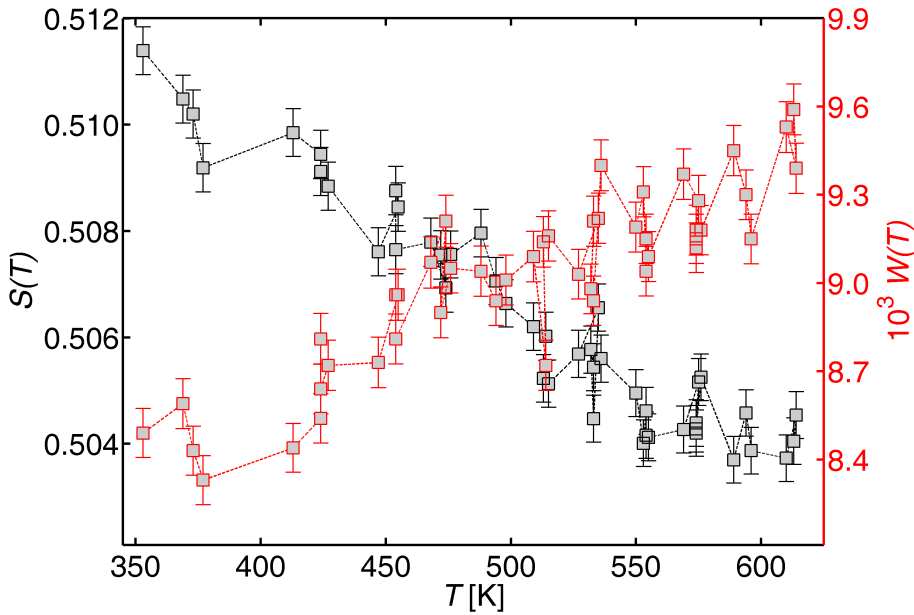


**Figure 5.36:** Variation of the S and W parameter with temperature; measurement time for each data point was 1 min, a monotonic increase or decrease is observed, respectively.

663 K) and a high and low temperature measurement in the crystalline state (768 K and RT 2). The higher temperature glass measurements only show little differences. Interestingly also the crystalline material at 768 K shows a comparable behaviour at higher potentials. The W-parameter in Fig. 5.35 also shows similarities in the higher temperature measurements in the glassy and crystalline state. Because this parameter is a measure for a relative change in the chemical environment of the annihilation site, it can be inferred that most probably the short range order in the highly pre-annealed glass is comparable to the short range atomic arrangement in the crystal. This is also supported by the measurement at room temperature (RT 2) where no significant differences to the higher temperature glass measurements are visible.

#### Parameter $S(T)$ and $W(T)$ : glassy state

The continuous variation of the S and W parameter (1 min measurement time for every spectrum) with temperature in the glassy state is shown in Fig. 5.36. The same behaviour which was already observed in the  $S(E)$  and  $W(E)$  measurements in Fig. 5.31 and 5.32 is found. The S-parameter decreases with temperature while the W-parameter increases. The increase and decrease are rather smooth which could be interpreted as a continuous increase in de-localized volume, i.e., due to thermal expansion of the material. No signs of localized free volume like vacancy type defects can be found.

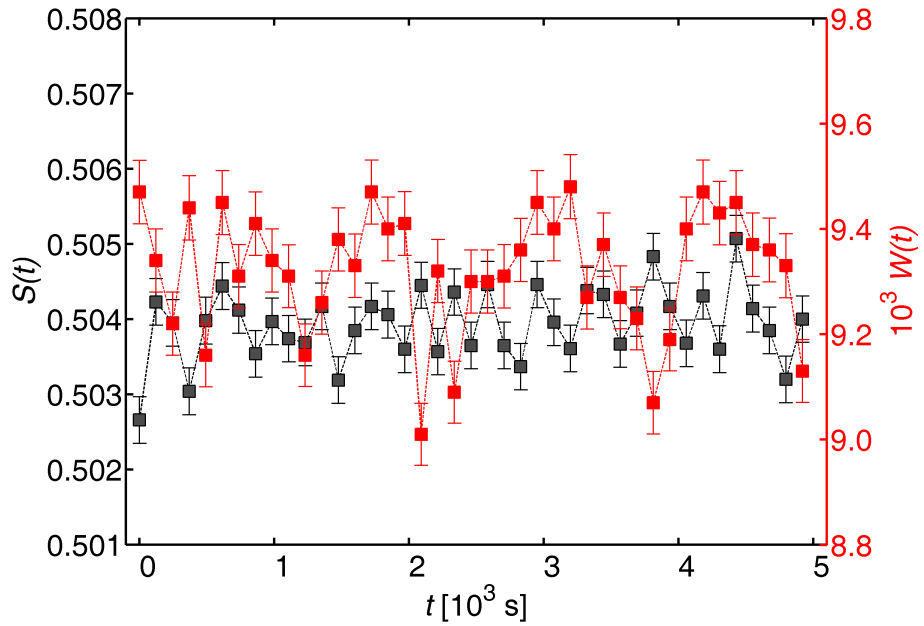


**Figure 5.37:** Isothermal measurement of the S and W-parameter. Measurement temperature was 593 K, measurement time for each spectrum, 2 minutes.

#### Parameter $S(t)$ and $W(t)$ : glassy state

An isothermal measurement at 593 K of the S and W-parameter for the pre-annealed sample in the glassy state heated from room temperature is shown in Fig. 5.37. With respect to the measurement resolution no changes in the S and W parameter can be found in the investigated time window. An isothermal equilibration due to vacancy type defect formation is not observed.

#### Coincident Doppler broadening

For the coincident Doppler-broadening (CDB) measurements it was decided to compare an as-quenched sample and a pre-annealed one, at room and at elevated temperature. To get useful results in terms of statistics the measurement time for a single spectrum was approx. 20 mins. The sum of 12 spectra was considered as final spectrum at the respective temperature shown in Fig. 5.38. Although the measurement time is much higher as for the simple S and W parameter, compared to standard laboratory equipment it is still two orders of magnitude faster. All measurements were performed relative to a high-purity Zr-metal disk according to Eq. 3.4. The results for the as-quenched and pre-annealed sample are shown in Fig. 5.38. In this plot the equilibrated sample is denoted by ES and the quenched sample with QS followed by

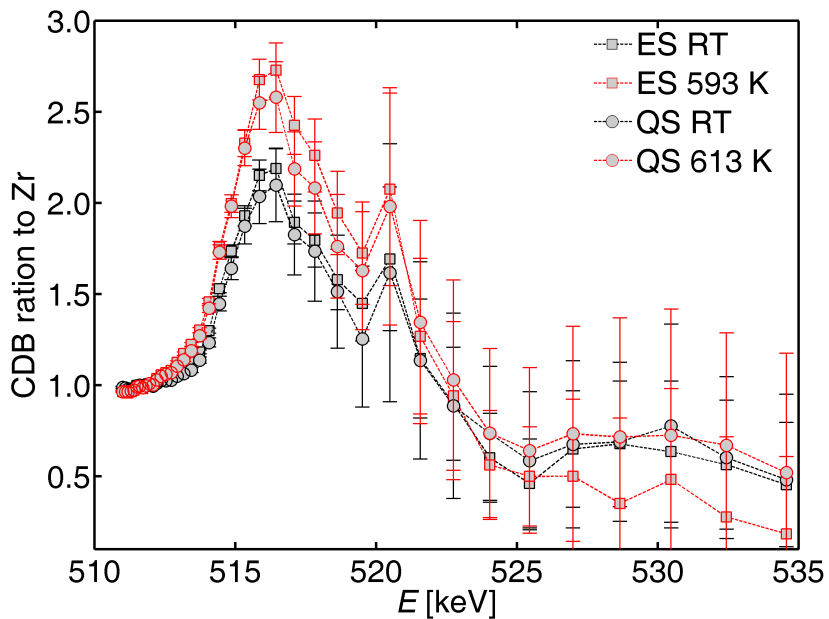


**Figure 5.38:** Coincident Doppler-spectra normalized to pure zirconium for the Vit105 sample material in different conditions. Here ES denotes the equilibrated sample with 27 day pre-annealing at 573 K, and QS denotes the quenched sample, without annealing after production.

the measurement temperature. Neither the low temperature measurements, nor the high temperature measurements for both material conditions show significant differences. Minor deviations are visible in the high energy-shift regime for the equilibrated sample. Nevertheless the uncertainty of this measurement points is much higher than the observed deviations in the element signature.

## Discussion

In this section results from comprehensive positron annihilation experiments on bulk metallic glass samples, with a high intensity positron beam have been presented. Because of the complexity of the amorphous multi atom structure of the alloy under investigation a mathematical interpretation of positron results is quite complex. Therefore, the measurements will only be interpreted in a qualitative way. Nevertheless some conclusions can be drawn from the measurements:

- The  $S(E)$  and  $W(E)$  results in the glassy state confirmed the constitutional homogeneity of the investigated samples.

- No localized vacancy-type defect formation was found in any of the measurements.
- The W-parameter for higher temperature glass measurements are comparable to the results in the crystalline state, indicating that the annihilation environment is comparable in both states.
- The element signature for zirconium in a CDB measurement for different sample conditions and temperatures does not change significantly. This supports the assumption that the chemical short range order only shows little variation with sample condition.

## 5.4 Low-temperature crystallization kinetics

In this section the crystallization kinetics of Vit105 are studied by a newly developed method which allows the direct measurement of a phase transformation. The results are analysed and discussed in comparison with other measurement techniques.

### Motivation

The knowledge of the crystallization behavior of glasses and especially of bulk metallic glasses is of vital importance for the processing of these materials. The measurement of crystal nucleation and growth in deeply undercooled liquids is possible by a variety of techniques; calorimetry and X-ray diffraction are two prominent examples [108, 109]. However, the monitoring of the start and finish times of crystallization especially on very long timescales remains a difficult task. Therefore, the range of available time-temperature-transformation diagrams (TTT) for bulk-metallic glasses is limited to times shorter than  $10^4$  s. The indication for crystallization in calorimetric measurements is the heat generated by the exothermic crystallization process. On long time scales the signal per unit time ration becomes very small and the method is very prone to error, e.g., due to oxidation heat even in high purity protective gas environments. In contrast, another distinct feature of a unique phase in equilibrium is its thermal expansion coefficient. The interatomic potentials, which are the origin of this quantity, are not affected by environmental conditions. Therefore, the continuous measurement of the thermal expansion coefficient of a sample under isothermal conditions would instantly show a phase separation of the matrix.

A material consisting of  $N$  phases with thermal expansion coefficients  $\alpha_1 \dots \alpha_N$  shows the macroscopic expansion coefficient

$$\bar{\alpha} = \sum_{i=1}^N \alpha_i X_i, \quad (5.19)$$

with

$$\sum_{i=1}^N X_i = 1, \quad (5.20)$$

where  $X_i$  is the relative amount of phase  $i$ . For a two-phase system the exact amount of each phase can be calculated by knowing the expansion coefficients  $\alpha_1$  and  $\alpha_2$  and

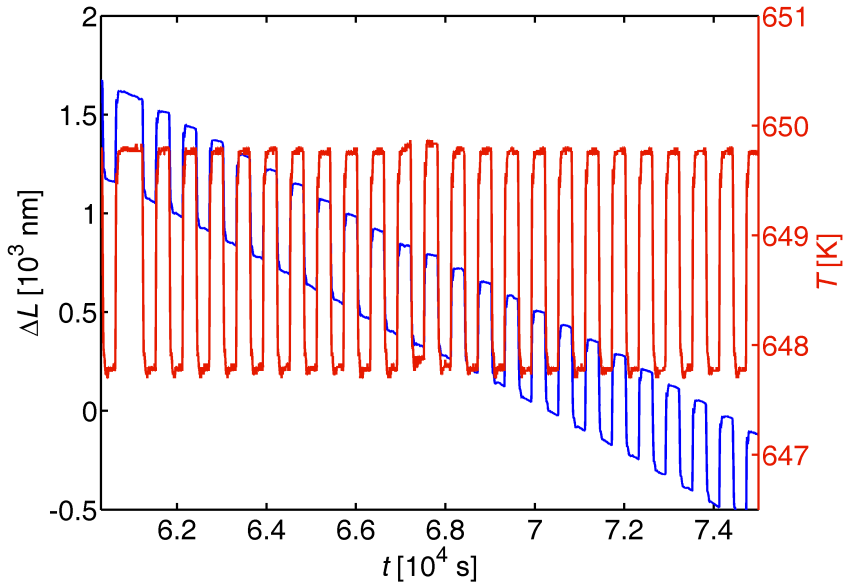


**Figure 5.39:** Excerpt of a measurement of the modulated sample temperature together with the length change signal (blue). The length change is superimposed by small periodic variations for measuring the thermal expansion coefficient of the sample as a function of time.

measuring  $\bar{\alpha}$ . In the following a method for the measurement of  $\bar{\alpha}$ ,  $\alpha_1$  and  $\alpha_2$  under quasi-isothermal conditions is presented.

### Measurement procedure

In the kinetics section of this work the isothermal equilibration of a material due to defect or free volume migration was studied by controlling the sample temperature to a constant value with a maximal relative offsets of  $\pm 0.02$  K. For measuring the instantaneous thermal expansion coefficient a fast but, with respect to the measurement resolution, small temperature step  $\Delta T = T_{\text{high}} - T_{\text{low}}$  is necessary. The measurement principle to simultaneously assess the specific volume evolution and the thermal expansion coefficient at any time of the experiment is described in Sec. 4.3. The specific modulation of the sample temperature used for the presented measurement is shown in Fig. 5.39. In this case a temperature oscillation with an amplitude of 1 K and a period of 300 s around 649 K were used. From each oscillation period an instantaneous value for the thermal expansion coefficient  $\alpha_{\text{inst}}$  can be calculated according to

$$\alpha_{\text{inst}}(T) = \frac{1}{(L_0 + L(T))} \cdot \frac{\Delta L}{T_{\text{high}} - T_{\text{low}}}, \quad (5.21)$$

where  $L_0$  is the sample length at time  $t = 0$  and  $L(T)$  is the actual length. The response of the length signal to the temperature variation is shown in blue on the left ordinate in Fig. 5.39. If one considers that at  $t = 0$  a single-phase material with  $\alpha_1$  and at  $t = \infty$  a single-phase material with  $\alpha_2$  exists. The instantaneous expansion coefficient  $\alpha_{\text{inst}}$  corresponds to  $\bar{\alpha}$  in Eq. 5.19. Therefore, the relative amount of phase 1 and 2 is known at any time of the experiment. If a very slow process like low temperature crystallization is studied it is in principle sufficient to determine the instantaneous expansion manually for distinct times. In reality the continuous modulation is necessary because a reliable value for  $\alpha_{\text{inst}}$  can only be obtained by calculating the mean instantaneous length change from many temperature steps. This is necessary because the changes in  $\bar{\alpha}$  can be very small, especially if  $\alpha_1$  and  $\alpha_2$  are of comparable size. In this work the raw data from 72 temperature steps was sampled for calculating one data point of  $\bar{\alpha}$ . This sampling value should only be seen as an example because it strongly depends on the temperature difference  $T_{\text{low}} - T_{\text{high}}$  and the difference in  $\alpha_1$  and  $\alpha_2$  of the specific case investigated.

## Crystallization kinetics

If the amount of a forming phase, e.g., crystals in a crystallization process, can be measured over time an analysis of the kinetics governing the formation and growth process is possible. One of the most commonly used models to describe phase formation and in general processes where a nucleation and growth process is observed, is the Johnson-Mehl-Avrami-Kolmogorov (JMAK) model [110–112]. The model is based on the assumptions that the critical radius of the nuclei is zero and nuclei form equally distributed throughout the volume. Therefore, it is better suitable for solid/solid reactions than for liquid/solid ones because of the difficulty to fulfil criteria of homogeneous nucleation in the latter case. Fortunately, the deeply undercooled liquid of a metallic glass can be treated as a quasi-solid in this relation because of its very high viscosity. The JMAK-model used for analyzing the crystallization process of the bulk metallic glass in this work is given by the equation

$$X(t) = A \cdot (1 - \exp(-(K \cdot (t - \tau))^n)) + B, \quad (5.22)$$

with  $X(t)$  the crystallized fraction at time  $t$ ,  $A$  denotes the amplitude of the process,  $B$  is the initial value and  $\tau$  the incubation time for crystallization. The constants  $K$  and  $n$  define the kinetics underlying the transformation process. Commonly  $K$  is called the growth constant and is a function of the nucleation rate  $\dot{N}(T)$ , the crystal growth

rate  $\dot{G}(T)$  and the geometry of the formed crystals. The constant  $n$  is often found to be a measure of the dimensionality of the phase-growth process, but it is also system specific. This fact makes a clear theoretical description difficult. For bulk metallic glasses values for the exponent  $n$  ranging from 2 to 3 are found for crystallization from the supercooled liquid state [113].

### Activation energy

For the analysis of the activation energy the low temperature isothermal dilatometric measurement was complemented with higher temperature constant heating rate DSC measurements. For the analysis of the non-isothermal DSC data a Kissinger model was used [114, 115]

$$\frac{\beta}{T_m^2} = \frac{A \cdot k_B}{E_A} \cdot \exp\left(-\frac{E_A}{k_B T}\right), \quad (5.23)$$

where  $\beta$  is the heating rate,  $T_m$  is the peak temperature of crystallization at heating rate  $\beta$ ,  $A$  is a constant,  $E_A$  is the activation energy of the process and  $k_B$  denotes Boltzmann's constant. The form of Eq. 5.23 was chosen because the constant  $A$  in the pre-exponential factor is in this case the same as in an isothermal measurement. Therefore, plotting the results in an isothermal representation is possible by a simple multiplication of the right side of Eq. 5.23 with  $\frac{E_A}{k_B}$ .

### Measurement results

According to the results in Sec. 5.2 where it was shown that the glass transition temperature on long time scales is much lower than obtained with heating rates in the order of several K/min, the temperature for the crystallization study was also chosen significantly lower than the lowest DSC determined  $T_g$ . The glass used was an un-equilibrated Vit105 sample from the same production batch as already used for the kinetic measurements in this work. For the crystallization temperature a value of 648 K was chosen because of timescale estimations according to extrapolations from literature data [116]. The estimation was based on the assumption of a maximum measurement time of  $2 \cdot 10^6$  s. As discussed earlier the modulation amplitude of the sample temperature for measuring the instantaneous expansion coefficient was set to 1 K. The measurement result for the sample length together with its time derivative is shown in Fig. 5.40. Due to the ordinate scaling the modulation for  $\bar{\alpha}$  is not visible. A magnified excerpt of this measurement curve was already shown in Fig. 5.39.

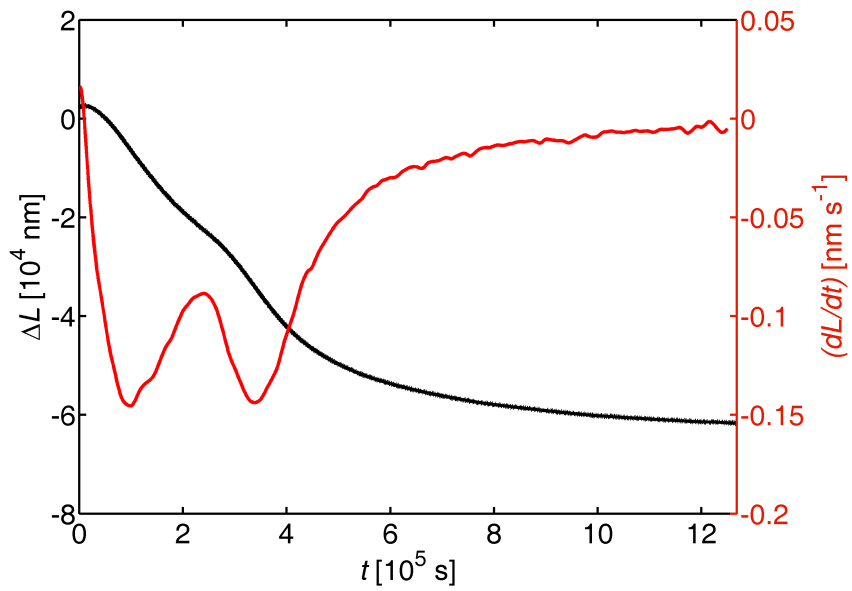


**Figure 5.40:** Length change signal of the un-equilibrated Vit105 sample at 648 K (black, at a temperature 11 K below  $T_g^{\text{calor}}$ ). The derivative  $\frac{dL}{dt}$  (red) can be used to distinguish between different length change process regimes. The length change modulation in  $\Delta L$  is not visible at this ordinate scaling.

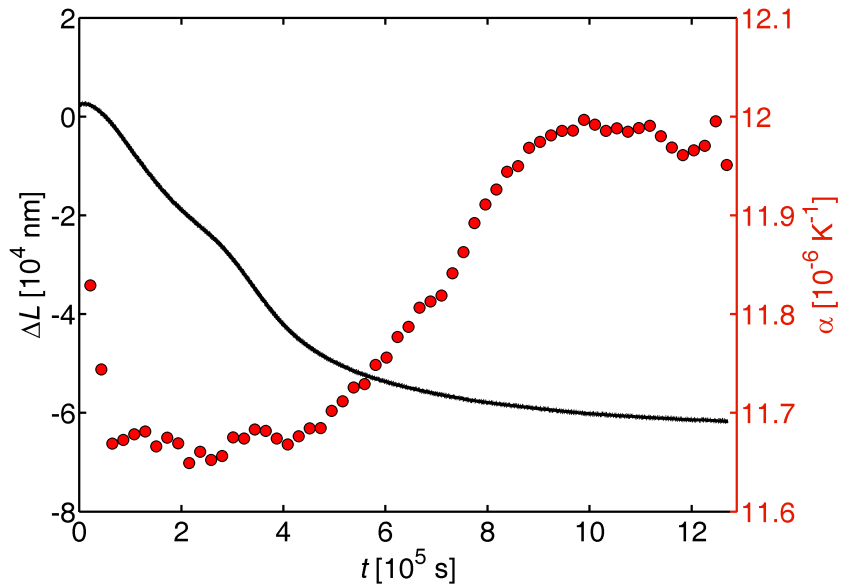


**Figure 5.41:** Length change signal of the un-equilibrated Vit105 sample at 648 K (black) together with the calculated values of the thermal expansion coefficient  $\bar{\alpha}$  (red dots). This representation clearly shows a phase change process starting after approx.  $4 \cdot 10^5$  s. The total measurement time of  $1.3 \cdot 10^6$  s corresponds to 15 days.

**Table 5.6:** The constants derived by fitting Eq. 5.24 to the data in Fig. 5.42.  $\alpha_1$  and  $\alpha_2$  are the thermal expansion coefficients of phase 1 and 2 respectively,  $K$  is the growth constant,  $n$  the Avrami exponent and  $\tau$  the incubation time for crystallization.

$\alpha_1$ [10 <sup>-6</sup> K <sup>-1</sup> ]	$\alpha_2$ [10 <sup>-6</sup> K <sup>-1</sup> ]	$K$ [s <sup>-1</sup> ]	$n$	$\tau$ [s]
(11.67 ± 0.01)	(11.99 ± 0.01)	(3.04 ± 0.5) · 10 <sup>-6</sup>	(2.0 ± 0.4)	(4.1 ± 0.3) · 10 <sup>5</sup>

Different regimes can be distinguished in the isothermal length change signal. At first a small expansion superimposed with the large volume reduction as a consequence of the un-equilibrated state of the material is observed. The expansion is a result of previous holding times at 583 and 633 K for testing the temperature modulation procedure. It is interesting to see that the reversible mechanism found in section 5.1.3 can also be observed in an as-received sample after short sub  $T_g$  annealing times. Until approx.  $2.5 \cdot 10^5$  s a large length reduction of about 25  $\mu\text{m}$  ( $\frac{\Delta L}{L_0} = 1.25 \cdot 10^{-3}$ ) is measured. This is a typical value found for the annealing out of irreversible quenched in volume (for comparison see e.g. [9]). Starting at a time of about  $2.5 \cdot 10^5$  s and clearly marked by a peak in the derivative a second length reducing process starts. This process governs the length change for the rest of the measurement. Although the derivation of the length change signal can help to distinguish different regimes it cannot answer the question if a length change is caused by defect equilibration or by a phase transformation. At this point the additional information gained by the simultaneous measurement of  $\bar{\alpha}$  can clarify exactly this question. In Fig. 5.41 the thermal expansion coefficient is plotted on the right ordinate. Each value was calculated by taking the mean length change over 72 temperature modulation steps. After a first relaxation phase the expansion coefficient reaches its equilibrium value  $\alpha_1$  after about  $5 \cdot 10^4$  s. No significant changes can be observed during the first volume reducing stage, which proofs that this process is not a phase transformation. In contrast to this the second stage of length reduction is clearly accompanied by a steady change in  $\bar{\alpha}$ . After approximately  $10 \cdot 10^5$  s a stationary value  $\alpha_2$  is again established. The measurement clearly shows the unambiguous relation between the phase fractions  $X_1$  and  $X_2$  and the expansion coefficient as defined by Eq. 5.19.

### JMAK - analysis

As a next step the variation of the thermal expansion coefficient  $\bar{\alpha}$  was analyzed in terms of the JMAK model described above. As the phase fractions of glass and crystal are

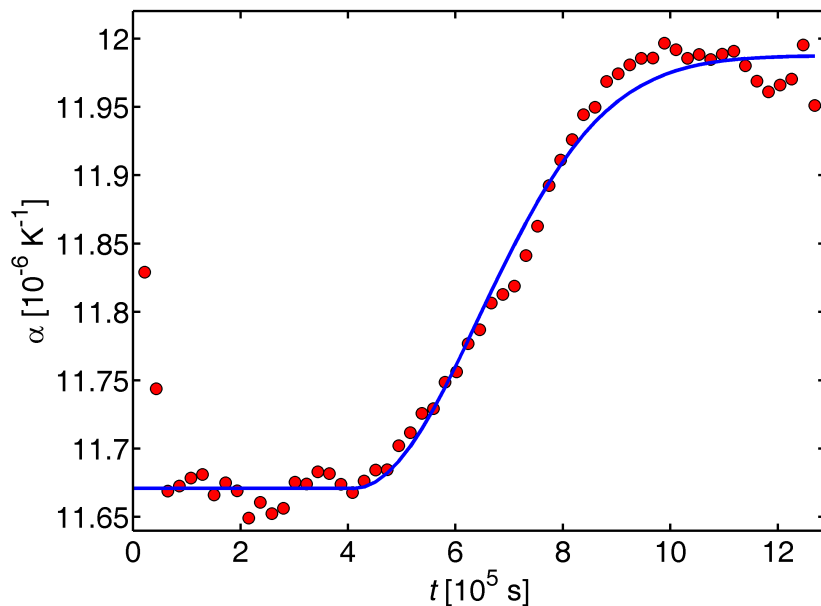


**Figure 5.42:** The thermal expansion coefficient fitted with the JMAK model defined by Eq. 5.24. The derived kinetic constants are summarized in Tab. 5.6.

directly related to  $\alpha_1$  and  $\alpha_2$  no calculations are necessary prior to the fitting procedure. Only the constants  $A$  and  $B$  in Eq. 5.23 had to be adapted appropriately

$$\bar{\alpha}(t) = (\alpha_2 - \alpha_1) \cdot (1 - \exp(-(\text{K} \cdot (t - \tau))^n)) + \alpha_1. \quad (5.24)$$

Adapted in this way the model function directly delivers the values of interest for  $K$ ,  $n$  and  $\tau$ . In Fig. 5.42 the data for the expansion coefficient fitted with the model function 5.24 is shown. The agreement of the data with the JMAK model is very good, especially with respect to the timescale of the process. The derived values are summarized in Tab. 5.6.

### DSC measurements

For a kinetic analysis in terms of activation energy for crystallization higher temperature measurements were made using a conventional DSC. In Fig. 5.43 the traces for 5, 10 and 20 K/min heating rates are shown. The main crystallization peaks used for the Kissinger analysis are marked with circles. By applying Eq. 5.23 to the data the following values were derived:

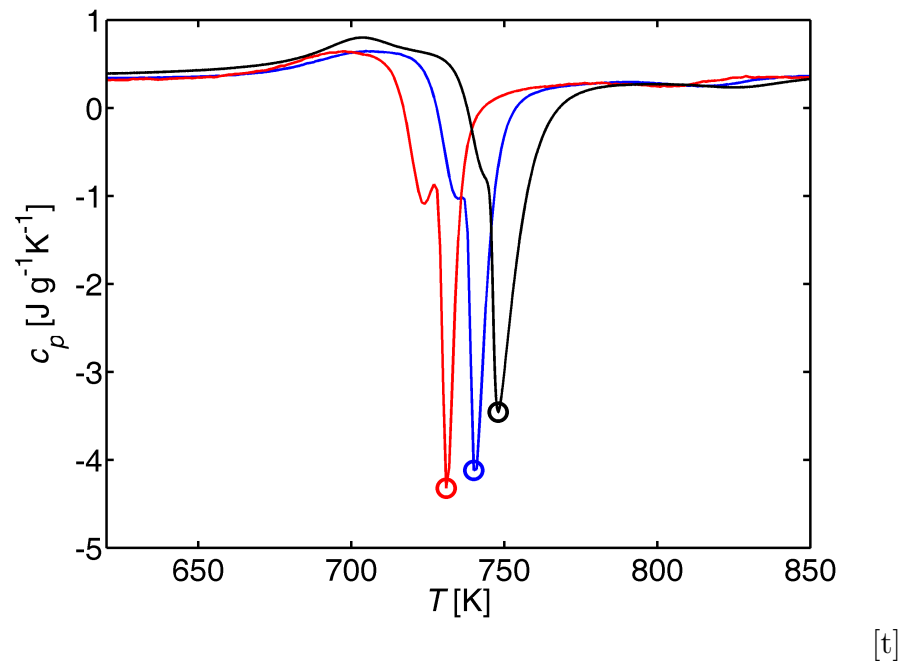


**Figure 5.43:** DSC measurements for Vit105 for 5 (red curve), 10 (blue curve) and 20 (black curve) K/min. The main crystallization event is marked by the circles. A second phase formation is observed in the low temperature shoulder of the crystallization peak. Both processes were analyzed in terms of the Kissinger model [114]. The values, converted to an isothermal representation together with the dilatometric result are shown in Fig. 5.44.

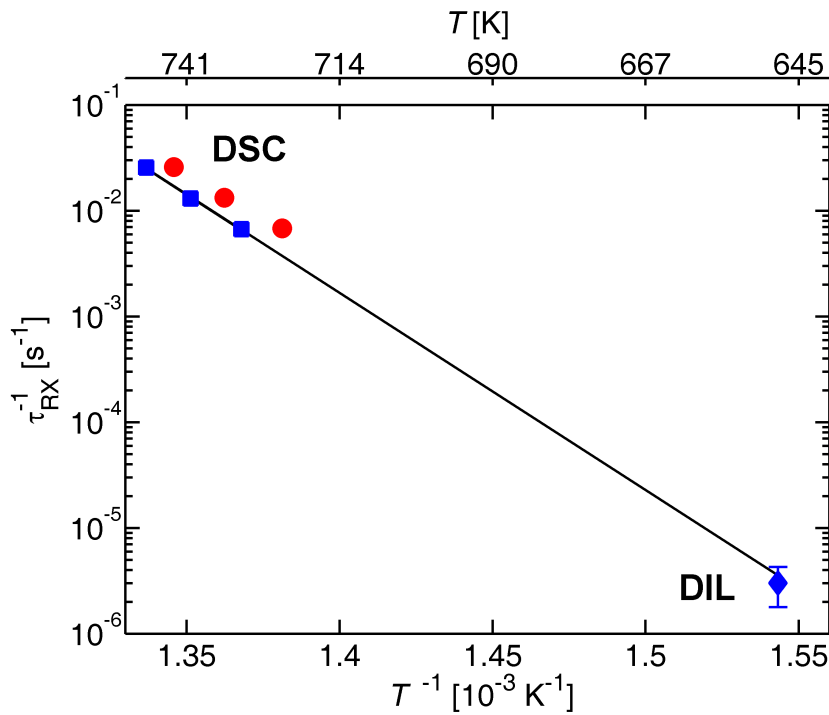


**Figure 5.44:** Arrhenius plot of the inverse incubation times for crystallization from conventional DSC measurement together with the value from the JMAK – analysis of the novel dilatometric technique. Two processes are found in the DSC measurements the second smaller process is indicated by the red circles. The low temperature dilatometric results shows excellent agreement with the DSC results extrapolated to low temperatures for the main crystallization peak.

$$E_A = (3.7 \pm 0.1) \text{ eV}$$

$$A = 2.15 \cdot 10^{23} \text{ s}^{-1}$$

The second crystallization event, visible in each measurement in Fig. 5.43 as a low temperature shoulder in the main crystallization peak, was also analyzed. The values read:

$$E_A = (3.3 \pm 0.1) \text{ eV}$$

$$A = 2.52 \cdot 10^{20} \text{ s}^{-1}$$

In Fig. 5.44 an Arrhenius plot of the DSC values together with the dilatometrically determined low temperature value from Tab. 5.6 is shown. The agreement of the DSC data with the value obtained by laser-dilatometry is excellent, although the difference in time constants spans nearly 4 orders of magnitude.

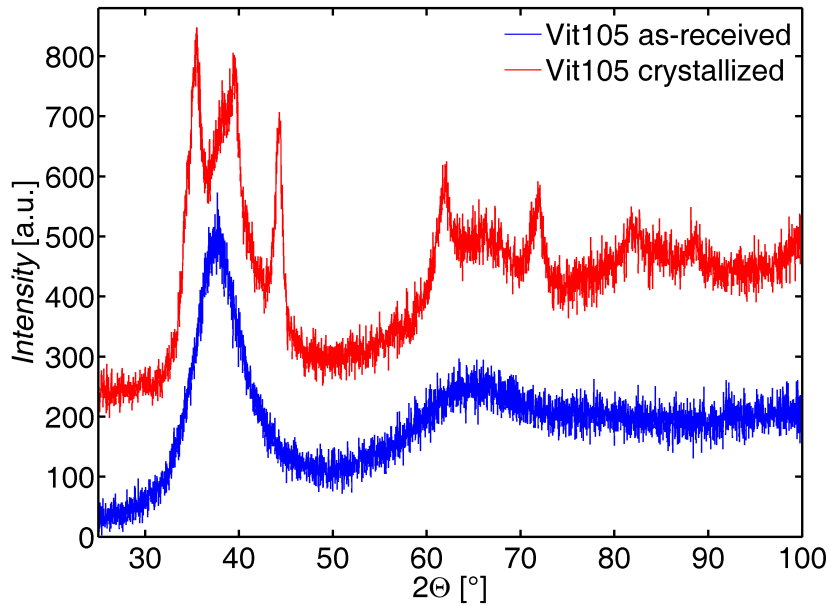


**Figure 5.45:** X-ray diffraction patterns of the Vit105 sample in the as-received and the fully crystalline state. The pattern for the crystalline material is offset for clarity.

### X-ray diffraction

X-ray diffraction patterns were measured in the as-received state and after the dilatometric measurements. In Fig. 5.45 the results are shown. The crystalline pattern is in good agreement with results from a crystallization study on Vit105 in Ref. 117. According to this publication the pattern corresponds to the fully crystalline state of the material.

### TTT - diagram

Another important aspect of the newly developed method for measuring phase transformations is the extension of available TTT diagrams to very long times and sub calorimetric  $T_g$  temperatures. In Fig. 5.46 TTT curves available for the alloys Vit106 ( $\text{Zr}_{57}\text{Cu}_{15.4}\text{Ni}_{12.6}\text{Al}_{10}\text{Nb}_5$  green triangles), Vit105 ( $\text{Zr}_{52.5}\text{Ti}_5\text{Cu}_{17.9}\text{Ni}_{14.6}\text{Al}_{10}$  blue squares) and Vit1 ( $\text{Zr}_{41.2}\text{Ti}_{13.8}\text{Cu}_{12.5}\text{Ni}_{10}\text{Be}_{22.5}$  red circles) are shown. Data is taken from Ref. 116. The Vit105 data in the plot is extended with the crystallization onset time derived with the JMAK - analysis in this work (marked by the arrow). The fits are not based on a physical model but should capture the appearance of the characteristic crystallization "noses" as good as possible.

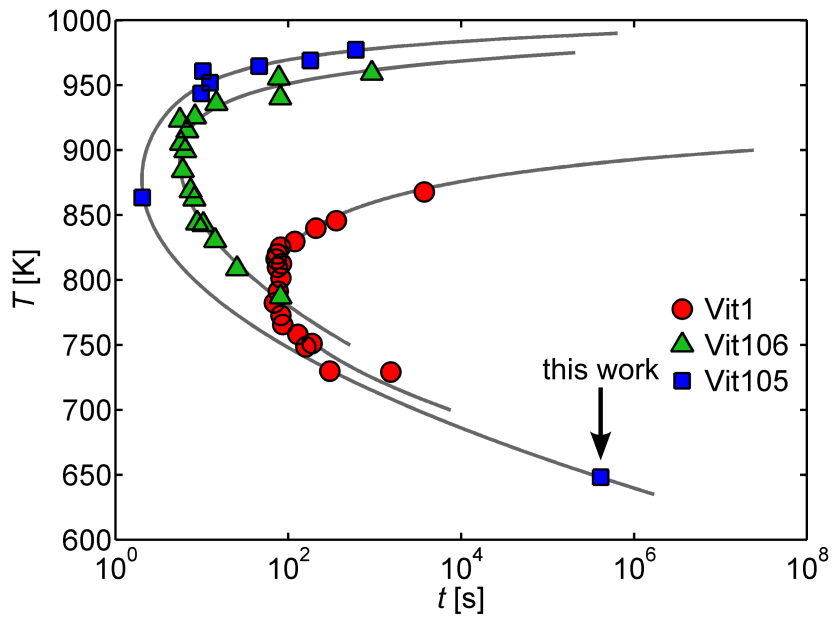


**Figure 5.46:** TTT-diagram for three different bulk metallic glasses. The data points for Vit105 extended with the result from the dilatometric measurement. The data points are taken from Ref. 116.

## Discussion

In this section a new method for measuring and detecting phase transformations with a dilatometric device was presented. By simultaneously measuring the thermal expansion coefficient and the length change of the material under quasi-isothermal conditions it was possible to distinguish between phase transformation and phase equilibration processes simultaneously in one single measurement. Furthermore, the time and temperature range for measuring crystallization in a bulk metallic glass was extended by two orders of magnitude, due to the high resolution and sensitivity of the laser-dilatometer. Additionally to the time for crystallization also the kinetics of the crystallization processes were studied in terms of a JMAK-model. The derived values in Tab. 5.6 are in well agreement with extrapolated literature data [113]. Especially the anomalously small Avrami exponent is commonly found in metallic glass forming systems [118]. This is possibly attributed to the very high viscosities of the supercooled liquids of metallic systems in the vicinity of the glass transition temperature. The second crystallization process found in DSC measurements was not visible in the dilatometric results. To clarify this observation additional measurements especially microscopic phase characterizations would be necessary.

The new method is not limited to crystallization processes from supercooled liquids.

In fact it is applicable to every phase transformation process in condensed matter for which Eq. 5.19 holds. This is expectable for all sorts of diffusive and non-diffusive phase transitions.



---

## 6 Summary and Conclusion

---

In this work the method of high resolution laser-dilatometry was further developed and applied to study kinetic phenomena in bulk metallic glasses. The method proved to be a significant extension of the available measurement techniques for the investigations of kinetic processes in materials in general. With a newly developed specimen holder, furnace assembly and temperature control it was possible to extend the absolute length change resolution to the sub-100nm regime for long-time measurements. Time-scales larger than  $10^6$  s are readily accessible in the experiments without noticeable drifts in the measurement signal. With this new experimental technique it was for the first time possible to investigate reversible specific volume changes in equilibrated bulk metallic glasses far below their calorimetrically determined glass transition temperature [119]. By applying a sophisticated mathematical model to the measured volume equilibration curves insights into the specific time constants of equilibration and the underlying activation energies were gained. The following conclusions can be drawn:

- The reversible equilibration process in the glassy state, which was found for both investigated glass alloys shows a distinct non-exponential time-dependence. The non-exponential equilibration curves were best fitted with a stretched exponential equilibration function with a temperature dependent stretching parameter  $\beta(T)$ . With the mathematical model developed in Sec. 2.3 it was possible to deduce a characteristic time constant distribution from the parameters of the stretched exponential function.
- In the investigated temperature regime the time-temperature variation of an effective time constant, deduced from the probability distributions, can be described by an Arrhenius behaviour. Activation energies for atomic motion of  $(3.2 \pm 0.1)$  eV

---

and of  $(3.1 \pm 0.1)$  eV are deduced for the  $\text{Zr}_{56}\text{Al}_7\text{Cu}_{24}\text{Ni}_{10}\text{Co}_3$  glass (Sec. 5.1.1) and for the  $\text{Zr}_{52.5}\text{Ti}_5\text{Cu}_{17.9}\text{Ni}_{14.6}\text{Al}_{10}$  glass (Sec. 5.1.3), respectively.

- A good agreement of the measured activation energies for volume migration with available activation energy values for diffusion as obtained from tracer diffusion measurements is found. The correlation suggests that the formation of specific volume in the bulk metallic glass comprises a very low or even vanishing formation enthalpy. This insight fits very well to the classical free-volume theory were free volume forms solely due to the thermal expansion of the glassy matrix [120].
- There is no correlation between the reversible volume equilibration process found in the sub- $T_g$  temperature regime and the primary liquid relaxation time  $\tau_\alpha$  found in dynamic mechanical analysis (DMA) experiments. This result suggests that the process observed in the dilatometric experiments is less collective in terms of atomic motion and shows a weaker temperature dependence than the primary  $\alpha$ -relaxation as determined from the DMA experiments in Sec. 5.1.2.

To probe the equilibrium specific volume concentration and evolution in a long-time equilibrated bulk metallic glass, the volume change upon heating was measured with a self-developed measurement technique which provides effective heating rates in the order of  $10^{-2}$  K/min (Chap. 5.2). By changing the sample temperature in steps of 5 K with subsequent isothermal equilibration phases a distinct change in the specific volume evolution behaviour of the bulk metallic glass  $\text{Zr}_{52.5}\text{Ti}_5\text{Cu}_{17.9}\text{Ni}_{14.6}\text{Al}_{10}$  was found at approximately 628 K which is 30 K below the calorimetrically determined glass transition temperature at a heating rate of 5 K/min. Additionally, the evolution of the thermal expansion coefficient of the material could be calculated from the 5 K temperature steps. The following interpretations of the results are possible:

- The observed change in the specific volume evolution at 628 K corresponds to the glass transition temperature  $T_g$  in the equilibrated state of this glass alloy
- With a volume sensitivity of  $\frac{\Delta V}{V} = 10^{-6}$  no irreversible annealing out of volume was detectable on a timescale exceeding  $10^5$  s. Thus the glass was in the fully equilibrated state.
- The observation strongly supports theoretical predictions for the existence of an ideal glass transition in the equilibrium state. Most probably this transition was observed for this bulk metallic glass at 628 K [119].

To assess the local atomic volume kinetics in  $\text{Zr}_{52.5}\text{Ti}_5\text{Cu}_{17.9}\text{Ni}_{14.6}\text{Al}_{10}$  extensive positron annihilation measurements at the NEPOMUC beam-line of FRM II (TU-München, Garching) were conducted. Conventional as well as coincident Doppler broadening experiments were made to get information about possible correlations between the macroscopic and microscopic volume equilibration behaviour of bulk metallic glasses. The results allowed for the following conclusions:

- No localized volume formation was detectable in the time variation of the conventional S-parameter. Thus, the volume formation process in bulk metallic glasses is most likely a delocalized phenomenon. This result underlines the observation made in the dilatometry experiments that free-volume formation in this system is not an activated process.
- The coincident Doppler broadening experiments suggest that no change in the chemical environment surrounding the positron annihilation site occurs. Thus, it can be concluded that the local atomic structure of the investigated samples does not change during the thermal treatment.

To complete the range of investigated phenomena, the low-temperature crystallization kinetics of the glass alloy  $\text{Zr}_{52.5}\text{Ti}_5\text{Cu}_{17.9}\text{Ni}_{14.6}\text{Al}_{10}$  was investigated by a self-developed, in-situ measurement technique based on cyclic temperature modulations in an isothermal measurement (Chap. 5.4). The kinetics was analysed in terms of their activation energy by comparing them with a Kissinger analysis from high temperature DSC measurements. The nucleation and growth properties of the glass were analysed by applying a Johnson-Mehl-Avrami-Kolmogorov (JMAK) model to the data. The crystallization behaviour comprises the following points:

- By the direct phase transformation measurement method a crystallization process with an incubation time of  $4 \cdot 10^5$  s (4.6 days) and a total time of approximately  $1.2 \cdot 10^6$  s (14 days) was measurable. The data fits very well to available time-temperature-transformation (TTT) data for  $\text{Zr}_{52.5}\text{Ti}_5\text{Cu}_{17.9}\text{Ni}_{14.6}\text{Al}_{10}$ .
- The range of TTT-diagrams for bulk metallic glasses was extended by two orders of magnitude. The asymmetric shape of the diagrams often found for bulk metallic glasses was confirmed.
- The Arrhenius-diagram for the activation energy of crystallization was extended by more than three orders of magnitude in terms of the inverse time constant for crystallization.

---

Beside glass measurements, the laser-dilatometer proved to be a reliable tool for the investigation of experiments with small-signals and long measurement times. Especially the newly developed method for isothermally measuring the thermal expansion coefficient of a material, allows for a distinction between phase transformation and phase equilibration processes in the same measurement. In the past such measurements were only possible by using at least one additional measurement technique. Considering these advantages the laser-dilatometer indeed represents a significant extension to the available measurement techniques for solid materials.

---

# Bibliography

---

- [1] A. Inoue, T. Zhang, and T. Masumoto, Materials Transactions, JIM **31**, 177 (1990).
- [2] A. Peker and W. L. Johnson, Applied Physics Letters **63**, 2342 (1993).
- [3] P. Wolynes and V. Lubchenko, *Structural Glasses and Supercooled Liquids: Theory, Experiment, and Applications* (Wiley, 2012).
- [4] L. Berthier and G. Biroli, Review of Modern Physics **83**, 587 (2011).
- [5] K. Binder and W. Kob, *Glassy Materials and Disordered Solids: An Introduction to Their Statistical Mechanics* (World Scientific, 2011).
- [6] I. Gallino, M. B. Shah, and R. Busch, Journal of Alloys and Compounds **434 - 435**, 141 (2007).
- [7] J. Mei, J. Soubeyroux, J. Blandin, J. Li, H. Kou, H. Fu, and L. Zhou, Journal of Non-Crystalline Solids **357**, 110 (2011).
- [8] Y. Zhang and H. Hahn, Journal of Non-Crystalline Solids **355**, 2616 (2009).
- [9] Z. Evenson and R. Busch, Journal of Alloys and Compounds **509**, 38 (2011).
- [10] N. Mattern, U. Kühn, H. Hermann, S. Roth, H. Vinzelberg, and J. Eckert, Materials Science and Engineering: A **375 - 377**, 351 (2004).
- [11] A. Karamanov, B. Dzhantov, M. Paganelli, and D. Sighinolfi, Thermochimica Acta **553**, 1 (2013).

- [12] J. Hachenberg, D. Bedorf, K. Samwer, R. Richert, A. Kahl, M. D. Demetriou, and W. L. Johnson, *Applied Physics Letters* **92**, 131911 (2008).
- [13] Z. F. Zhao, P. Wen, W. H. Wang, and C. H. Shek, *Applied Physics Letters* **89**, 071920 (2006).
- [14] Q. Wang, J. Pelletier, J. Blandin, and M. Suery, *Journal of Non-Crystalline Solids* **351**, 2224 (2005).
- [15] W. Kob and L. Berthier, *Physical Review Letters* **110**, 245702 (2013).
- [16] V. Lubchenko and P. G. Wolynes, *Annual Review of Physical Chemistry* **58**, 235 (2007).
- [17] C. A. Angell, K. L. Ngai, G. B. McKenna, P. F. McMillan, and S. W. Martin, *Journal of Applied Physics* **88**, 3113 (2000).
- [18] C. Suryanarayana and A. Inoue, *Bulk Metallic Glasses* (Taylor & Francis, 2011).
- [19] J. Jensen and A. Mackintosh, *Rare earth magnetism: structures and excitations*, International series of monographs on physics (Clarendon Press, 1991).
- [20] R. Balluffi, S. Allen, and W. Carter, *Kinetics of Materials* (Wiley, 2005).
- [21] F. Ye, W. Sprengel, R. K. Wunderlich, H.-J. Fecht, and H.-E. Schaefer, *Proceedings of the National Academy of Sciences* **104**, 12962 (2007).
- [22] X. Xia and P. G. Wolynes, *Physical Review Letters* **86**, 5526 (2001).
- [23] C. M. Roland, D. Fragiadakis, D. Coslovich, S. Capaccioli, and K. L. Ngai, *The Journal of Chemical Physics* **133**, 124507 (2010).
- [24] V. Lubchenko and P. G. Wolynes, *The Journal of Chemical Physics* **121**, 2852 (2004).
- [25] R. Kohlrausch, *Annalen der Physik* (Leipzig) **91**, 179 (1854).
- [26] G. Williams and D. C. Watts, *Transactions of the Faraday Society* **66**, 80 (1970).
- [27] M. Berberan-Santos, E. Bodunov, and B. Valeur, *Annalen der Physik* (Berlin) **17**, 460 (2008).
- [28] M. Berberan-Santos, E. Bodunov, and B. Valeur, *Chemical Physics* **315**, 171 (2005).

- [29] C. P. Lindsey and G. D. Patterson, *The Journal of Chemical Physics* **73**, 3348 (1980).
- [30] D. C. Johnston, *Physical Review B* **74**, 184430 (2006).
- [31] D. C. Johnston, S.-H. Baek, X. Zong, F. Borsa, J. Schmalian, and S. Kondo, *Physical Review Letters* **95**, 176408 (2005).
- [32] F. G. Coury, L. C. R. Aliaga, C. R. M. Afonso, C. Bolfarini, W. J. B. Filho, and C. S. Kiminami, *Journal of Materials Research and Technology* **2**, 125 (2013).
- [33] R. M. Srivastava, J. Eckert, W. Loser, B. K. Dhindaw, and L. Schultz, *Materials Transactions, JIM* **43**, 1670 (2002).
- [34] C. Hugenschmidt, H. Ceeh, T. Gigl, F. Lippert, C. Piochacz, P. Pikart, M. Reiner, J. Weber, and S. Zimnik, *Journal of Physics: Conference Series* **443**, 012079 (2013).
- [35] B. Oberdorfer, E.-M. Steyskal, W. Sprengel, W. Puff, P. Pikart, C. Hugenschmidt, M. Zehetbauer, R. Pippal, and R. Würschum, *Physical Review Letters* **105**, 146101 (2010).
- [36] C. Hugenschmidt, G. Dollinger, W. Egger, G. Kögel, B. Löwe, J. Mayer, P. Pikart, C. Piochacz, R. Repper, K. Schreckenbach, et al., *Applied Surface Science* **255**, 29 (2008).
- [37] C. Hugenschmidt, G. Kögel, R. Repper, K. Schreckenbach, P. Sperr, B. Straßer, and W. Triftshäuser, *Nuclear Instruments and Methods in Physics Research Section B: Beam Interactions with Materials and Atoms* **221**, 160 (2004).
- [38] H.-E. Schaefer, K. Frenner, and R. Würschum, *Physical Review Letters* **82**, 948 (1999).
- [39] K. Frenner, Master's thesis, Universitaet Stuttgart (1999).
- [40] F. Baier, Ph.D. thesis, Universitaet Stuttgart (2002).
- [41] B. Lorenzoni, Master's thesis, TU Graz (2010).
- [42] M. Luckabauer, Master's thesis, TU Graz (2010).
- [43] R. Würschum, C. Grupp, and H.-E. Schaefer, *Physical Review Letters* **75**, 97 (1995).

- [44] G. Paperin, *Live Graph*: <http://www.live-graph.org>, Free Software (2009), URL <http://www.live-graph.org/>.
- [45] H. Mehrer, M. Luckabauer, and W. Sprengel, Defect and Diffusion Forum **333**, 1 (2013).
- [46] R. Cahn, A. Evans, and M. McLean, eds., *High-temperature structural materials*, Philosophical Transactions of the Royal Society of London. v.351 (Chapman & Hall for the Royal Society, 1996).
- [47] N. Stoloff and V. Sikka, eds., *Physical Metallurgy and Processing of Intermetallic Compounds* (Springer London, Limited, 2011).
- [48] C. Koch, ed., *High-temperature ordered intermetallic alloys VII*, Materials Research Society Symposia Proceedings (Materials Research Society, 1997).
- [49] E. George, M. Mills, and M. Yamaguchi, eds., *High-temperature ordered intermetallic alloys VIII*, Materials Research Society Symposia Proceedings (Materials Research Society, 1999).
- [50] S. Deevi and V. Sikka, *Intermetallics* **4**, 357 (1996).
- [51] S.-C. Deevi, V.-K. Sikka, and C.-T. Liu, *Progress in Materials Science* **42**, 177 (1997).
- [52] M. Palm, A. Schneider, F. Stein, and G. Sauthoff, *MRS Proceedings* **842** (2004).
- [53] K. Momma and F. Izumi, *Journal of Applied Crystallography* **41**, 653 (2008).
- [54] H. Mehrer, *Diffusion in Solids: Fundamentals, Methods, Materials, Diffusion-Controlled Processes* (Springer, 2007).
- [55] M. Fähnle, J. Mayer, and B. Meyer, *Intermetallics* **7**, 315 (1999).
- [56] H. Mehrer, M. Eggersmann, A. Gude, M. Salamon, and B. Sepiol, *Materials Science and Engineering: A* **239-240**, 889 (1997).
- [57] O. Kubaschewski, *Iron-binary phase diagrams* (Springer-Verlag, 1982).
- [58] R. Kerl, J. Wolff, and T. Hehenkamp, *Intermetallics* **7**, 301 (1999).
- [59] M. Morris, O. George, and D. Morris, *Materials Science and Engineering: A* **258**, 99 (1998).
- [60] H. Bakker, I. Modder, and M. Kuin, *Intermetallics* **5**, 535 (1997).

- [61] A.-P. Tsai, D. Kawase, A. Inoue, and T. Masumoto, *Scripta Metallurgica et Materialia* **29**, 657 (1993).
- [62] A. Inoue, T. Zhang, N. Nishiyama, K. Ohba, and T. Masumoto, *Materials Transactions, JIM* **34**, 1234 (1993).
- [63] A. Inoue, N. Nishiyama, K. Amiya, T. Zhang, and T. Masumoto, *Materials Letters* **19**, 131 (1994).
- [64] T. Zhang, A. Inoue, and T. Masumoto, *Materials Science and Engineering: A* **181-182**, 1423 (1994).
- [65] C. Tang and P. Harrowell, *Nature Materials* **12**, 507 (2013).
- [66] K. F. Kelton, *Nature Materials* **12**, 473 (2013).
- [67] J. Heinrich, R. Busch, F. Müller, S. Grandthyll, and S. Häfner, *Applied Physics Letters* **100**, 071909 (2012).
- [68] G. J. Fan, M. Freels, H. Choo, P. K. Liaw, J. J. Z. Li, W.-K. Rhim, W. L. Johnson, P. Yu, and W. H. Wang, *Applied Physics Letters* **89**, 241917 (2006).
- [69] Y. S. A. Inoue, Y. Yokoyama and T. Masumoto, *Materials Transactions, JIM* **35**, 923 (1994).
- [70] Y. Kawamura, T. Shibata, A. Inoue, and T. Masumoto, *Acta Materialia* **46**, 253 (1998).
- [71] A. Inoue, T. Zhang, and T. Masumoto, *Materials Transactions, JIM* **36**, 391 (1995).
- [72] Y. Kawamura, T. Shibata, A. Inoue, and T. Masumoto, *Applied Physics Letters* **69**, 1208 (1996).
- [73] A. Caron, R. Wunderlich, D. Louzguine, T. Egami, and H. Fecht, *Philosophical magazine letters* **91**, 751 (2011).
- [74] A. Caron, R. Wunderlich, L. Gu, and H.-J. Fecht, *Scripta Materialia* **64**, 946 (2011).
- [75] R. Wunderlich, M. Vaillant, A. Caron, and H. Fecht, *Advanced Engineering Materials* **10**, 1020 (2008).
- [76] R. Kronig, *Journal of the Optical Society of America* **12**, 547 (1926).

- [77] Wen, Ping and Zhao, Zuo Feng and Pan, Ming Xiang and Wang, Wei Hua, *Physica Status Solidi (a)* **207**, 2693 (2010).
- [78] P. Wen, D. Q. Zhao, M. X. Pan, W. H. Wang, Y. P. Huang, and M. L. Guo, *Applied Physics Letters* **84**, 2790 (2004).
- [79] Z. F. Zhao, P. Wen, C. H. Shek, and W. H. Wang, *Physical Review B* **75**, 174201 (2007).
- [80] Z. Wang, H. B. Yu, P. Wen, H. Y. Bai, and W. H. Wang, *Journal of Physics: Condensed Matter* **23**, 142202 (2011).
- [81] M. Hojo and H. Numakura, *Materials Science and Engineering: A* **442**, 268 (2006).
- [82] C. A. Angell, *Science* **267**, 1924 (1995).
- [83] R. Busch, W. Liu, and W. L. Johnson, *Journal of Applied Physics* **83**, 4134 (1998).
- [84] E. Bakke, R. Busch, and W. L. Johnson, *Applied Physics Letters* **67**, 3260 (1995).
- [85] I. Gallino, J. Schroers, and R. Busch, *Journal of Applied Physics* **108**, 063501 (2010).
- [86] R. Busch, E. Bakke, and W. Johnson, *Acta Materialia* **46**, 4725 (1998).
- [87] L. Shadowspeaker and R. Busch, *Applied Physics Letters* **85**, 2508 (2004).
- [88] A. Bains, C. Gordon, A. Granato, and R. Schwarz, *Journal of Alloys and Compounds* **310**, 20 (2000).
- [89] W. L. Johnson, M. D. Demetriou, J. S. Harmon, M. L. Lind, and K. Samwer, *MRS Bulletin* **32**, 644 (2007).
- [90] M. Jiang and L. Dai, *Physical Review B* **76**, 054204 (2007).
- [91] X. H. Lin and W. L. Johnson, *Journal of Applied Physics* **78**, 6514 (1995).
- [92] G. Fan, J. Löffler, R. Wunderlich, and H.-J. Fecht, *Acta Materialia* **52**, 667 (2004).
- [93] C. C. Hays, J. Schroers, W. L. Johnson, T. J. Rathz, R. W. Hyers, J. R. Rogers, and M. B. Robinson, *Applied Physics Letters* **79**, 1605 (2001).

- [94] F. Faupel, W. Frank, M.-P. Macht, H. Mehrer, V. Naundorf, K. Rätzke, H. R. Schober, S. K. Sharma, and H. Teichler, *Review of Modern Physics* **75**, 237 (2003).
- [95] T. Zumkley, V. Naundorf, M.-P. Macht, and G. Frohberg, *Scripta Materialia* **45**, 471 (2001).
- [96] P. Fielitz, M.-P. Macht, V. Naundorf, and G. Frohberg, *Journal of Non-Crystalline Solids* **250 - 252**, 674 (1999).
- [97] U. Geyer, W. L. Johnson, S. Schneider, Y. Qiu, T. A. Tombrello, and M.-P. Macht, *Applied Physics Letters* **69**, 2492 (1996).
- [98] K. Knorr, M.-P. Macht, K. Freitag, and H. Mehrer, *Journal of Non-Crystalline Solids* **250 - 252**, 669 (1999).
- [99] K. Knorr, M.-P. Macht, and H. Mehrer, *Materials Research Society Symposia Proceedings* **554**, 269 (1999).
- [100] H.Nakajima, T.Kojima, K.Nonaka, T.Zhang, A.Inoue, and N.Nishiyama, *Materials Research Society Symposia Proceedings* **644**, L2.2.1 (2001).
- [101] S. Flege, U. Fecher, and H. Hahn, *Journal of Non-Crystalline Solids* **270**, 123 (2000).
- [102] P. G. Debenedetti and F. H. Stillinger, *Nature* **410**, 259 (2001).
- [103] J. C. Qiao and J. M. Pelletier, *Journal of Applied Physics* **112**, 033518 (2012).
- [104] J. Qiao and J. Pelletier, *Intermetallics* **28**, 40 (2012).
- [105] Y. P. Mitrofanov, V. A. Khonik, A. V. Granato, D. M. Joncich, and S. V. Khonik, *Journal of Applied Physics* **109**, 073518 (2011).
- [106] Y. P. Mitrofanov, V. A. Khonik, A. V. Granato, D. M. Joncich, S. V. Khonik, and A. M. Khoviv, *Applied Physics Letters* **100**, 171901 (2012).
- [107] W. Kauzmann, *Chemical Reviews* **43**, 219 (1948).
- [108] J. Schroers, Y. Wu, R. Busch, and W. Johnson, *Acta Materialia* **49**, 2773 (2001).
- [109] D. V. Louzguine-Luzgin, *Journal of Alloys and Compounds* **586**, 216 (2014).
- [110] A. N. Kolmogorov, *Bulletin of the Academy of Sciences of the USSR* **3**, 355 (1937).

## Bibliography

---

- [111] W. A. Johnson and R. F. Mehl, Transactions of the American Institute of Mining, Metallurgical and Petroleum Engineers **135**, 416 (1939).
- [112] M. Avrami, Journal of Chemical Physics **7**, 212 (1940).
- [113] J. Qiao and J. Pelletier, Transactions of Nonferrous Metals Society of China **22**, 577 (2012).
- [114] H. E. Kissinger, Analytical Chemistry **29**, 1702 (1957).
- [115] P. Roura and J. Farjas, Journal of Materials Research **24**, 3095 (2009).
- [116] S. Mukherjee, Z. Zhou, J. Schroers, W. L. Johnson, and W. K. Rhim, Applied Physics Letters **84**, 5010 (2004).
- [117] F. Jiang, J. Qu, G. Fan, W. Jiang, D. Qiao, M. W. Freels, P. K. Liaw, and H. Choo, Advanced Engineering Materials **11**, 925 (2009).
- [118] T. Pradell, D. Crespo, N. Clavaguera, and M. T. Clavaguera-Mora, Journal of Physics: Condensed Matter **10**, 3833 (1998).
- [119] M. Luckabauer, U. Kühn, J. Eckert, and W. Sprengel, Physical Review B **89**, 174113 (2014).
- [120] M. H. Cohen and G. S. Grest, Physical Review B **20**, 1077 (1979).

---

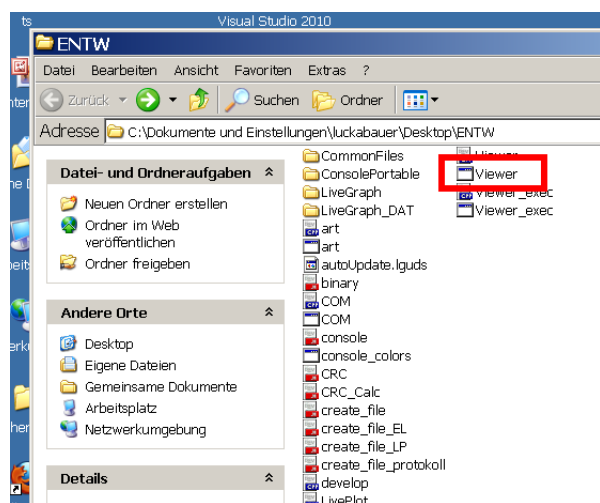
# A Dilatometer control software

---

The dilatometer control software is basically a command line based program with the JAVA extension LiveGraph for visualization purposes. LiveGraph is integrated into the software in such a way that no installation of JAVA on the target machine is necessary. The runtime environment is included as a portable version in the main folder of the software under **CommonFiles**. To transfer the control software to another PC or reinstall it after a software update, it is simply necessary to copy the main folder to the desired location and configure the COM-port setting in such a way that the communication with the interferometer and the controller can be established.

## Start of a measurement and configuration of COM ports

To start a measurement the application **Viewer.exe** in the main software folder must be launched. The folder should look like in the following picture:



---

After the program is executed the following command line window opens up:



In this case it states that the COM port 1 was successfully opened and set to the parameters in the picture. If the opening of the COM port would have failed, an error message would appear. It is important to set the COM port for communication with the EUROTHERM 3504 controller to the correct number because at this point only the existence of the COM port is checked. To change the COM number for communication with the controller the following procedure is necessary:

- At first open the file **modbus.h**, located in the main software folder in a text editor or in a programming environment
- When the file is open search for the following lines:

```
34 //----- Code needed by all functions -----//  
35  
36 unsigned short com_number = 1; // COM  
37 unsigned short baudrate = 19200; // 19200  
38 float fbaudrate = baudrate;  
39  
40 // calculate timeout min 3.5 chars  
41 float one_char_time_msec = 11000*(1/(fbaudrate)); // 11 bits for  
        // each byte in RTU mode  
42 float ftimeout = 1.5 * one_char_time_msec; //if a silent  
        // interval of more than 1.5 char times occurs --> timeout  
43 int interframetime = (int)ceil(3.5 * one_char_time_msec); //min 3.5 char  
        //times for interframetime  
44 int timeout = (int)ceil(ftimeout);  
45  
46 HANDLE com_handle = open_com_RTU(com_number,baudrate,8,'E',1,timeout); //  
        // Create the COM handle
```

- Change the variable **com\_number** to the desired value and save the change
- In the main folder open the file **Viewer.cpp** in a programming environment for C++ and compile the file to make the change active

When the COM-port for communication with the controller was successfully opened press **ENTER** to start the main program and the LiveGraph visualization environment. The following screen appears:



where the software tries to open the COM-ports for communication with the laser-interferometer. Because there are two independent evaluation units, also two COM-ports are needed for data transfer. The procedure to change the COM-port numbers is rather similar to the one described above for the controller. A change in the COM numbering can be necessary after a software or hardware change of the used PC. If an error occurs in the above shown screen stating that the COM port opening has failed the following steps are necessary:

- Locate the file **Viewer.cpp** in the main software folder and open it
- Search for the following lines:

```

126
127 //-----
128 HANDLE h_c1 = open_com(4,19200,8,'N',2); //open COM1 with BaudRate, ByteSize
      , Parity and Stopbits
129 HANDLE h_c2 = open_com(3,19200,8,'N',2); //open COM2 with BaudRate, ByteSize
      , Parity and Stopbits
130 //-----

```

- 
- The first integer number in the **open\_com** function represents the COM port number as set in the Windows control panel
  - Set the values to match the system settings and save the change
  - Compile **Viewer.cpp** and restart the software

When no errors occur the software starts the LiveGraph visualization and automatically starts to collect data. The configuration possibilities of the LiveGraph window are described in the following paragraph. The Command line software output when data is collected looks like this:

```

C:\Dokumente und Einstellungen\luckabauer\Desktop\ENTW\View...
# 80    ns: 81766          ns: 81813      time offset: 47 ms
< Smiling Face> N - 0 0 0 1 2 1 3 8 7 < Heart> -121387  < Smiling Face> N + 0 0 0 0 0 4 5 9 < Heart> 459 deltaL =
121846 nm

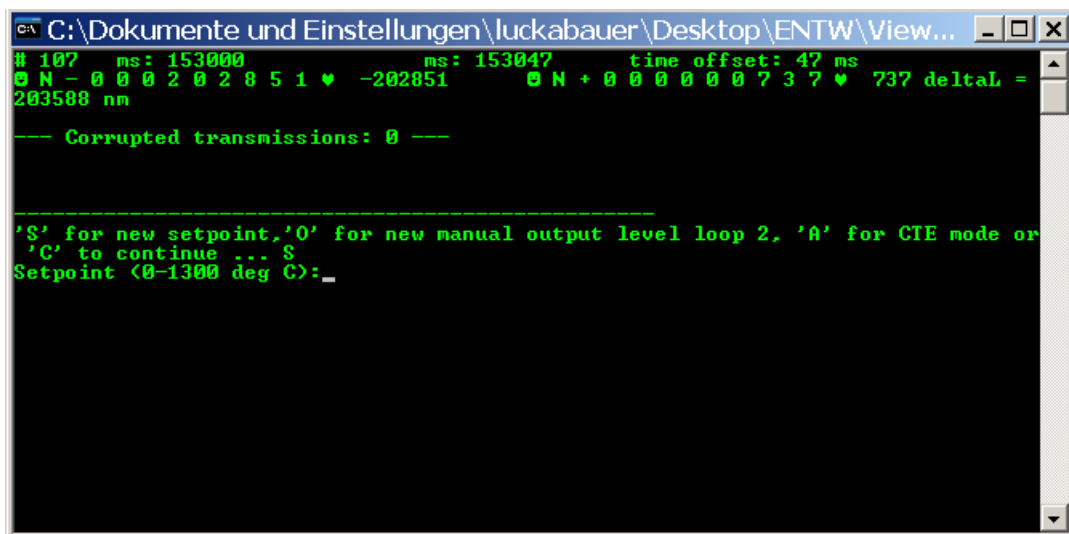
--- Corrupted transmissions: 0 ---

```

The output begins in the upper left corner with the dataset number followed by the data recording time for laser 1 and 2 in milliseconds. In the upper right corner the time offset between the two data transmissions is shown. Values lower than 400 ms can be considered as good. If the time-offset is larger than 1000 ms the data recording in the interferometer control unit is possibly asymmetric and needs a reset. If the offset persists after restarting the software please refer to the manual of the SIOS SP120 interferometer. The length value data transmissions visible in the above screen start with the STX (start of transmission; smiling face) byte followed by the operation mode, in this case N for length values in nm, a sign and a nine digit number for the actual value. The message frame is closed by the ETX (end of transmission; heart) byte. The length change deltaL is calculated from the two values of every data set. Because the interferometer transfer protocol does not include a redundancy or error check, all data frames are checked by the software for integrity. If one transmission does not fulfil the integrity criteria a one is added to the counter of corrupted transmissions.

## Changing measurement parameters

When the software is running it is possible to change the mode of operation as well as the measurement parameters at any time by simply interrupting the data recording. With **Shift + S**. The following screen appears:



The possible inputs have the following meanings:

- **'S' for new setpoint:** by pressing 'S' a new set point in degrees centigrade can be entered (This is shown in the picture above).
- **'O' for new manual ouptput level loop 2:** manually change the output level for the gradient control furnace between 0 and 100% by pressing 'O'. It is noteworthy that the real output level in [W] of the gradient control power supply is only adjustable directly by the controls on the front panel of the supply. These controls must be adjusted in such a way that 100% output power are well in the save operation range of the furnace.
- **'A' for CTE mode:** starts the modulation of the sample temperature to simultaneously measure the instantaneous thermal expansion coefficient of the material by pressing 'A'. Details about the measurement procedure can be found in Chap. 4 of this work.
- **'C' to continue:** the program continues with the active measurement.

---

## CTE mode

If CTE mode was chosen in the mode selection screen the command line window looks like this:



In the upper left corner **CTE mode on** indicates the mode of operation. The setpoint is shown together with its modulation amplitude CTE-Temperature-Interval. The period time of modulation is given by the CTE-Time-Interval and the number of intervals already recorded is given by the Alphainterval\_COUNT variable. Up to now the values for interval-time and interval-temperature are not changeable when the software is running. To change the values locate the following lines in the **Viewer.cpp** file (located in the main folder of the software):

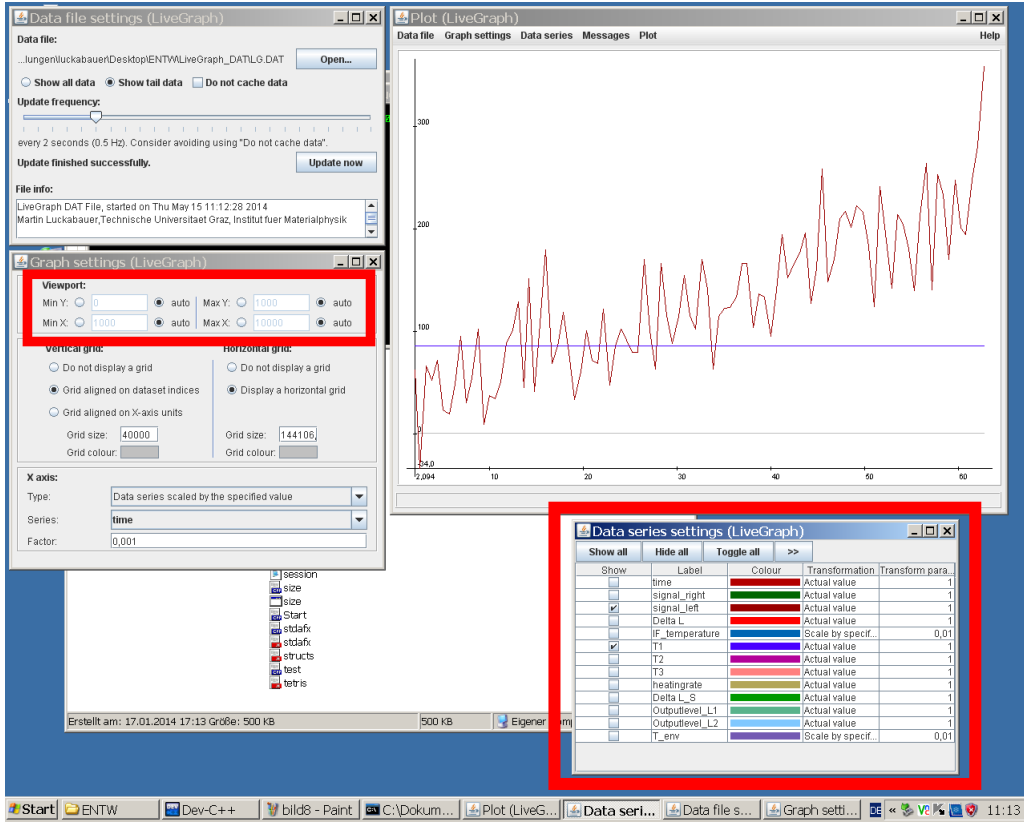
```
106 char alphemode = 0;
107 uint16_t alphainterval = 2;
108 float SP;
109 long int alphatime_int;
110 int high_low = 0;
111 long int alphainterval_count = 0;
112 long int alphatimeinterval = 300;
```

- The variables **alphainterval** and **alphatimeinterval** can be changed according to their data type to an appropriate integer value.
- After changing the parameters the file **Viewer.cpp** must be compiled to make the changes active

The modifiability of the parameters for the CTE mode during runtime of the software should be integrated in a future version to facilitate the usage.

## The LiveGraph Screen

Parallel to the command line software the LiveGraph screen(s) is open to visualize the collected data. The main screen of the program looks like in the following picture:



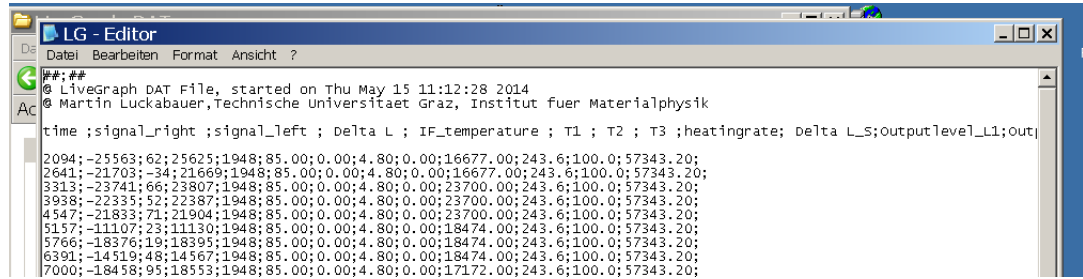
Different mostly self-explaining properties of the graph and the data collection speed can be adjusted in the left side windows. By clicking on the ticks in the area marked by the red square in the picture the corresponding data set is immediately shown in the graph window. When more than one data set is visualized the graph is scaled to the largest value found in any of the marked data sets. In this case it is useful to use the manual y-axis data range adjustment in the mid left side of the picture above, marked with a red square. A complete description of all the functions included in the LiveGraph software can be found in Ref. 44.

## Data storage

All measured values are stored in on textfile called **LG.dat**. The file is located in the **LiveGraph.DAT** folder which can be found in the main folder of the software. Data storage to the file is conducted after the collection of each data set. This assures that it is only possible to loose a few seconds of measurement time when the PC crashes

---

or a hardware error occurs. The structure of the **LG.dat** file looks as shown in the following picture:



The screenshot shows a window titled "LG - Editor". The menu bar includes "Datei", "Bearbeiten", "Format", and "Ansicht". Below the menu is a status bar with "##;##" and "Livegraph DAT File, started on Thu May 15 11:12:28 2014 @ Martin Luckabauer, Technische Universitaet Graz, Institut fuer Materialphysik". The main area contains a text editor with the following content:

```
##;##
@ Livegraph DAT File, started on Thu May 15 11:12:28 2014
@ Martin Luckabauer, Technische Universitaet Graz, Institut fuer Materialphysik
time ;signal_right ;signal_left ; Delta L ; IF_temperature ; T1 ; T2 ; T3 ;heatingrate; Delta L_S;outputlevel_L1;out;
2094;-25563;62;25625;1948;85.00;0.00;4.80;0.00;16677.00;243.6;100.0;57343.20;
2641;-21703;-34;21669;1948;85.00;0.00;4.80;0.00;16677.00;243.6;100.0;57343.20;
3313;-23741;66;23807;1948;85.00;0.00;4.80;0.00;23700.00;243.6;100.0;57343.20;
3938;-22335;52;22387;1948;85.00;0.00;4.80;0.00;23700.00;243.6;100.0;57343.20;
4547;-21833;71;21904;1948;85.00;0.00;4.80;0.00;23700.00;243.6;100.0;57343.20;
5157;-11107;23;11130;1948;85.00;0.00;4.80;0.00;18474.00;243.6;100.0;57343.20;
5766;-18376;19;18395;1948;85.00;0.00;4.80;0.00;18474.00;243.6;100.0;57343.20;
6391;-14519;48;14567;1948;85.00;0.00;4.80;0.00;18474.00;243.6;100.0;57343.20;
7000;-18458;95;18553;1948;85.00;0.00;4.80;0.00;17172.00;243.6;100.0;57343.20;
```

In the first line the data delimiter is defined between the two hash symbols followed by a file description and the actual data. The file can be used in any plot program because of its simple txt format.

**ATTENTION: The LG.dat file must be renamed or stored in another location before starting a new measurement. Otherwise all the data from the last measurement are lost.**

The description above should be enough to use the software and conduct measurements with the laser-interferometer. However at a certain point it will be necessary to change parts of the source code to implement new features. Because the whole source code of the software with all functions is more than 2000 lines long it was decided to make the code available in a separate document which is available at the institute of materials physics.

---

# Acknowledgement

# Danksagung

---

Diese Arbeit entstand in den Jahren 2010 bis 2014 im Rahmen meiner Tätigkeit als wissenschaftlicher Mitarbeiter am Institut für Materialphysik der technischen Universität Graz. Ohne die tatkräftige Unterstützung etlicher Personen wäre die Erstellung dieser Dissertation nicht möglich gewesen. Im Folgenden möchte ich diesen Menschen meinen Dank aussprechen.

An erster Stelle danke ich meinem Betreuer Assoc.Prof. Dr. Wolfgang Sprengel für die unzähligen Stunden an intensiven Diskussionen, sein offenes Ohr für alle erdenklichen Ideen zu neuen Messungen und natürlich für die fachliche Hilfestellung bei der Durchführung dieser Arbeit.

Mein besonderer Dank gilt Herrn Univ.-Prof. Dr. Roland Würschum für die Ermöglichung einer Dissertation am Institut für Materialphysik und für das entgegengebrachte Vertrauen.

Prof. Dr. Gerhard Wilde danke ich für die Begutachtung dieser Arbeit und für die Anreise zum Rigorosum.

Für die wissenschaftliche Zusammenarbeit und die Herstellung der Vitreloy 105 Proben bedanke ich mich bei Herrn Prof. Dr. Jürgen Eckert, Frau Dr. Uta Kühn und Herrn Dipl.-Ing. Benjamin Escher vom Leibniz-Institut für Festkörper- und Werkstoffforschung in Dresden. Ohne die ausgezeichnete Qualität der Proben wären die Ergebnisse diese Arbeit nicht erreichbar gewesen.

## *Acknowledgement / Danksagung*

---

Herrn Prof. Dr. Hans-Jörg Fecht und Herrn Dr. Rainer Wunderlich vom Institut für Mikro- und Nanomaterialien der Universität Ulm danke ich für die Bereitstellung der  $Zr_{56}Al_7Cu_{24}Ni_{10}Co_3$  Proben.

Herrn Prof. Dr. Christoph Hugenschmidt und Herrn Dipl.-Phys. Markus Reiner vom Forschungsreaktor München II danke ich für die Messungen am Positronenstrahl.

Herrn Ao. Univ.-Prof. Dr. Wilfried Schranz und Herrn Mag. Marius Reinecker von der Fakultät für Physik der Universität Wien danke ich für die Möglichkeit DMA-Messungen im Rahmen dieser Arbeit durchführen zu können.

Herrn Univ.-Prof. Dr. Reinhard Pippa und Herrn Dr. Anton Hohenwarter vom Erich Schmid Institut für Materialwissenschaften in Leoben danke ich für die Herstellung des Probenschleifgerätes für das Laser-Dilatomter.

Herrn Dipl.-Ing Alexander Schmon vom Institut für Experimentalphysik gilt mein Dank für die Durchführung der DSC-Messungen.

Mein besonderer Dank für die Mithilfe bei der praktischen Durchführung der Dilatometer-Experimente gilt Herrn Bernhard Nell. Viele seiner guten Ideen sind zu entscheidenden und unverzichtbaren Komponenten des Laser-Dilatometers geworden.

Bei Herrn Dr. Bernd Oberdorfer und bei Herrn Dr. Peter Parz bedanke ich mich für viele interessante Diskussionen in der gemeinsamen Zeit am Institut.

Für das hervorragende Arbeitsklima am Institut und für viele anregende Gespräche bedanke ich mich bei Herrn Dr. Ulrich Brossmann, Herrn Gregor Klinser, Herrn Dipl.-Ing. Stefan Topolovec, Herrn Dipl.-Ing. Jaromir Kotzurek und Frau Dipl.-Ing. Eva-Maria Steyskal.

Frau Regina Steingasser danke ich für ihre Unterstützung in organisatorischen Angelegenheiten. Frau Eva Kniewasser gilt mein Dank für die Unterstützung bei Arbeiten in der Institutswerkstatt.

Bei der Werkstatt des Instituts für Experimentalphysik bedanke ich mich für die Herstellung und Bearbeitung von Teilen für das Laser-Dilatometer.

Für die fortwährende Unterstützung in allen erdenklichen Bereichen meines Lebens bedanke ich mich bei meinen Eltern, Frau Christine Luckabauer und Herrn Dipl.-Ing. Herbert Luckabauer.

---

Meiner Freundin Tanja Pelzmann danke ich für die unermüdliche Unterstützung und den Rückhalt in allen Lebenslagen.

Diese Arbeit wurde vom österreichischen Fonds zur Förderung der wissenschaftlichen Forschung (FWF, Projektnummer: P22645-N20) finanziell unterstützt.

Bei NAWI Graz bedanke ich mich für alle im Rahmen dieser Arbeit zur Verfügung gestellten Ressourcen.